

## WI<sup>n</sup>d and Salinity Experiment 2000 (WISE 2000) Scientific Analysis Report

(ESTEC Contract No 14188/00/NL/DC)

Technical Assistance for the Implementation of the WISE 2000 Campaign).

Version 1.00, August 31, 2001

### Participants:

Universitat Politècnica de Catalunya (Spain)

Institut de Ciències del Mar, CSIC (Spain)

Laboratoire d'Oceanographie DYnamique et de Climatologie, UPMC (France)

Universitat de València (Spain)

Centre d'Études des Environnements Terrestre et Planétaires (France)

University of Massachusetts, Amherst (USA)



## WISE Scientific Analysis Report

**WISE 2000 Participants:**

UNIVERSITAT POLITÈCNICA DE CATALUNYA (UPC)  
A. Camps, I. Corbella, M. Vall-llossera, L. Enrique, R. Villarino, J. Miranda, F. Julbé

INSTITUT DE CIÈNCIES DEL MAR (ICM-CSIC)  
J. Font, C. Gabarró, A. Julià, M. Emelianov

LABORATOIRE D'OCÉANOGRAPHIE DYNAMIQUE ET DE CLIMATOLOGIE  
(LODYC)  
J. Etcheto, J. Boutin

UNIVERSITAT DE VALÈNCIA (UV)  
V. Caselles, E. Rubio, R. Niclòs, L. Martínez

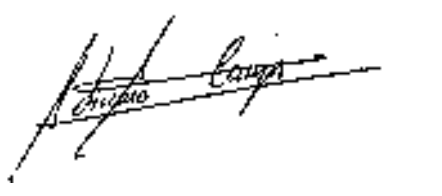
CENTRE D'ÉTUDES DES ENVIRONEMENTS TÉRRESTRE ET PLANÉTAIRES  
(CETP)  
A. Weill, G.L. Kalpaktchioglou (?)

UNIVERSITY OF MASSACHUSETTS, AMHERST (MIRSL-UMass)  
S. Reising, E. Knapp, K. Horgan, J. Pons, A. Bajaj

Written by (in alphabetical order):

Boutin, J. (LODYC)  
Camps, A. (UPC)  
Corbella, I. (UPC)  
Etcheto, J. (LODYC)  
Font, J. (ICM)  
Gabarró, C. (ICM)  
Reising, S.C. (UMass)  
Rubio, E. (UV)  
Vall-llossera, M (UPC)  
Weill, A. (CETP)

Approved by: Camps, A. (UPC)



---

Adriano Camps,  
Associate Professor, Polytechnic University of Catalonia, Spain (UPC)  
Barcelona, August 29, 2001

**The WInd and Salinity Experiment 2000: Scientific Analysis Report.**

1.Introduction	10
2.Analysis of in-situ data:	
2.1. Analysis of sea surface temperature and salinity (ICM)	13
2.2. Analysis of wind speed data (LODYC)	16
2.3. Analysis of infra-red radiometer data (UV)	19
2.3.1.Introduction	19
2.3.2.Description of the CIMEL CE-312 radiometer	20
2.3.3.Field measurement strategy	21
2.3.4.Laboratory calibration of the CE-312 radiometer	23
2.3.5.Sea surface temperature retrieval	25
2.3.6.SST processing and assessment	31
2.3.7.Intercomparison between CE-312-calculated, buoy-measured and AVHRR- observations of the SST	33
2.4. Analysis of sea state	36
2.4.1. Analysis of significant wave height (ICM)	36
2.4.2. Analysis of stereo-camera data (CEPT)	37
2.4.3. Analysis of video imagery from antenna boresight (UPC)	43
3.Analysis of satellite imagery data (LODYC)	47
3.1.Analysis of sea color	47
3.2.Analysis of AVHRR imagery	48
3.3.Analysis of Quicksat data	49
4.Analysis of radiometric data	50
4.1.L-band radiometric data (UPC)	50
4.1.1. L-band brightness temperatures: Signatures in elevation and azimuth	51
4.1.2. L-band brightness temperatures: Sensitivity to wind speed	53
4.2.Ka-band radiometric data (UMass)	56
4.2.1. Ka-band brightness temperatures: Time series	57
4.2.2. Ka-band brightness temperatures: Signatures in elevation	57
5.Emissivity modeling studies: comparison with WISE and reported measurements	59
5.1.Introduction (UPC)	59
5.2.Kirchhoff model (UPC)	61
5.3.Small Perturbation Method (UPC)	67
5.4.IEM model (UPC)	68
5.5.Yueh-LODYC two-scale model (LODYC)	70
5.6.Models and data inter-comparison (LODYC-UPC)	71
5.7.Rain effects on the brightness temperature at L-band:	72
modelling results (UPC)	
5.7.1.Description of the model	72
5.7.2.Simulation results at L-band	73



## WISE Scientific Analysis Report

6.Simulation results at L-band in WISE conditions (LODYC)	74
7.The sea surface salinity retrieval problem	78
7.1.Sea surface retrieval using WISE data (ICM)	78
7.1.1. Emissivity models	79
7.1.2. Error in the in-situ measurements	82
7.1.3. Conclusions	83
7.2.Sea surface retrieval using WISE fits in the SMOS configuration (UPC)	84
7.2.1. Introduction	84
7.2.2. SSS retrieval algorithm	86
7.2.3. Conclusions	86
8.General conclusions of WISE 2000	92
Bibliography	93

**List of figures:**

- Figure 1.1. Sensor locations during WISE-2000.
- Figure 2.1. SST recorded from two moored buoys (violet: buoy 1, pink: buoy 4)
- Figure 2.2. SSS recorded from two moored buoys (purple: buoy 1, orange: buoy 4) from mid November 2000 to mid January 2001
- Figure 2.3. Salinity difference between sensors located at -5 m and -0.2 m
- Figure 2.4. Stability test: wind speed ( $U_{10}$ ) ratio versus air-sea temperature difference
- Figure 2.5. Wind speed mapped at 10 m ( $U_{10}$ ) from different sources: meteo station (red), buoy 2 (green) and QUIKSCAT satellite (blue)
- Figure 2.6. Wind speed ( $U_{10}$ ) comparison; fit 3-15 m/s (green), fit whole range (red)
- Figure 2.7. Normalized spectral response functions for the channels of CIMEL CE-312 radiometer.
- Figure 2.8. Detail of the housing camera containing the CE 312 optical head and deployed on the Scientific Atlanta pedestal.
- Figure 2.9. Diagram of the different contributions to the measured radiance  $R_m$  during the laboratory calibration exercises.
- Figure 2.10. Scatter plot of the radiance differences measured for the calibration experience of the CE 312 channel 1.
- Figure 2.11. Elevation dependence of seawater emissivity in the CE 312 channel 1 for wind speeds in the 0-15 m/s interval.
- Figure 2.12. Sky brightness temperature obtained from CE 312 radiometer on 15<sup>th</sup> December of the 2000. Sky scans at specific times are highlighted.
- Figure 2.13. Sky brightness temperature obtained from CE 312 radiometer on 17<sup>th</sup> December of the 2000. Sky scans at specific times are highlighted.
- Figure 2.14. Biases in the SST retrieval resulting from no correcting from the atmospheric emission and attenuation along the path length sea-sensor versus the total water vapor content of the atmosphere. dSST stand by the difference approximated SST and actual SST. These values are average differences for SST ranging between 10 and 18 °C and surface wind ranging between 0 and 15 m/s.
- Figure 2.15. First preliminary SST values retrieved from an elevation scan which was performed on 2<sup>nd</sup> December 2000. The slightly dependence on the elevation angle is in a critical part due to using no appropriate emissivity values for angles greater than 30°.
- Figure 2.16. Comparison between the SST observations registered by the oceanographic buoys of ICM and LODYC and the retrieved from the CE 312 radiometric measurements performed in the 8-12 μm region and at 25 –35° elevation angle.
- Figure 2.17. Low passed (6h filter) wave height (blue) and wind speed (pink) for the period December 13 to January 14
- Figure 2.18. Samples of stereo-images used in the analysis
- Figure 2.19. Picture acquired on 12/15/2000. Foam, wind and complex topography
- Figure 2.20. Picture acquired on 12/08/2000. Calm sea, no foam, complex topography
- Figure 2.21. Relationship between foam percent and wind speed as derived from the stereo-camera (pointing to the North)
- Figure 2.22. Typical example of 1D omnidirectional sea surface spectrum as derived from CEPT stereo-cameras during WISE 2000 campaign.
- Figure 2.23. Typical example of 2D directional sea surface spectrum as derived from CEPT stereo-cameras during WISE 2000 campaign.
- Figure 2.24. Typical sea surface topography and height variances along the directions parallel (X) and perpendicular (Y) to the platform derived from CEPT stereo-cameras during WISE 2000 campaign.

- Figure 2.25. Photogram from antenna boresight ( $\theta=25^\circ$ ) truncated to the antenna half power beamwidth.
- Figure 2.26. Example of instantaneous variation of sea foam coverage within antenna footprint.
- Figure 2.27. Sample images of maximum and minimum sea foam coverage during a scan (two different incidence angles: a-b  $\theta = 25^\circ$ , c-d  $\theta = 65^\circ$ )
- Figure 2.28. Foam coverage (%) and 1-sigma standard deviation bars derived from UPC video camera mounted on antenna pedestal (linear scale).
- Figure 2.29. Foam coverage (%) derived from UPC video camera mounted on antenna pedestal. In logarithmic scale the scatter plot is fit by a line with slope 3.4988, in agreement with Monahan and Lu and Weill.
- Figure 2.30. Foam coverage decay in a series of consecutive photograms.
- Figure 3.1. Seawifs chlorophyll image of the platform region on December 26.
- Figure 3.2. Sea surface temperature image of the platform region on December 11
- Figure 3.3. Sea surface temperature image of the platform region on December 26
- Figure 3.4. QUIKSCAT versus meteo station wind speed ( $U_{10}$ ) comparison.
- Figure 4.1. a) Top and b) side views of the LAURA radiometer.
- Figure 4.2. Sample measurements of elevation scans at horizontal (left) and vertical polarizations (right) for two different wind speeds: 1.3 m/s (a-b) and 11.9 m/s (c-d).
- Figure 4.3. Sample measurements of azimuth scans at horizontal (left) and vertical (right) polarizations for three different wind speeds and incidence angles: (a-b)  $\theta=25^\circ$ , WS = 2.7 m/s, (c-d)  $\theta=45^\circ$ , WS = 2.8 m/s, and (e-f)  $\theta = 35^\circ$ , WS = 10.9 m/s.
- Figure 4.4. Sample measurements of azimuth scans for the third Stokes parameter (U): (a)  $\theta=45^\circ$ , WS = 2.8 m/s, and (b)  $\theta=35^\circ$ , WS = 9 m/s.
- Figure 4.5. Sensitivity to wind speed of the L-band brightness temperature at horizontal (left) and vertical (right) polarizations at different incidence angles: (a-f)  $\theta=25^\circ$ , (b-g)  $\theta=35^\circ$ , (c-h)  $\theta=45^\circ$ , (d-i)  $\theta=55^\circ$  and (e-j) $\theta=65^\circ$ .  
Legend: SST: Blue: < 14.5 °C, Green: from 14.5 °C to 15.5 °C, Red: >15.5 °C  
Wind direction relative to radiometer:  $\blacktriangle$ : up-wind,  $\blacktriangledown$  : down-wind, x : cross-wind
- Figure 4.6. Sensitivity of  $T_h$  (blue) and  $T_v$  (red) to wind speed at 10 m height
- Figure 4.7. Series of instantaneous brightness temperatures at  $\theta=65^\circ$  for (a-b-c) vertical and (d-e-f) horizontal polarizations.
- Figure 4.8. Azimuthally averaged brightness temperatures vs. incidence angle for different wind speeds: a) WS = 2 m/s, b) WS = 5 m/s, c) WS = 8 m/s, and d) WS = 10 m/s.
- Figure 4.9. Azimuthally-averaged horizontal brightness temperatures vs. incidence angle for different wind speeds: a) WS = 2 m/s, b) WS = 5 m/s, c) WS = 8 m/s, and d) WS = 10 m/s.
- Figure 5.1. Incidence angle dependence of the difference between brightness temperatures computed using Ellison or Klein&Swift sea water permittivity model (SST = 18°C, SSS = 36°C, f = 1.41 GHz).
- Figure 5.2. SST dependence of the difference between brightness temperatures computed using Ellison or Klein&Swift sea water permittivity model ( $\theta=0^\circ$ , f = 1.41 GHz).
- Figure 5.3. Brightness temperature uncertainties associated to the measurement uncertainty in the dielectric permittivity of the sea water: Ellison (red) and Klein-Swift (blue) models.
- Figure 5.4. The yellow zone in the plot marks the validity range of the Kirchhoff model.
- Figure 5.5. Wind Speed range in which Kirchhoff hypothesis are valid at 1.4 GHz (blue zone).
- Figure 5.6. a) Validity margin (yellow zone) of Stationary-Phase approach. b) Validity range of the wind speed at 12.5 m from the sea surface at 1.4 GHz.
- Figure 5.7. a) Validity margin (yellow zone) of scalar approach. b) Validity range of the wind speed at 12.5 m from the sea surface at 1.4 GHz.
- Figure 5.8. Validity margin of the wind speed at 12.5 m from the sea surface respect to the frequency for a) Stationary-Phase approach and b) Scalar approach.

- Figure 5.9. Simulation results using the Kirchhoff model under the SPA showing the amplitude of the (a-b) zeroth, (c-d) first and (e-f) second harmonics of the horizontal (left) and vertical (right) brightness temperatures ( $T_{h,v}(\phi)=T_{h,v0}+T_{h,v1}\cos(\phi)+T_{h,v2}\cos(2\phi)$ )
- Figure 5.10. The yellow zone represents the combination of correlation length and rms height values in which SPM model obtain accurate results.
- Figure 5.11. a) The most restrictive condition for the height standard deviation when SPM is applied. The maximum wind speed at 12.5 m from the sea surface is 1.34 m/s at 1.4 GHz. b) Maximum wind velocity allowed respect to the frequency for obtaining accurate results with SPM.
- Figure 5.12. The yellow zone establishes the validity range of the IEM method for a sea surface with 38‰ of salinity at 15°C and Gaussian autocorrelation function.
- Figure 5.13. a) Validity range for IEM small scale. b) Validity range for IEM large scale.
- Figure 5.14. Slopes of Tb versus U derived from Yueh-LODYC model with 3 different spectra.
- Figure 5.15. WISE 2000-derived brightness temperature sensitivities to wind speed vs. incidence angle at vertical (red circles) and horizontal polarizations (blue circles) and comparison with Hollinger's measurements (diamonds) and Yueh-LODYC 2-scale model (Durden-Veseckix spectrum x 2, solid line).
- Figure 5.16. Wind-induced spectrum for wind speeds 2, 5, 10, 15 and 20 m/s and rain-induced spectrum for rain rates 20, 40, 60 and 80mm/h.
- Figure 5.17. Sea surface slope variances versus wind speed in rain free conditions and for rain rates of 20, 40, 60 and 80 mm/h.
- Figure 5.18. Vertical polarization of the brightness temperature change at 1.4 GHz due to the presence of rain:  $\Delta T_{Bv}=T_{bv}(\theta, WS, rr) - T_{bv}(\theta, WS, 0)$ . a) Wind Speed = 0m/s. b) Wind Speed = 10 m/s. c) Wind Speed = 20 m/s.
- Figure 5.19. Horizontal polarization of the brightness temperature change at 1.4 GHz due to the presence of rain:  $\Delta T_{Bh}=T_{bh}(\theta, WS, rr) - T_{bh}(\theta, WS, 0)$ . a) Wind Speed = 0m/s. b) Wind Speed = 10 m/s. c) Wind Speed = 20 m/s.
- Figure 6.1. Tb (h-pol) variations at 30° incidence angle predicted by the Klein and Swift sea water parametrization (red) and by the Ellison parametrization (green), when only SSS and SST variations are taken into account.
- Figure 6.2. Tb (h-pol) variations at 30° incidence angle predicted by the Klein and Swift sea water parametrization due to SST variations at fixed SSS (37.8 psu) (purple) and due to SSS variations at fixed SST (15.2°C) (orange).
- Figure 6.3. Influence of the wind speed on Tb at 30° incidence angle (in V-pol) when using two sources of wind speed (top) (meteorological station (purple) ; ICM float (blue)), and when using two wave spectra (bottom) (Elfouhaily (green) ; Durden and Veseckix2 (purple)). On average, the difference coming from the different wind speed source is 0.2 K whereas the difference coming from the use of different spectra is 0.35K.
- Figure 6.4. Influence of the wind speed on Tb at 30° incidence angle (in H-pol) when using two sources of wind speed (top) (meteorological station (purple) ; ICM float (blue)), and when using two wave spectra (bottom) (Elfouhaily (green) ; Durden and Veseckix2 (purple)). On average, the difference coming from the different wind speed source is 0.2 K whereas the difference coming from the use of different spectra is 0.7K.
- Figure 7.1. Block diagram of the salinity retrieval algorithm
- Figure 7.2: Comparison of retrievals using different models.
- Figure 7.3. Comparison of retrieved SSS using in-situ and satellite wind data.
- Figure 7.4. The SMOS imaging characteristics: a pixel is imaged many times under different incidence angles, with different spatial resolutions and radiometric sensitivities. Parameters: NEL=21 antennas per arm,  $d = 0.875$  wavelength antenna spacing,  $\beta=32^\circ$  tilt angle,  $h = 755$  km platform height.

- Figure 7.5. Brightness temperature at nadir dependence with SSS and SST:  
Figure 7.6. Sensitivity of brightness temperature to WS vs. incidence angle.  
Figure 7.7. Standard deviation of the retrieved SSS for different wind speed 0 m/s (left) and 10 m/s (right), different SSS (a-b) 30 psu, (c-d) 35 psu and (e-f) 40 psu, and different SST: 5°C, 15°C and 25°C.  
Figure 7.8. Standard deviation of the retrieved SST for different wind speed 0 m/s (left) and 10 m/s (right), different SSS (a-b) 30 psu, (c-d) 35 psu and (e-f) 40 psu, and different SST: 5°C, 15°C and 25°C.  
Figure 7.9. Standard deviation of the retrieved WS for different wind speed 0 m/s (left) and 10 m/s (right), different SSS (a-b) 30 psu, (c-d) 35 psu and (e-f) 40 psu, and different SST: 5°C, 15°C and 25°C.  
Figure 7.10. Histograms of retrieved SSS, SST and WS (16 simulations) for SSS = 30 psu, SST = 15°C and WS = 0 m/s.  
Figure 7.11. Histograms of retrieved SSS, SST and WS (16 simulations) for SSS = 35 psu, SST = 15°C and WS = 10 m/s.

**List of tables:**

- Table 1.1. Data acquisition periods  
Table 2.1. Coefficients of the calibration of CE 312 thermal channels, equation (2.2).  
Table 4.1. Number of data points for each plot in figure 4.5.

## 1. Introduction

In May 1999 the European Space Agency (ESA) selected **SMOS** as the second **Earth Explorer Opportunity Mission**. Its goals are obtention of **Soil Moisture** and **Ocean Salinity** maps with global coverage. SMOS will be the first two-dimensional synthetic aperture radiometer ever built for Earth observation. The scanning configuration of SMOS presents new challenges:

- i) Two-dimensional imaging of the scene, with varying incidence angles and pixel resolution as the pixel travels through the alias-free field of view.
- ii) Polarization mixing between vertical and horizontal polarizations due to the relative orientation between the antenna reference frame and the pixel's local reference frame.
- iii) Not yet well understood azimuthal dependence of the first two Stokes parameters ( $T_v$  and  $T_h$ ) with wind direction.
- iv) Unknown signature of the third and fourth (U and V) Stokes parameters and their azimuth/elevation dependence with wind speed.
- v) Effect of sea foam at L-band.
- vi) Feasibility of accurate retrieval of U, and eventually V, assuming that Faraday rotation effects (for a satellite borne sensor) have been corrected for by other means.

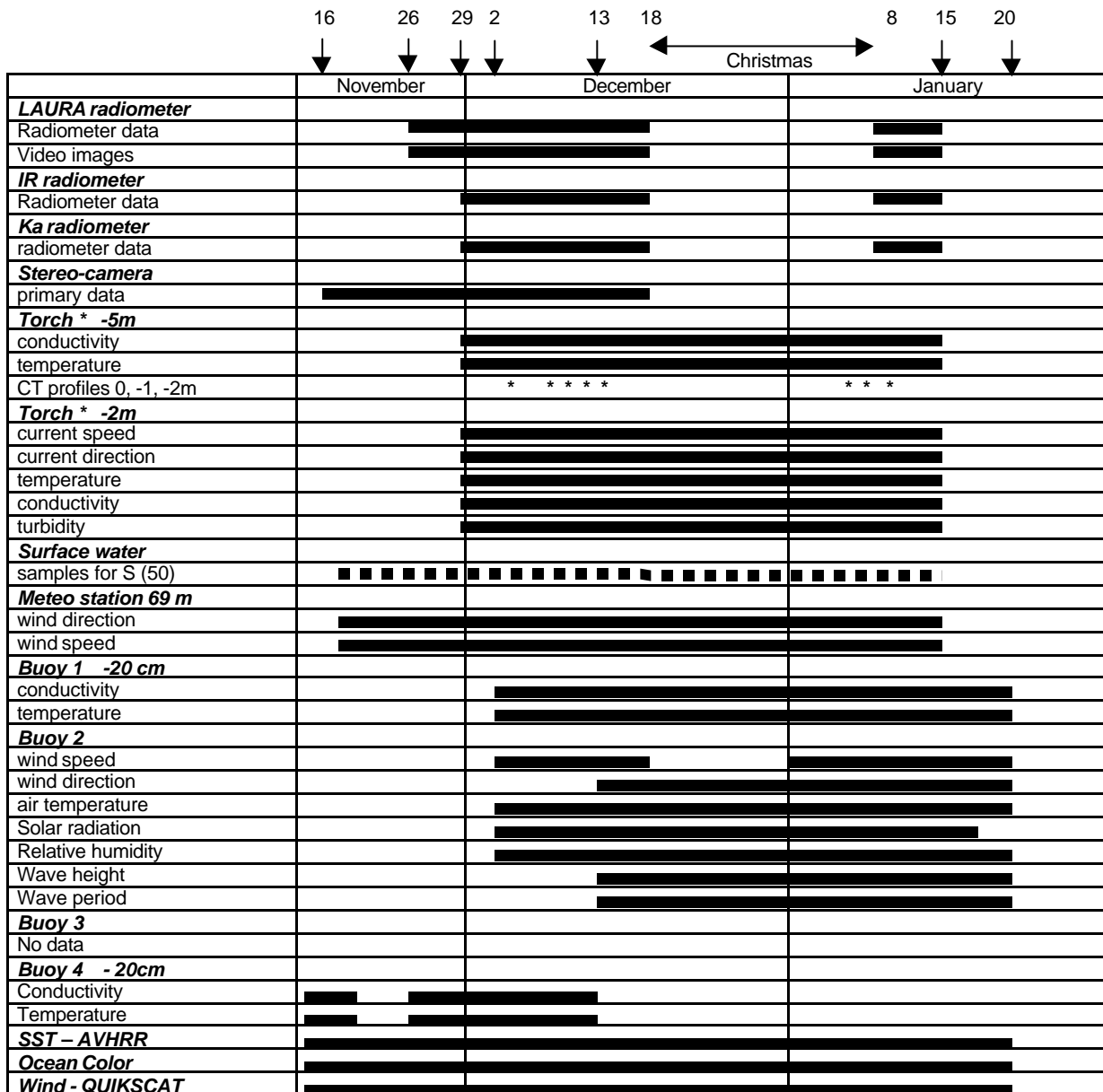
The **WISE 2000 campaign** was sponsored by ESA to collect experimental data under the widest possible range of wind conditions to better understand the polarimetric emission at L-band of the sea surface and its dependence with wind and salinity (points (i), (iii), (iv) and (v)). Point (ii) is a known geometrical problem. Point (iii) is specifically addressed by the LOSAC campaign. Finally, point (vi) will depend on MIRAS antenna parameters and the amplitude of the azimuthal signature of the third (and fourth, if detectable) parameters.

Fully polarimetric L- and Ka-band radiometers, a video, an IR and a stereo-camera, and four oceanographic and meteorological buoys were installed in the Casablanca oil rig, located at  $40^{\circ} 43' 4''$  N  $1^{\circ} 21' 34''$  E, 40 km away from the Ebro river mouth at 40 Km from the coast of Tarragona (Spain) as shown in Figure 1.1. The sea conditions are representative of the open Mediterranean with periodic influence of the Ebro river fresh water plume. Systematic measurements were acquired from November 16<sup>th</sup> to December 18<sup>th</sup>, 2000 and continued during the January 9<sup>th</sup> to 15<sup>th</sup>, 2001 (table 1.1). This document presents the scientific analysis performed by the team members within the frame of the WISE-2000 activities.



## WISE Scientific Analysis Report

**Table 1.1.** Data acquisition periods



## WISE Scientific Analysis Report

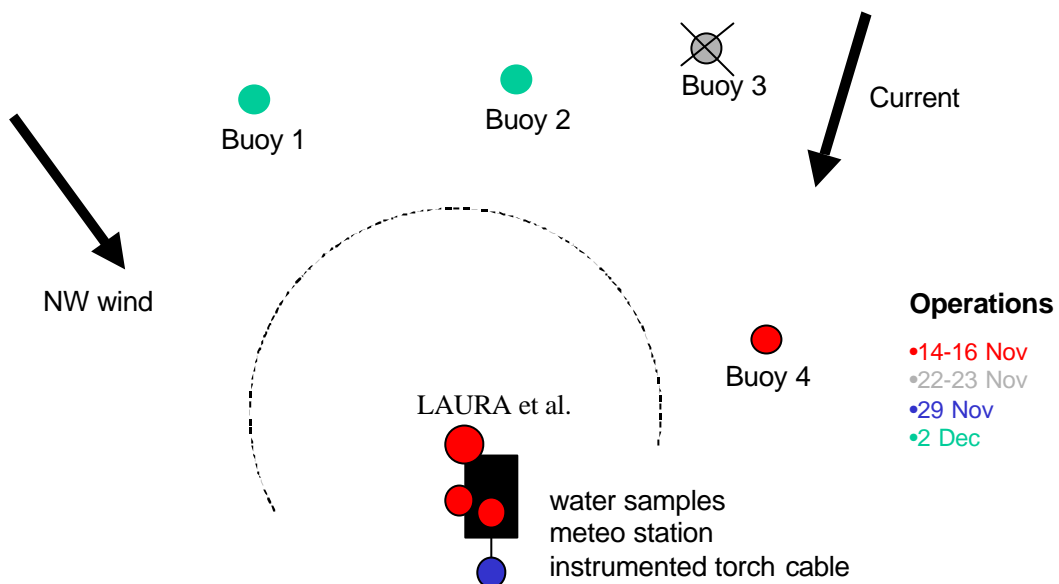
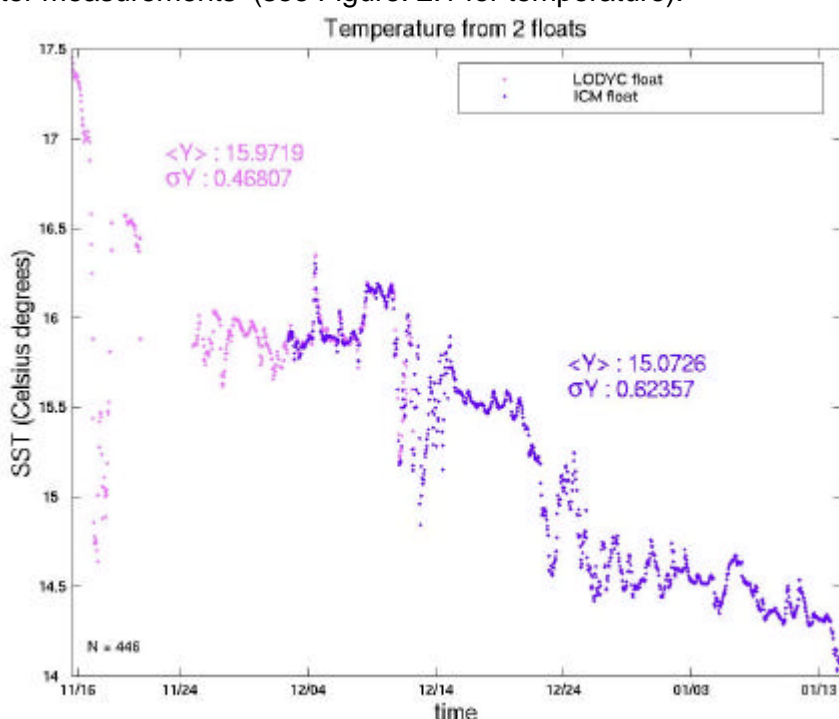


**Figure 1.1.** Sensor locations during WISE-2000.

## 2. Analysis of in-situ data

### 2.1 Analysis of sea surface temperature and salinity (ICM)

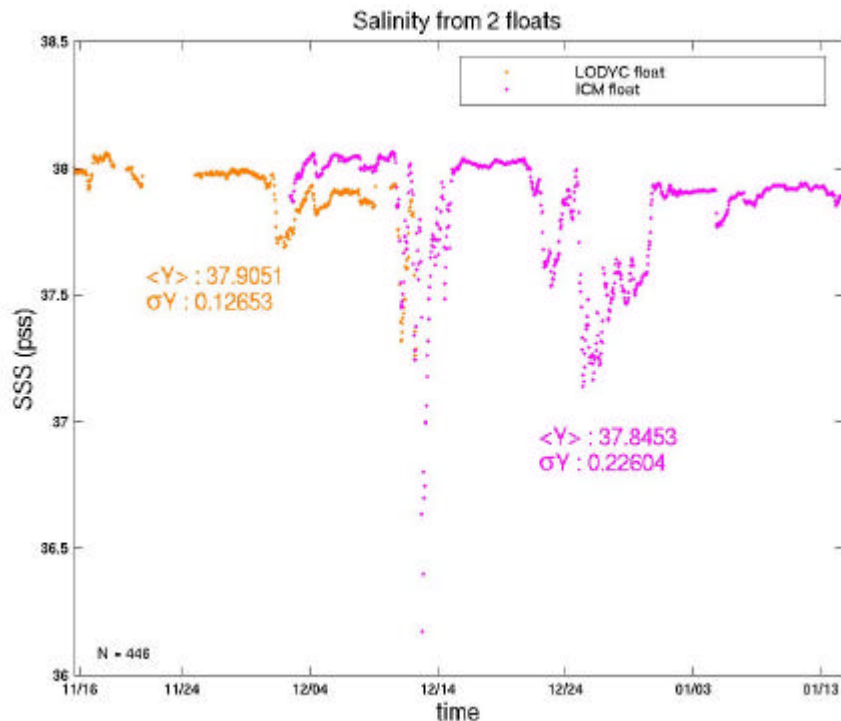
Sea surface temperature and salinity in the area of the Casablanca platform were monitored by means of in situ sensors deployed in moored buoys (see WISE 2000 Data Acquisition Report). Since neither buoy 1, nor buoy 4 worked for the whole duration of the campaign, we compared their measurements for the common period: on average, SST from buoy 4 was 0.015°C warmer than the one from buoy 1, while its SSS was 0.13 psu lower. The resolution, accuracy, and hence consistency, between all sensors were good enough to provide the required in situ data set and reconstruct time series to complement the radiometer measurements (see Figure. 2.1 for temperature).



**Figure 2.1.** SST recorded from two moored buoys (violet: buoy 1, pink: buoy 4) from mid November 2000 to mid January 2001

The surface temperature temporal evolution is typical of the autumn season. November is usually the month when the erosion of the summer stratification is speed up by the occurrence of strong and cold winds: SST values that can be above 25°C at the end of the warm season (September) will drop to around 13°C after completion of the winter vertical mixing (February). During the first two weeks of WISE 2000 the temperature decreased by more than 1.5°C, then the surface cooling continued regularly for the rest of the measurement period, with another strong drop around December 20, and even some short periods of small increase as around December 10. In total SST ranged from 17.5°C to 14°C. The sudden decrease detected by the sensor in buoy 4 near to the beginning of

the series (see Figure 2.1) was short in time, but very strong (almost 2.5°C). We don't have a clear explanation for this, as it was not related to a remarkable signal on the salinity records, but contemporaneous to quite strong and perhaps cold (we don't have air temperature data at that moment) northerly winds.



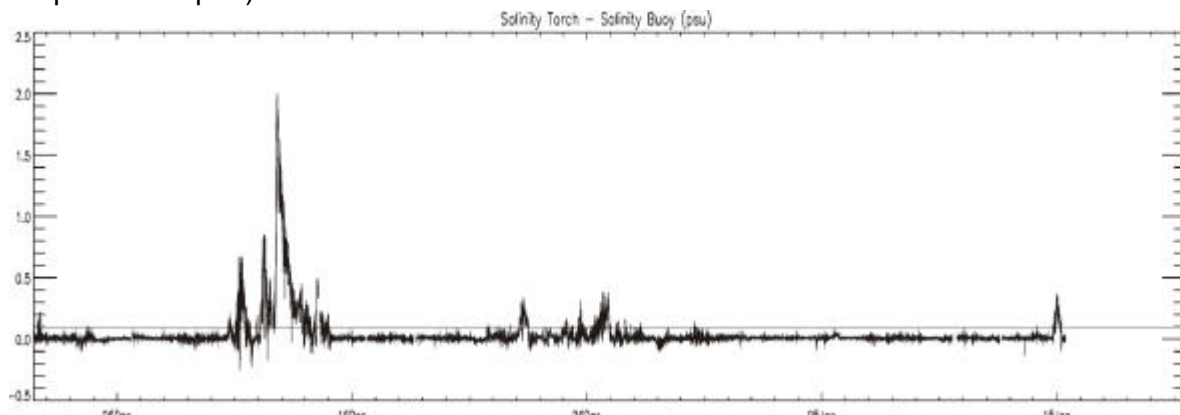
**Figure 2.2.** SSS recorded from two moored buoys (purple: buoy 1, orange: buoy 4) from mid November 2000 to mid January 2001

Figure 2.2 shows the surface salinity recorded from buoys 1 and 4. There is an evident offset (1.5 psu) between both series that has been explained by the lower accuracy of the sensor in buoy 4 since, as detailed in the Data Acquisition Report, the accuracy in the measurements from buoy 1 was within specifications. SSS, during the whole experiment period, remained near 38 psu, a value typical of the Mediterranean open sea waters that, unlike temperature, do not display a clear seasonal salinity signal. This means that the WISE area was usually out of the direct influence of the Ebro river discharge. The salinity time series shows the occurrence of some low SSS events that typically had duration of 5-6 days. These events, especially the one around December 12 (strongest SSS drop), are associated to similar SST decreases, a possible indication of the river plume reaching the Casablanca area, as continental waters are not only fresher, but also colder than ambient water. This interpretation has been confirmed by the sequence of satellite infrared images that display the evolution of the cold-water tongue from the river mouth to this offshore location. The standard situation presents an alongslope current from the NE that keeps the river plume close to shore and continental waters flowing to the SW, away from the platform. But occasionally, current reversals, strong southerly winds or a significant increase of the river discharge, allow these lower salinity waters to reach our

experiment area. The two main events detected during WISE resulted in recorded SSS values 2 psu (December 12) and almost 1 psu (December 25) lower than the regular 37.9-38 psu observed all around the experiment.

An important issue related to salinity remote sensing is the possible presence of a vertical salinity gradient. A microwave radiometer will only measure the very surface values, which is not the case of in situ sampling, where sensors have to be completely immersed in seawater. Validation of SMOS salinity determinations will strongly rely on in situ measurements made from standard moored or drifting buoys, or even hydrographic casts or underway measurements from research or opportunity vessels. In all these cases temperature, and especially conductivity, sensors are not operated close to the surface to avoid interference from air bubbles and even to protect them from possible sources of dirt. A present standard value for near surface salinity measurement is 5 m below sea level. In some cases, especially after strong rainfall, salinity at this depth can be significantly different from SSS and then errors can be introduced by comparing both values.

The difference between salinity close to the surface (-20 cm, buoy 1) and at 5 m was monitored during WISE 2000 by deploying a second instrument at this depth (see Data Acquisition Report).



**Figure 2.3.** Salinity difference between sensors located at -5 m and -0.2 m

Most of the time the difference between both time series is below 0.1 psu, a value that can be considered a threshold for SSS satellite remote sensing resolution. And it is only remarkable during the reported low salinity events, especially that of December 10-15 when the difference reached up to 2.0 psu. The latter is another confirmation that this event was due to an intrusion of the river plume, a near-surface phenomenon, since at 20 cm the salinity drop from ambient water was almost 2.1 psu while at 5 m it was only 0.8 psu maximum.

To increase the knowledge on the vertical resolution of the salinity gradient the sensor at -5 m was manually raised to -2 m, -1 m and to the surface in several occasions. The

resulting profiles, with typically a duration of about one hour and a half, display very small salinity variations (see plot F in Data Acquisition Report, ICM Contribution) except those on December 12 and 14 (low salinity event) and January 10 at surface (probably effect of air bubbles). In these specific cases it is remarkable the high temporal variability of the salinity values, which reflects the dynamic character of the event. This was also observed in the SSS time series, where changes of the order of 2 psu can be recorded in very few hours. This poses an additional problem to the satellite SSS validation that has to be analysed in the framework of the general cal/val strategy and considering the decorrelation scales at open oceans.

For the WISE 2001 experiment it has been decided to monitor again temperature and salinity at -0.2 and -5 m, but discard the vertical profiles. The additional information they can provide is not significant enough to compensate for the extra operational and data processing load they imply.

## **2.2. Analysis of wind speed data**

Three instruments measured the wind speed:

- Meteorological station at 69 m height on the platform provided 15 min averages
- Buoy 2 provided a measurement at 2.5 m height every 2 min
- Satellite borne scatterometer (QUIKSCAT) : see § 3.3.

The first step is to map the in-situ measurements to 10 m height (meteorological standard). The method used is described below:

### **HYPOTHESIS:**

- Inside the boundary layer (buoy 2):
- Assume neutral stability
- Use the Smith [1988] drag coefficient
  
- For the meteo station at 69m height:
- Assume the boundary layer thickness to be 10 times  $U_{10}$
- Assume uniform wind speed in the mixed layer

### **METHOD:**

- Compute  $U_{10}$  from 69m to 10m using the above method
- Check if  $10 \times U_{10} > 69$ :
  - if yes O.K.
  - if no, compute new  $U_{10}$  from  $10 \times U_{10}$  to 10m using the same method
- -iterate until it converges

In order to check the hypothesis of neutral stability we plotted the ratio of the wind speed measured by the two instruments versus the air temperature minus the water

temperature: no tendency is visible on the Figure 2.4 shown below even though on average the water is one degree warmer than the air indicating an atmosphere generally slightly unstable. Since the air temperature is not available for the whole campaign we did not make the correction for stability.

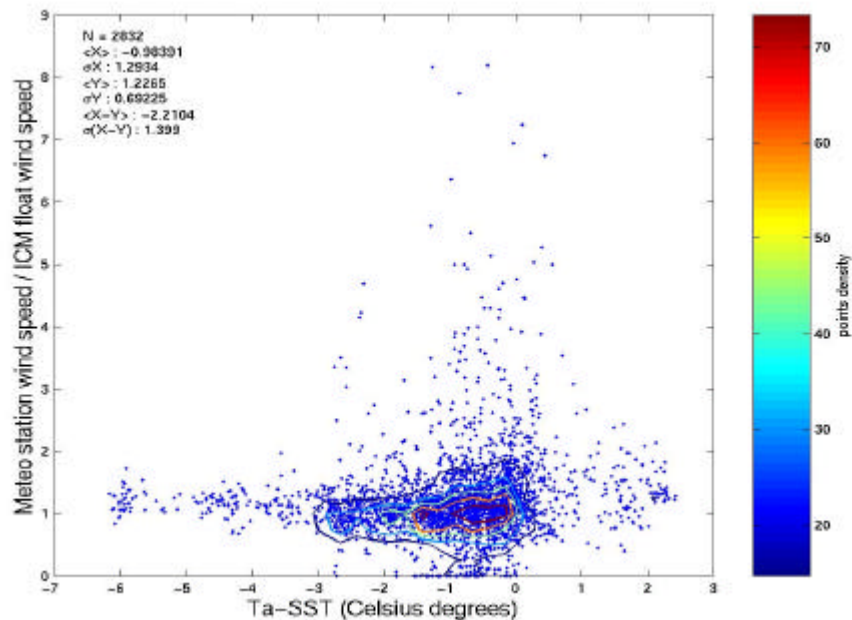


**Figure 2.4.** Stability test: wind speed ( $U_{10}$ ) ratio versus air-sea temperature difference

The only instrument which measured for the whole period is the platform meteorological station. The measurements of the three instruments mapped to 10 m height are plotted against time in the Figure 2.5 below.

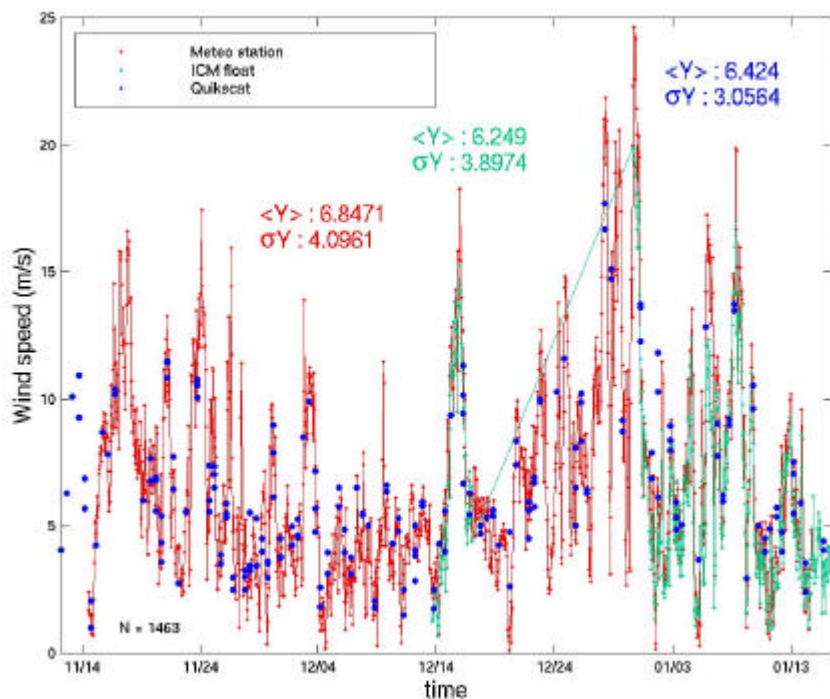


**Figure 2.5.** Wind speed mapped at 10 m ( $U_{10}$ ) from different sources: meteo station (red), buoy 2 (green) and QUIKSCAT satellite (blue)

The wind speed averaged during the whole period is 6.8 m/s. Wind speed higher than 15 m/s were observed on November 17, 24 and 26, on December 15, 28, 29, 30 and 31 and on January 5, 6 and 8. Unfortunately the strongest winds were observed during the Christmas/New Year period during which the manned experiments were not operating.

We compared the measurements made by the various instruments, mapped to 10 m height, during the period of common measurements. For the comparison to be meaningful we averaged the measurements during one hour.

The Figure 2.6 below shows the measurements of the meteorological station on the platform (y axis) against the measurements made simultaneously by buoy 2. The regression lines are orthogonal regressions (same weight given to the two types of measurements, minimize the distance perpendicular to the fit). We fitted the measurements in the range 3 - 15 m/s (most commonly observed wind speed range and optimal range for instruments) and in the whole data range.

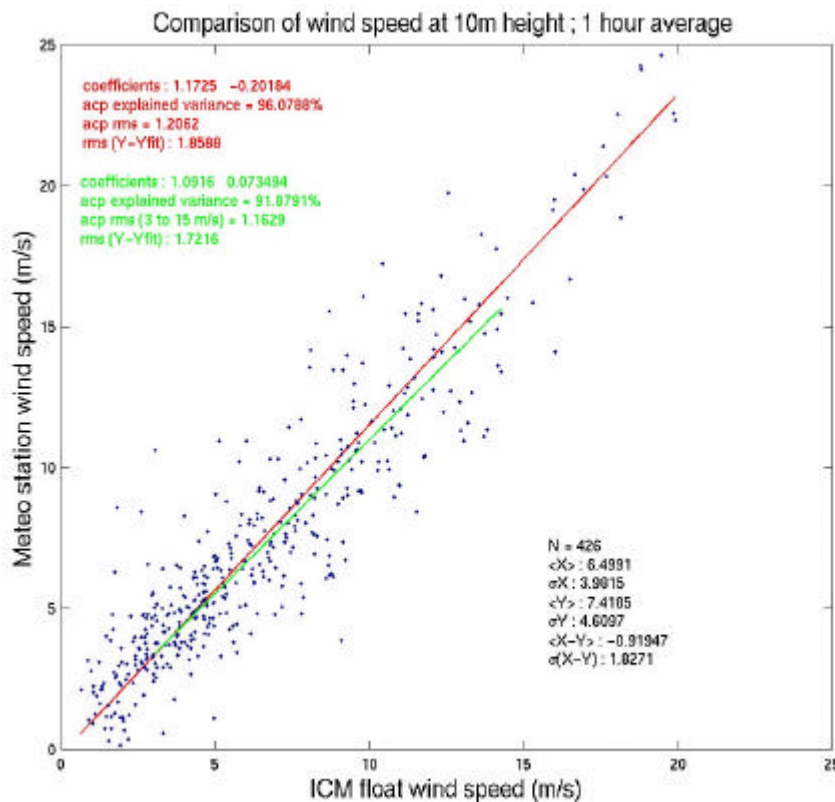


**Figure 2.6.** Wind speed ( $U_{10}$ ) comparison; fit 3-15 m/s (green), fit whole range (red)

In the range 3-15 m/s the equation of the fit is:  $U_M = 1.09 U_B + 0.07$  with an explained variance of 92%, in the whole range it is  $U_M = 1.17 U_B - 0.20$  with an explained variance of 96%. The mean difference between the instruments is  $\langle U_B - U_M \rangle = -0.92$  m/s with a standard deviation of 1.83 m/s. In the most commonly observed range the instruments differ by about 10%, the standard deviation of the difference being rather high. We checked that the measurements are nevertheless usable for checking emissivity models (see §6). This discrepancy might be due to several factors:

- different instruments
- different height: the mapping to 10 m is not perfect and from 69 m it is a large correction (we tried to correct for the stability, but it did not improve the result), the platform is likely to disturb the air flow less at the top than at low altitude.

### 2.3. Analysis of infra-red radiometer data

#### 2.3.1. Introduction

The main objective of the Remote Sensing Unit of the University of Valencia within the ESA-sponsored measurement campaign WISE 2000: WIInd and Salinity Experiment, has been to provide sea surface skin temperature (SST) estimations from *in situ* observations of the CIMEL thermal-infrared radiometer, model CE 312. These measurements are

complementary to the SST estimations from the moored-buoys of the Institut de Ciències del Mar (ICM) and the Laboratoire d'Oceanographie Dynamique et la Climatologie (LODYC). Accurate estimations of SST are required as input data in the retrieving of SSS and L-band sea emissivities from concurrent sea observations of the fully polarimetric L-band Automatic Radiometer (LAURA) of the Universitat Politècnica de Catalunya (UPC). From 15 November to 23 December 2000 and from 8 to 13 January 2001 parallel observations of L-band, and thermal-infrared sea brightness temperatures were taken at the Casablanca oil platform. In addition to the radiometric data a comprehensive set of ground-truth data were achieved. Amongst them, the next data have been also used in the SST recovery:

- air temperature ( $T_a$ ) and relative humidity (H), which were measured by the four oceanographic buoys of the ICM and LODYC;
- atmospheric pressure ( $P_{atm}$ ),  $T_a$  and H at 30 m height, measured by the meteorological station of the UPC;
- $P_{atm}$ ,  $T_a$  and H at 64 m height, recorded by one automatic meteorological station installed on the top of a communications tower on the Casablanca platform; and

Coincident observations of the AVHRR-NOAA satellite instrument have been provided by LODYC to study the representative character of the punctual CE 312-derived temperatures versus the satellite-derived ones. The different spatial scale of these radiative measurements will permit us to study the spatial variability of SST (patterns of SST variations) in a SMOS pixel.

This chapter provides a brief overview of the radiometric measurements acquired by the UV from the Casablanca platform during WISE 2000. The following sections describe the model adopted to obtain SST observations from CE-312 brightness observations. Here, the problems arising from the recovery of SST under different sky conditions have been described, and the different sources of error have been quantified. The excellent agreement with the satellite derived SST and the oceanographic buoys confirm both the algorithms used and the high accuracy of the radiometric data.

### 2.3.2. Description of the CIMEL CE-312 radiometer

The CE 312 is a portable radiance-based radiometer. It is composed of two major components: (1) the optical head containing the detector (thermopile) and optics, and (2) the electronic unit, which performs the data collection configuration, display and storage. A filter wheel with four interference filters is located between the objective lens and a stepper motor that allows the filter selection. This design includes one broad filter, 8-13  $\mu\text{m}$  (channel 1), and three narrow filters: 11.5-12.5  $\mu\text{m}$  (channel 2), 10.5-11.5  $\mu\text{m}$  (channel 3), and 8.2-9.2  $\mu\text{m}$  (channel 4). Figure 2.7 presents its normalized bands response functions. The radiometer is provided with a concealable, gold coated mirror, which enables

comparisons between target radiation and a reference radiation from inside the optical head. A platinum probe attached to the detector's surface monitors the head's internal temperature and is used to give the reference temperature from which the reference signal is calculated. A second, but external temperature probe can be added by the user into the control unit. It allows collecting the temperature of an external blackbody. The CE 312 has a range of sensed temperature between  $-80^{\circ}\text{C}$  and  $+50^{\circ}\text{C}$ ; it has a radiometric resolution of 8mK for the broad band and 50 mK for other bands (at  $20^{\circ}\text{C}$ ); 1 s of response time; and a field of view of  $10^{\circ}$ . More details on the technical specifications can be found in Pietras et al. [1994] and Sicard et al. [1999].

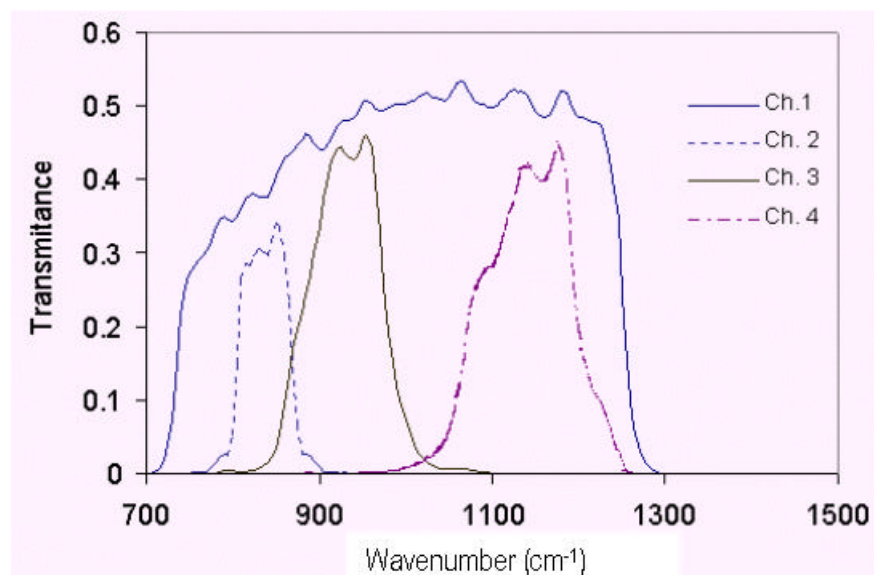


**Figure 2.7.** Normalised spectral response functions for the channels of CIMEL CE-312 radiometer.

The performance of the CE 312 instrument has been regularly checked against a reference black-body for a wide range of temperatures and field conditions. Resulting from these calibration procedures, the temperature of the sample was determined to an accuracy of  $\pm 0.10$  K,  $\pm 0.12$  K,  $\pm 0.09$  K, and  $\pm 0.14$  K for channels 1, 2, 3 and 4, respectively. All channels show similar performance, with no significant bias (below 0.06 K) and accuracies (better than) on the order of  $\pm 0.16$  K.

### 2.3.3. Field Measurement Strategy

The CE 312 head unit together with a video camera were located on the Casablanca terrace, mounted on the Scientific Atlanta pedestal (UPC) besides LAURA and all three looking at the same geometry. Figure 2.8 shows this configuration. The power-driven capability of the Scientific Atlanta pedestal was used to perform scans in elevation and azimuth, with the limitations stemming from measuring from a fixed platform.



**Figure 2.8.** Detail of the housing camera containing the CE 312 optical head and deployed on the Scientific Atlanta pedestal.

As the detector head unit had to work fixed on the pedestal and subjected to open-air conditions, a cylindrical compact external camera housing was used to protect it from these conditions. Thus, it was allocated inside the housing and looking through a ZnSe window 4 mm thickness. This window was selected because its spectral response shows a good transmission in the 8-13  $\mu\text{m}$  spectral region. It has an absorption coefficient of  $0.0005 \text{ cm}^{-1}$  at  $10.6 \mu\text{m}$ , and a refractive index of about 2.39 in the 10 to 15  $\mu\text{m}$  spectral region.

Since the CE 312 read-outs are brightness temperatures, these data had to be corrected from the atmospheric and emissivity effects, before being compared with the SST estimates from the AVHRR and the oceanographic buoys. The strategy we have adopted for determining the SST has been already used in recent studies [Donlon et al., 1998]. It consists of using independent CE 312 brightness temperature observations of the sea and sky in combination with calculated values of the sea surface emissivity. To this end, alternating measurements of sea and sky were performed. During an elevation scan mode, the sea surface was observed downlooking at different viewing angles ( $25^\circ$ ,  $35^\circ$ ,  $44^\circ$ ,  $45^\circ$ ,  $55^\circ$ , and  $65^\circ$  as measured from nadir). Intercalated with these observations, the CE 312 observed radiance from the sky uplooking at the complimentary angles ( $25^\circ$ ,  $35^\circ$ ,  $44^\circ$ ,  $45^\circ$ ,  $55^\circ$ , and  $65^\circ$  from zenith, respectively). Besides, azimuth scans were performed for fixed elevation angles. In this case, the sea observations were made at  $80^\circ$ ,  $110^\circ$ ,  $140^\circ$ ,  $170^\circ$  and  $200^\circ$  azimuth angles, whereas the sky was observed at the complimentary elevation angle. For the about 1 h 15 min that took a scan event, the sea and sky

observations were sampled in a continuous manner (every 2.5 min, with 1'20" integration times). This integration time corresponds to the following acquisition mode: for each of the four channels starting with channel 1, the instrument makes 1 measurement of the detector temperature, and 8 measurements alternating the detector signal (with mirror) and the sample signal (without mirror), all of them in the same channel. The duration of this mode is about 1 min 20 s and the data can be stored in an ASCII file as 4 line, one per channel, with 9 values each one.

With the exception of the measurements performed at fixed elevation and azimuth angles for 30 min, the system pedestal-radiometers rested about 4 min at each selected position, then it moved from its actual position to next position following the scan scheme. This movement between positions also took several seconds. To alleviate these temporal constraints and get the maximum number of valid CE 312 measurements (i.e. for motionless positions of the pedestal), the minimum interval between consecutive measurements (2.5 min) was set for the CE 312.

In the next sections we present the data analysis performed to obtain SST from brightness temperature measurements of CE 312 thermal-infrared radiometer.

#### 2.3.4. Laboratory Calibration of the CE 312 Radiometer

To determine accurate SSTs an absolute calibration of the CE 312 radiometer is required. Since the radiometer was housed inside the cylindrical cover and looking through a ZnSe window, the calibration had to be performed in the above conditions. Besides, contamination of the ZnSe window by seawater, dust particles and salt, can affect the transmission response of the ZnSe window, and cause a degradation of the calibration. Therefore two laboratory calibrations were performed prior to and after WISE experiment.

Calibration exercises consisted of comparing the CE 312-measured radiometric signal and the thermometric temperature of an EVEREST model 1000 blackbody calibration source. They took place along several days measuring mainly during the night in order to reach steady environmental conditions over the temperature interval of interest (10-17 °C). This approach also prevents transient thermal conditions between the black-body calibration source and the environment throughout the measurement time (about 20 sec). The thermometric temperature is collected by using the external temperature probe of the CE 312. Proceeding in this way, calibration is performed assuming that the source is enough close to a blackbody and therefore the contribution of the reflected environmental radiation to the signal is insignificant. Thus, the operation of the radiometer can be precisely checked to within  $\pm 0.3$  °C accuracy

From these calibration tasks a correction function for each thermal channel has been obtained to correct the brightness temperatures, from both miscalibration and the ZnSe window effect. For a non-blackbody sample as the sea surface, this effect is dealt with in a posterior data processing step. Calibration equations were obtained for radiances instead of temperatures and correspond to the following physical relationship (see figure 2.9):

$$R_m = \tau B(T_{bb}) + \rho B(T_c) + \alpha B(T_w) \quad (2.1)$$

where  $R_m$  is the radiance CE 312-measured through the ZnSe window,  $B(T)$  is the Planck function at the temperature  $T$ ,  $T_{bb}$  is the thermometric temperature of the source measured with the external probe,  $T_c$  is the head's internal temperature also registered,  $T_w$  is de ZnSe window temperature, and  $\alpha$ ,  $\rho$  and  $\tau$  are the window absorptivity, reflectivity and transmissivity, being  $\alpha+\rho+\tau=1$ . Then, equation 2.1 can be rewritten as follows:

$$R_m - B(T_c) = \tau (B(T_{bb}) - B(T_c)) + \zeta \quad (2.2)$$

with  $\zeta = \alpha (B(T_w) - B(T_c))$ . Assuming  $\zeta$  is practically constant because it is expected that  $T_c$  and  $T_w$  are similar enough, then we can obtain the calibration equations to correct our measurements. Figure 2.10 illustrates the radiance data from the calibration of the CE 312 channel 1. And Table 2.1 contains the calibration coefficients of equation 2 obtained by linear regression on these data.

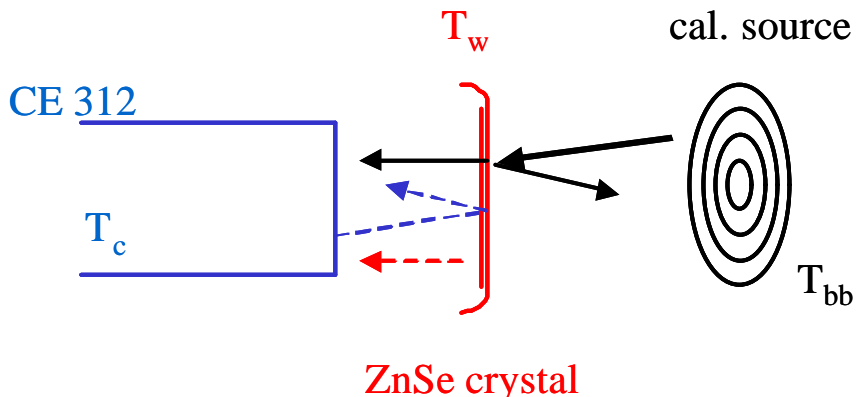


**Figure 2.9.** Diagram of the different contributions to the measured radiance  $R_m$  during the laboratory calibration exercises.

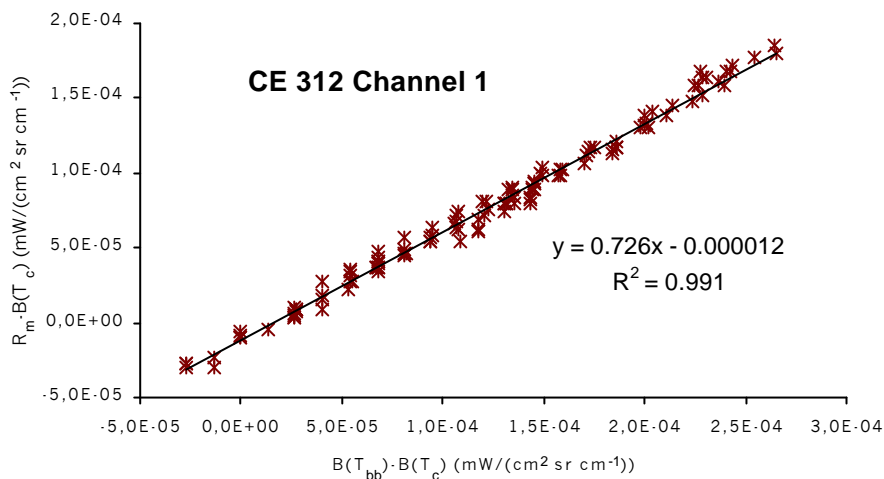


**Figure 2.10.** Scatter plot of the radiance differences measured for the calibration experience of the CE 312 channel 1.

**Table 2.1.** Coefficients of the calibration of CE 312 thermal channels, equation (2.2).

channel	$\tau$	$\pm\sigma(\tau)$	$\zeta(\text{mW}/(\text{cm}^2 \text{sr cm}^{-1}))$	$\pm\sigma(\zeta)$	$r^2$
1	0.726	0.006	$-1.20 \times 10^{-5}$	$9 \times 10^{-7}$	0.991
2	0.735	0.014	$-2.3 \times 10^{-5}$	$2 \times 10^{-6}$	0.955
3	0.745	0.008	$-1.56 \times 10^{-5}$	$1.3 \times 10^{-6}$	0.986
4	0.768	0.018	$-1.8 \times 10^{-5}$	$2 \times 10^{-6}$	0.939

### 2.3.5. Sea Surface Temperature Retrieval

The radiance reaching the sensor when looking at sea surface at an elevation angle  $\theta$ ,  $R(\theta)$ , is composed of three contributions: (i) the sea surface direct emission, which is attenuated by the transmittance of the atmosphere between the sea and the instrument,  $\tau$ ; (ii) the reflection of the downwelling sky radiance ( $L_{\text{sky}}^{\downarrow}$ ) on the sea, also attenuated by the atmosphere; and (iii) the upwelling atmospheric radiance emitted along the viewing direction ( $L_{\text{sky}}^{\uparrow}$ ), on the form

$$R(\theta) = [\epsilon(\theta, U)B(\text{SST}) + (1 - \epsilon(\theta, U))L_{\text{sky}}^{\downarrow}(\bar{\theta}_r)]\tau(\theta) + L_{\text{sky}}^{\uparrow}(\theta) \quad (2.3)$$

where  $B(T)$  is the Planck radiance for a skin temperature  $T$ ;  $\epsilon$  is the emissivity of the roughed seawater;  $U$  is the surface wind; and  $\bar{\theta}_r$  is an effective angle of incidence of the reflected radiance that is close to the viewing angle [Smith et al., 1996; Watts et al., 1996]. Equation 2.3 assumes a horizontally homogeneous sky, such as  $L_{\text{sky}}^{\downarrow}$  only depends on the elevation angle, not azimuth. This is a valid assumption for clear or completely cover skies.

The downwelling atmospheric radiance that is reflected on the roughed sea surface at a local zenith angle  $\theta$  results from the contribution of a region o lobe of the sky which undergoes specular reflection on a roughed surface. The effective angle  $\overline{\theta_r}$ , corresponds to the elevation such that  $L_{\text{sky}}^{\downarrow}(\overline{\theta_r})$  equals to the angular integration of  $L_{\text{sky}}^{\downarrow}$  at different directions that contribute to the signal sensed at  $\theta$  direction.

The surface of a wind-driven sea is made of a distribution of faced slopes, and the sensed signal of this roughen sea is also made of the radiance contributions from the entire distribution of faced slopes. Theoretical calculation of the emission and reflection contributions should consider the sea slope distribution (see e.g. [Cox and Munk, 1954]), should include the effects of shadowing, multiple surface reflections, and consider the anisotropy of the sky radiance. There exists a considerable number of works dealing with this issue [Watts et al., 1996; Yoshimori et al., 1994, 1995]. In this study, the following approximations have been assumed.

**a) Sea surface emissivity calculation.** An approximation to the actual value of  $\varepsilon$  (equation 2.3) has been derived from the seawater emissivities provided by Masuda el al. [1988]. They provide these emissivities for different wavelength, view angles and wind speed, but in their calculations did not consider multiple reflections or rough sea reflectivity. The appropriate channel-emissivity values have been derived for nadir viewing angles between 0 and 85° and for wind speeds in the 0-15 m/s interval. Figure 2.11 shows the angular dependence of these emissivities for different wind speeds and Channel 1 of the CE 312.

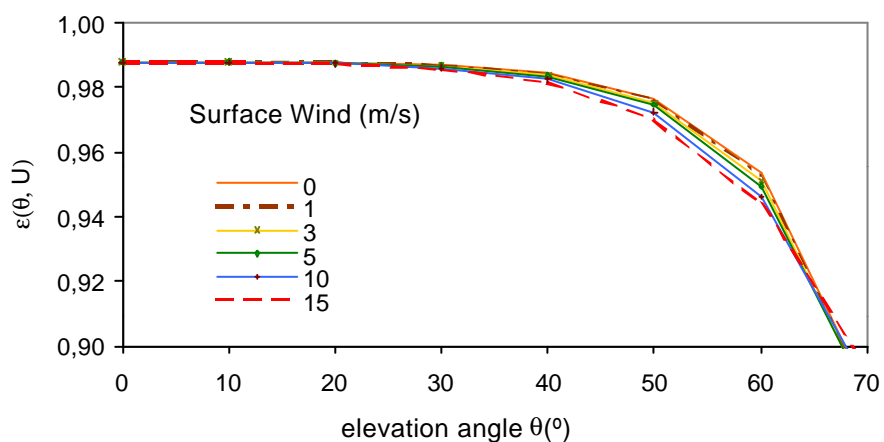


**Figure 2.11.** Elevation dependence of seawater emissivity in the CE 312 channel 1 for wind speeds in the 0-15 m/s interval.

**b) Downwelling atmospheric radiance.** Correcting brightness temperatures from the downwelling atmospheric radiance is hampered by two facts: (i) The anisotropy of  $L_{\text{sky}}^{\downarrow}$  with the elevation angle, and (ii) the roughness of the sea surface. Both circumstances cause the sky region that suffers specular reflection on the sea and leaves it in the sensor direction, contributing to the signal, is a large region, like a lobe. In broken-clouds conditions, the assessment of  $L_{\text{sky}}^{\downarrow}$  can be more difficult and being accompanied of a significant uncertainty. The angle at which  $L_{\text{sky}}^{\downarrow}$  coincides with the total contribution of the atmosphere is known as the effective angle,  $\overline{\theta_r}$ . This effective angle not always coincides with the view angle  $\theta$ . Depending on the viewing angle and the atmospheric conditions,  $\overline{\theta_r}$  can depart more or less degrees from  $\pi-\theta$ . However, a common approximation for the SST retrieval is to take  $\overline{\theta_r}$  equal to  $\pi-\theta$ .

To correct sea brightness temperatures from the sky reflection, CE 312 observations of the sky were performed intercalated between sea observations. These sky scans were not performed at regularly spread angles covering the whole sky. On the contrary, for each one of the sea views only one sky measurement was performed at the complimentary elevation angle (i.e.  $\overline{\theta_r} = \pi - \theta$ ). Figure 2.12 illustrates this strategy, it presents the sky temperature observations performed starting at 00:00 h and finishing at 20:00 h on 15<sup>th</sup> December of 2000. They are mainly at 115°, 130° and 145° views (but also a few at 105°, 125°, 135°, and 155°) and have been used to calculate SST at 65°, 50°, 35° views (at 75°, 55°, 45°, and 25°) respectively. Throughout this day, the sky evolved from completely covert to clear conditions, being partially cloudy during a considerable part of the day. This explains the great variety of sky temperatures. For a completely clear sky (see figure 2.13), brightness temperatures are lower but constant enough with time. Besides, its dependence with elevation is stronger than that for overcast conditions.

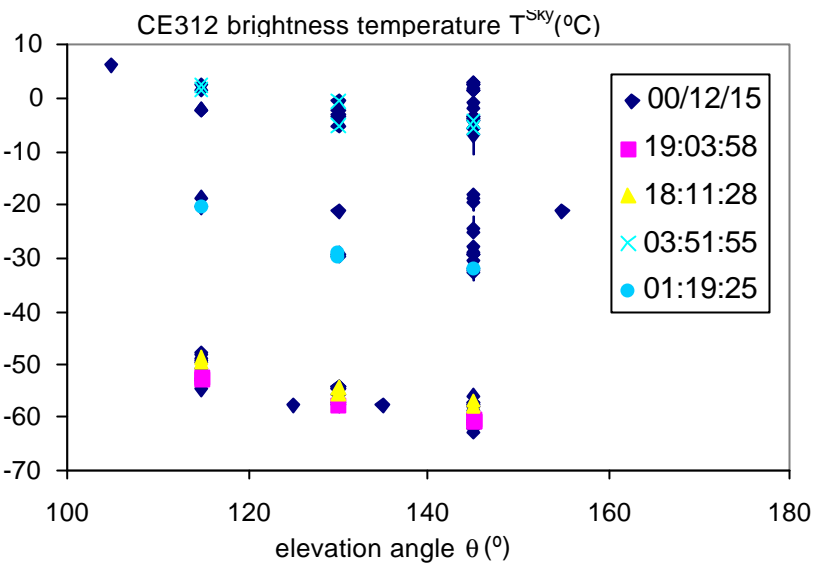


**Figure 2.12.** Sky brightness temperature obtained from CE 312 radiometer on 15<sup>th</sup> December of the 2000. Sky scans at specific times are highlighted.

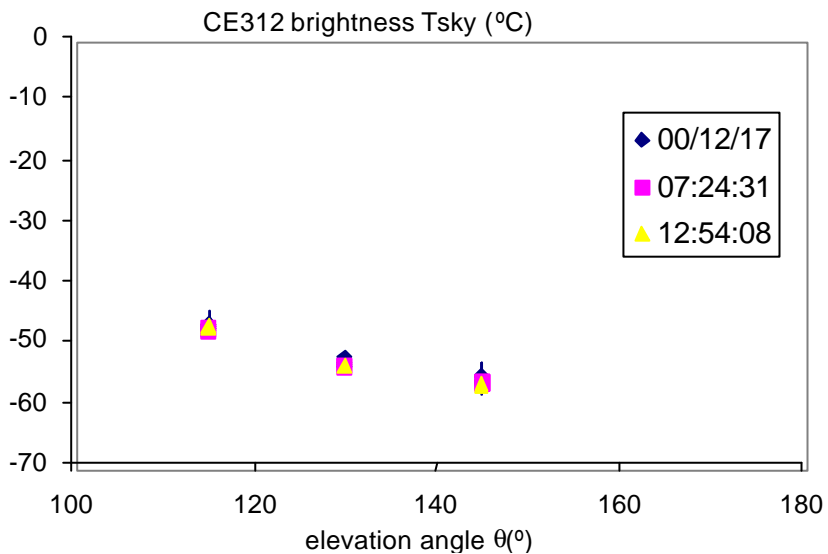


**Figure 2.13.** Sky brightness temperature obtained from CE 312 radiometer on 17<sup>th</sup> December of the 2000. Sky scans at specific times are highlighted.

- c) **Upwelling radiance and transmittance of the atmosphere.** A wide approach when using in situ radiometric observations for the recovery of SST is to neglect the atmospheric emission and signal attenuation effects along the path length between the sea and the instrument. Deployments consisting of radiometers or interferometers onboard of ships are about 10 m of altitude [Smith et al., 1996; Donlon et al., 1998]. The terrace with the scientific Atlanta pedestal and radiometer was allocated 32 m over the sea (a path length of about 75 m for observations at 65° view angle). This

longer path length has led us to check the importance of upwelling atmospheric emission and attenuation of the signal.

Biases of up to 1 K and more can occur in the retrieved SST if these terms are not considered. Figure 2.14 presents the differences between the retrieved temperatures from equation 3 with  $\tau = 1$  and  $L_{sky}^{\uparrow} = 0$  and the actual SST, as a function of the water vapor content of the atmosphere, and for 60° viewing angle in the spectral regions of the CE 312 channels. To perform these calculations we have used the MODTRAN radiative transfer code and 6 different atmospheres, whose water vapor content spread regularly the 0-5 g/cm<sup>2</sup> range. Values of Figure 2.14 correspond to the average of the single differences for SST ranging between 10 and 18 °C and for and the surface wind ranging between 0 and 15 m/s.

Atmospheric conditions in Casablanca place and in November can be modeled as a standard midlatitude atmosphere in winter. This means that biases of up to 0.6 K can result if the view angle is 60°. If we restrict the view geometry to angles below 30°, then we have found that these biases decrease from 0.6 K to ±0.2 K. Therefore, we consider necessary to perform this correction. Thus, we have modeled the upwelling atmospheric radiance and transmittance at 32 m altitude and for the different viewing angles of the observations by using the MODTRAN code with the air temperature, atmospheric pressure and relative humidity measured at 0, 30 and 64 m height. The appropriate broadband channel values of  $L_{sky}^{\uparrow}$  and  $\tau$  have been calculated from the modeled spectral functions of  $L_{sky}^{\uparrow}$  and  $\tau$  and the filter functions of the CE 312 channels. The availability of these meteorological data as continuous temporal series would allow us to obtain representative values for individual observations (every two minutes approximately). This procedure represents a great volume of computations. To optimize this task, we adopted the approach of defining representative values of  $T_a$ ,  $P_{atm}$ , and  $H$  to being representative of stationary weather conditions. In this way the number of simulations have been reduced significantly to 3-4 cases per day.

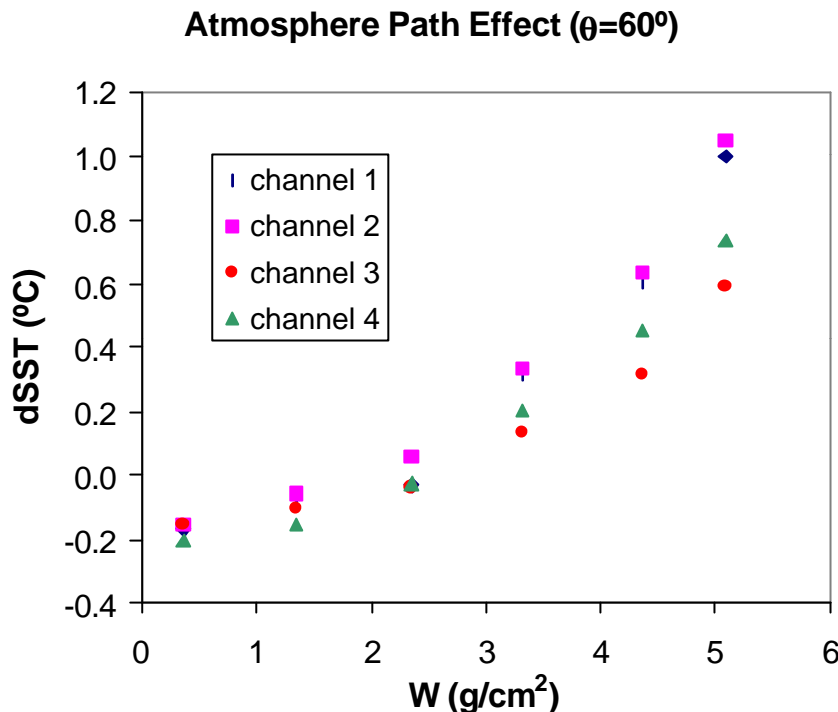


**Figure 2.14.** Biases in the SST retrieval resulting from no correcting from the atmospheric emission and attenuation along the path length sea-sensor versus the total water vapour content of the atmosphere. dSST stand by the difference approximated SST and actual SST. These values are average differences for SST ranging between 10 and 18 °C and surface wind ranging between 0 and 15 m/s.

**d) Viewing geometry.** A first preliminary treatment of the sea surface data was performed in order to identify the appropriate viewing conditions for the SST retrieval. Some suggestions on this issue have been previously indicated in Donlon et al. [1998] and Donlon and Nightingale [2000]. In this point we want to highlight the importance of the observation geometry to overcome problems derived from inaccurate estimations of sea emissivity and atmospheric terms. Results from this preliminary study are shown in Figure 2.15. It contains the retrieved values of SST obtained from channel 1 observations following the above indicated methodology. It is immediate to see that for view angles greater than 35°, SST values deviates from the actual thermodynamic temperature. As view angle increases, also the SST error increases (up to more than 0.7 K for 65° view angle and in critical conditions). Although sea state and atmospheric conditions affect the definitive error of the SST. This influence can be significantly reduced if the appropriate view geometry is used. This result is in total agreement with what we expected, if we keep in mind the emissivity and atmosphere dependences on the view angle.

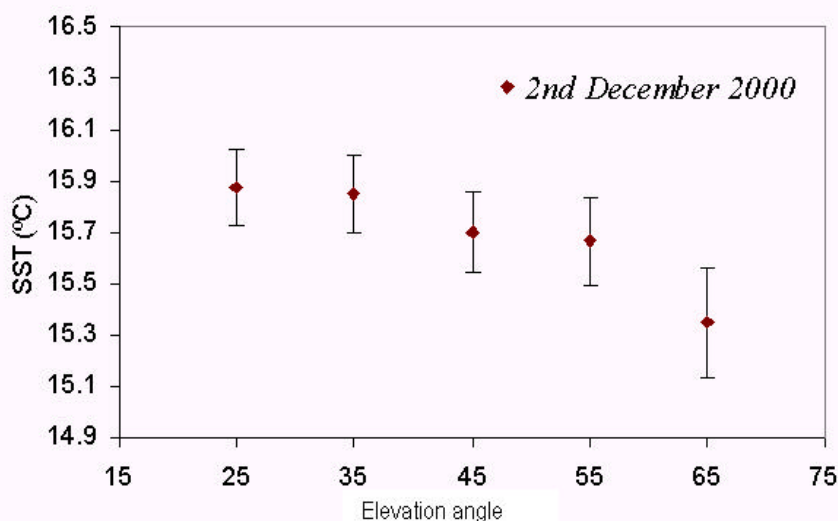


**Figure 2.15.** First preliminary SST values retrieved from an elevation scan which was performed on 2<sup>nd</sup> December 2000. The slight dependence on the elevation angle is in a critical part due to using no appropriate emissivity values for angles greater than 30°.

### 2.3.6. SST Processing and Assessment

Brightness temperature processing to obtain actual SST is based on the above exposed methodology. In a first step, each one of the sea observations was flagged with the data, time, elevation and azimuth angles. Then, those data corresponding to an elevation angle of 25° or 35° and performed in channel 1, were selected for the retrieval of actual SSTs. Next step was to assign a surface wind speed to every one of the measurements. Here, the surface wind estimations provided by LODYC people were used (section 2.2). This parameter is necessary to obtain the seawater infrared emissivities [Masuda et al., 1988].

A key issue of this study is to evaluate the accuracy of our SST determinations. This point involves questions such as the identification of the different sources of errors; the estimation of their magnitude; and finally a discussion on the dependence of these errors and the way of minimizing them.

Uncertainties of input parameters as well as of the numerical approaches result in random errors. This kind of errors can be easily estimated by applying error theory. These errors are related with the sensitivity of the method to changes in a parameter. They are important because they can help us to identify the best conditions to deploy our experiment. Besides these random errors, biases (positive and negative differences) can be due, for instance, to implicit assumptions on the physical model used, incorrect sea emissivity values or inappropriate measurements of sky radiance.

It is worth noticing that propagation of emissivity and sky radiance errors on the SST calculation is greatly conditioned by the observing strategy and instrument geometry and alignment [Donlon and Nightingale, 2000]. Thus, for nadir angles higher than 30°, emissivity begins to decrease having a strong dependence on pointing, but also wind effects on emissivity can be significant for these angles. With other factors also influencing the error magnitude we cannot decide on. For example the atmospheric conditions, completely covered skies represent the ideal conditions to perform SST observations. In this sense, Donlon and Nightingale [2000] remark that, under cloudy skies the sensitivity to roll is small, but under clear skies, the error in the orientation of the radiometer must be less than 5° for the magnitude of the SST error to remain below 0.1 K. Therefore, selecting a good observing strategy we can avoid a lot of problems derived from wind and sky radiance anisotropy and at the same time we can minimize biases from using an approximate model of the radiative properties of sea surface. Now we are focusing on random error from the following source of error:

- a) *Calibration Accuracy.* First point in the data processing was the calibration of the CE 312 measured signal,  $R_m$ , to correct from the ZnSe window attenuation. This correction was performed by applying equation 2.2. Therefore, error in  $T_{bb}$  has been calculated from the radiometric accuracy of Ce 312 (see Section 2.2), and errors due to the linear regression of equation 2 (see  $\sigma(\tau)$  and  $\sigma(\zeta)$  in Table 2.1). Thus,

$$\sigma(T_{bb}) = f(\sigma(R_m), \sigma(\tau), \sigma(\zeta)) \quad (2.4)$$

- b) *Emissivity Errors.* Sea surface emissivity has been calculated from values presented by Masuda et al. [1988] for different surface wind speeds and nadir angles. The appropriate value of emissivity was calculated by interpolating in the Masuda et al. emissivity table. Therefore errors in emissivity are due to both pointing and wind speed errors, as follows:

$$\sigma(\varepsilon) = \sqrt{\left(\frac{\partial \varepsilon}{\partial U}\right)^2 \sigma^2(U) + \left(\frac{\partial \varepsilon}{\partial \theta}\right)^2 \sigma^2(\theta)} \quad (2.5)$$

We calculated this error assuming a pointing error up to  $\pm 5^\circ$  ( $\pm 0.09$  rad) for every sea surface measurement, resulting in a negligible error ( $< 1 \times 10^{-4}$ ). However, it is worth to note that Masuda et al.'s model constitutes a first approximation to the actual emission of a wind roughed sea surface. Then, we have to model more reliable emissivity errors, taking into account that wind effects on emissivity are insignificant for  $\theta < 30^\circ$  [Watts et al., 1996]. In this sense, Donlon and Nightingale [2000] conclude that, under cloudy skies the sensitivity to roll is small, but under clear skies, the orientation of the radiometer must be known to better than 5° for the magnitude of  $(\partial SST/\partial \varepsilon)\sigma(\varepsilon)$  to remain below 0.1 K.

The surface wind  $U$  is fully determined by wind at 69 m altitude ( $U_{69}$ ) being provided by the meteorological station anemometer. So, error in  $U$  is also fully determined by the precision of this anemometer (about  $\pm 1\text{-}2 \text{ m/s}$ ). Therefore:

$$\sigma(U) = \left| \frac{\partial U}{\partial U_{69}} \right| \sigma(U_{69}) \quad (2.6)$$

- c) *Downwelling Atmospheric Radiance Errors.* Donlon and Nightingale [2000], show that inappropriate measurements of sky radiance can have their origin in: (i) incorrect radiometer view geometry (pointing); (ii) temporal mismatches between the sea surface and atmospheric views; and (iii) the effect of wind on the sea surface. It can be really difficult to assess the precision when measuring  $L_{\text{sky}}$ . In effect, under moving or cloud-broken skies, sky temperatures can change quickly, then the uncertainty associated to these measurements, increases certainly. An assessment on this uncertainty is possible by performing continuous in time measurements of  $L_{\text{sky}}$  and analyzing changes between consecutive measurements. Errors due to incorrect radiometer view geometry or due to the effect of wind on the sea surface are equivalent to errors due to measure at a wrong  $\bar{\theta}_r$ . This error can be minimized selecting the appropriate geometry of observation. For a homogeneous sky, and view angles near the zenith (about  $\theta < 30^\circ$ ) there is not a significant anisotropy of the sky on the elevation. So a pointing error of  $\pm 5^\circ$  has no significant consequences on the SST value than the same pointing error when measuring at  $50^\circ$ . On the other hand, propagation of  $L_{\text{sky}}$  and emissivity errors on the SST depends in part on the difference between the sky and the sea brightness temperatures. If both temperatures are similar, then this error reduces significantly. In conclusion, maximum error on SST will result from the combination of a clear sky, with a high nadir view and wind speeds of about 10 m/s.
- d) *Variability of brightness temperatures.* Depending on the viewing angle, sea surface brightness temperatures are more or less variable, for the same external conditions. In effect, continuous measurements of SST performed in identical conditions show the uncertainty of SST increases as the view angle increases.

### **2.3.7. Inter-comparison between CE312-calculated, buoy-measured and AVHRR-observations of the SST**

Actual SST and its total error have been calculated from the CE 312 radiometric measurements and the meteorological parameters done during WISE 2000 campaign, from 15 November to 23 December 2000 and from 8 to 13 January 2001. Only SST observations performed at  $25^\circ\text{-}35^\circ$  have been used for SST retrieving. In these viewing

conditions, SST error are in general below  $\pm 0.2$  K. These results have been compared with the sea temperatures registered by the oceanographic buoys of ICM and LODYC and the AVHRR observations obtained by LODYC for four different dates. Figure 10 shows this comparison. The agreement of the sea temperatures in general is excellent. The differences between buoy-SST and CE 312-SST range between 0.05 and 0.3 K which are consistent with previous observations. This discrepancies are believed to be due to the skin effect. For the four coincident AVHRR images, the average difference between the CE312-derived SST and the AVHRR-observations is  $-0.05$  K, which is negligible in relation with the uncertainty of  $\pm 0.1$ -  $0.2$  K of the CE-312 temperatures.

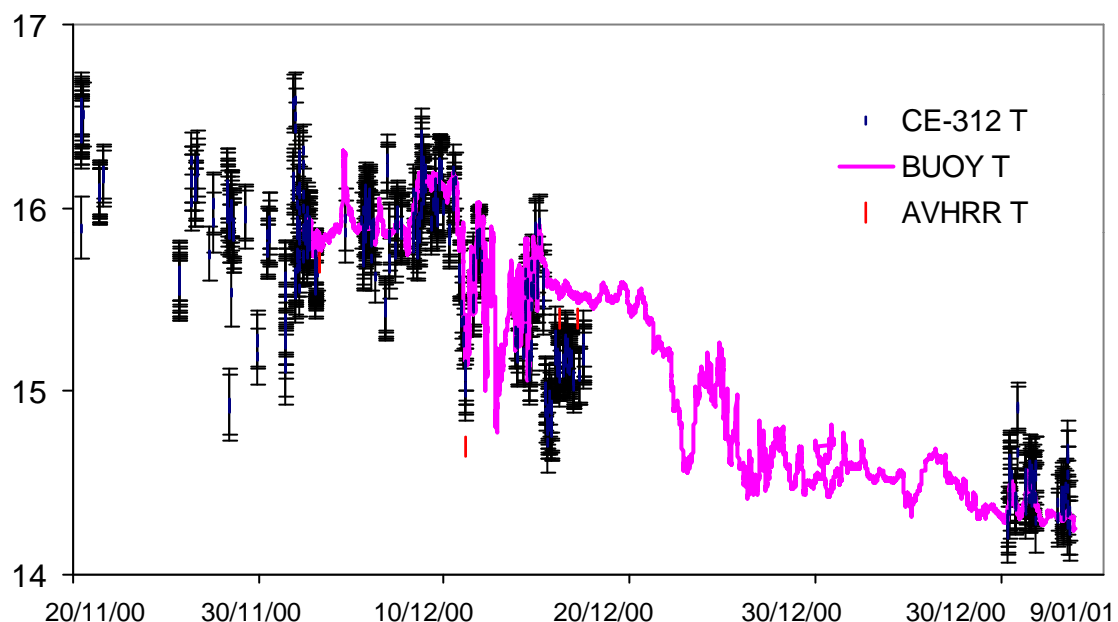


**Figure 2.16.** Comparison between the SST observations registered by the oceanographic buoys of ICM and LODYC and the retrieved from the CE 312 radiometric measurements performed in the 8-12  $\mu$ m region and at  $25^{\circ}$ - $35^{\circ}$  elevation angle.

We have presented the measurement strategy and the processing of the sea surface temperature measured during WISE 2000, using the CE-312 infrared radiometer mounted on the Casablanca terrace. Intercomparisons of buoy-based measurements with determinations from radiometer-based observations indicate that an absolute accuracy of 0.2 °C or better may be possible. For near-nadir measurements where the surface emissivity is nearly constant, the Masuda et al. [1988] values of surface emissivity should be sufficient for accurate SST determinations. At large viewing angles where the surface emissivity varies greatly with sea state and the emitted and reflected sky radiation become a significant contributor to the signal, then more exact values of emissivity are required to derive accurate SST. Thus, a pragmatic approach to alleviating the majority of errors associated with observations at large viewing angles is to restrict to use only near-nadir observations ( $\theta$  below  $35^{\circ}$ ) for recovering the sea surface temperature and then to use observations at larger viewing angles to get the angular variation of emissivity. A first look

at this last activity has revealed that sea emissivity at large angles should be a little higher than the values proposed by Masuda et al.[1988].

A key aspect of this work has been the identification of the different sources of errors in retrieving SST. Effects from inappropriate downwelling sky radiance have been assessed taken into account the sky conditions (differencing between clear, overcast, broken-cloud skies). In this sense it has been shown that overcast skies represent the best conditions for measuring, whereas clear skies stresses the necessity of measuring at near-nadir angles, where anisotropy is smaller. More critical are the measurements performed under broken-cloud conditions, then we propose to estimate the associated error from dispersion in time of the sky temperatures. Also in this work we have proved the necessity of correcting from the atmosphere along the path length sea-sensor (in this case this path length is between 32 and 75 m). To obtain the atmospheric radiance emitted upward and the transmittance, we propose to use collocated atmospheric parameters measured near the surface by a meteorological station. Thus values of air temperature, atmospheric pressure and relative humidity are enough to calculate this correction.

## 2.4 Analysis of sea state

### 2.4.1 Analysis of significant wave height measured by buoy 2 (ICM)

The failure of buoy 3 after the first deployment attempt (see Data Acquisition Report) resulted in a lack of wave rider data. Only significant wave height and period, at a sampling rate of 2 minutes, were recorded by buoy 2 sensors. In addition to that, the reported problem on a connector in buoy 2 resulted in these wave data being only available from December 13 to the final recovery of the moorings (January 20). During these five weeks significant wave height ranged from 0.1 to 4 m, with an average of near 1 m. Wave periods ranged from 1.6 to 7.5 s, with an average of 3.2 s.

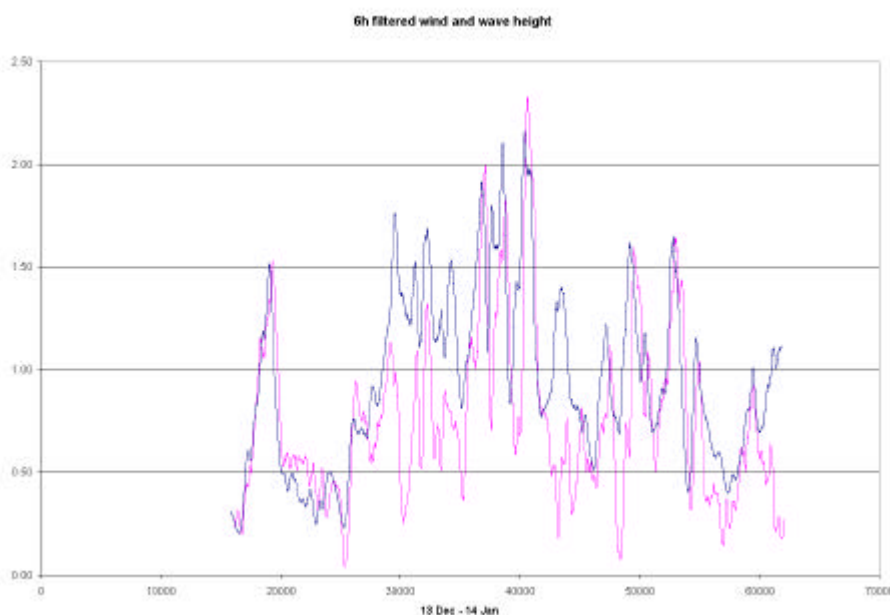


**Figure 2.17.** Low passed (6h filter) wave height (blue) and wind speed (pink) for the period December 13 to January 14

Most of the time wave height is correlated to wind stress. This means that waves are mainly due to local wind and hence wind speed values, with the adequate correction for the presence of foam, can be used as a parameter for the determination of surface roughness in the models of sea surface emissivity. However, as seen in Figure 2.17, some times during WISE 2000 considerable wave heights were recorded without simultaneous high wind (records around 3000, 4300 and 6100 in the figure). This is an indication that the wave field at the Casablanca site was at that moment not originated by local winds, but arrived there from external areas (swell). This is also an important issue to be solved for SMOS salinity retrieval, if wind speed information has to be used in the computation.

#### 2.4.2. Analysis of stereo-camera data

During WISE 2000 experiment from November 16 to December 17 two numerical stereo camera looking at the surface from the Casablanca platform were dedicated to sea surface elevation estimation using a surface elevation estimate with a stereo algorithm. The level of observation was 25.8 m from the surface and the camera were slanting at 15.1 degrees from the horizontal plan. The horizon determination is used to recover the camera positions if either the camera angles have any drift as a function of time and if the platform presents some oscillations as a function of time. Each camera has typically an angle of view of 37.86°X28.96°. The lens dimension is 10.4 dia. X 27.5 (D) mm. The number of pixel in the pictures are 832X624.

The objectives of the sea surface elevation estimate and breaking estimate (computed with the cameras) is to give information about the surface from the L band radiometer on board the platform (Polytechnic University of Catalonia) and looking the surface. This information is intended to be used to correct the radiometer brightness temperature to derive Sea Surface Salinity SSS and Sea Surface Temperature SST.

Have participated to the experiment on the Casablanca platform for the Stereo program: Dr Jacqueline Boutin ( LODYC, Paris Jussieu) from November 28 to December 15 and Dr. Alain Weill ( CETP, Velizy) from November 13 to November 28. From December 15 to December 17 the system was in charge of R. Villarino and L. Enrique (UPC, Barcelona)

CETP was responsible of:

##### 1) Data acquisition of digital pictures of the surface from the Casablanca Platform:

An amount of around 6000 couples of pictures were acquired and indications about pictures performed is given in the Data Acquisition Report distributed to the WISE participants (<http://dataserv.cetp.ipsl.fr/WISE/>). To get a clearer idea Figure 2.18 presents a set of samples of stereo images collected.

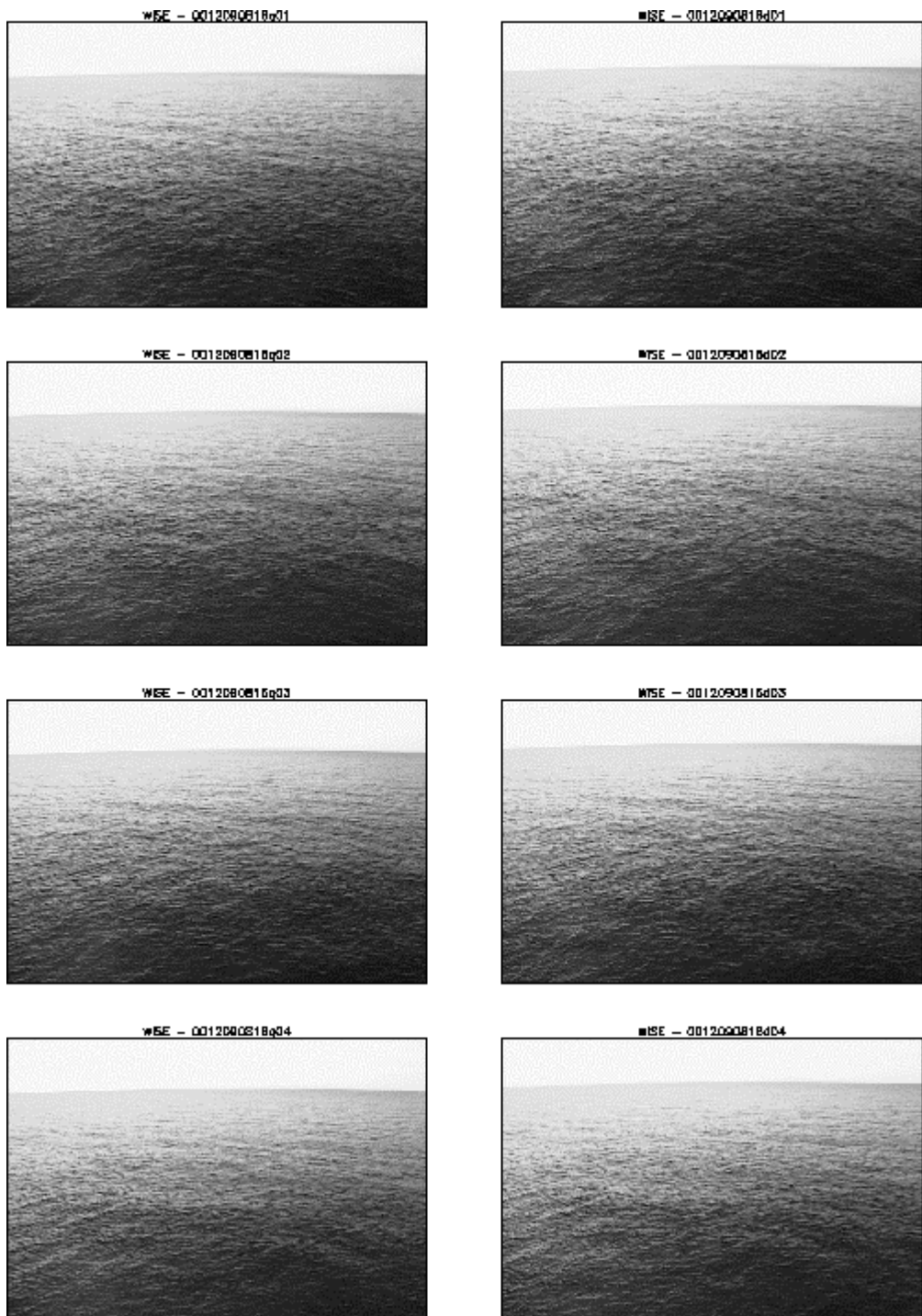


**Figure 2.18.** Samples of stereo-images used in the analysis

Figures 2.19 and 2.20 present two examples of different wind and foam conditions showing the complexity of the topography due to the presence of swell and the reflections on the platform structure which affect both the foam coverage and the surface topography.



**Figure 2.19.** Picture acquired on 12/15/2000  
Foam, wind and complex topography



**Figure 2.20.** Picture acquired on 12/08/2000  
Calm sea, no foam, complex topography

## 2) Estimation of the percent of breaking at the sea surface.

The analysis has been performed followed with an estimate of the relationship between foam percent and wind speed (Figure 2.21).

slope 3.5 ( large scatter as found generally)  
theoretical slope ( 3.) but observed slope in agreement  
with Monahan and O'Muircheartaigh, 1980 who found a 3.4  
power with mean wind.

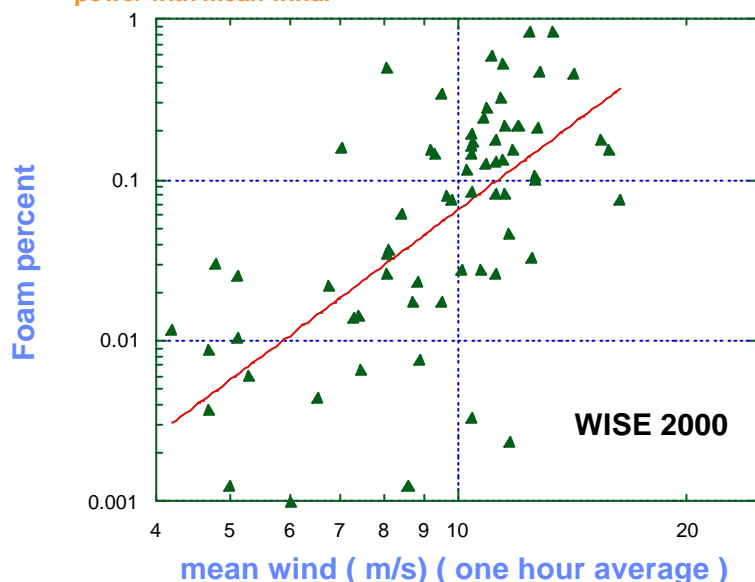


**Figure 2.21.** Relationship between foam percent and wind speed as derived from the stereo-camera (pointing to the North)

It has been found that:

$$\begin{aligned} \text{Foam percent: } C_f &= 1.8910^{-5} U^{3.53} \\ \text{Standard deviation of foam percent: } s_{C_f} &= 0.000119 U^{2.8} \end{aligned} \quad (2.7)$$

*This estimate which is rather low corresponds to the observations made "de visu" that the breaking was smaller in the North of the platform than westerly. This can be explained by wave reflection which prevent the incoming waves from becoming very unstable, or which stabilizes the incoming wave. This seems indeed confirmed by the complexity of the wave spectrum built with the stereo effect, which shows different modal behaviours.*

*It has to be noticed that due to the height from which the wind was measured on the platform we had to imagine an algorithm able to determine the surface wind: If the surface layer depth is  $h_{sl}=10 U_{10m}$ , the logarithmic wind profile is computed from the tower observation and if the tower height is smaller than  $h_{sl}$  one have to suppose that the tower observation is in the mixed layer: therefore this height is affected to the be identical to the surface layer depth. Diabatic conditions cannot be computed since  $T_{air}$  is not locally measured. However this algorithm enable us to estimate the neutral wind speed at the surface level (10 m).*

Another estimate which is uncommon in the literature but which has been thought to be useful is the statistics about the foam percent which has been systematically estimated and justifies the standard deviation estimate as a function of mean wind speed. Relatively new is the fact that the power law is not very far from the mean wind speed at power 3.

### **3) Estimation of the elevation of the surface, height variance and spectral information.**

It has to be noticed that one estimate of the surface elevation lasted several minutes in CPU and more than 3000 coupled of pictures were processed (see the web report which gives examples, the different data obtained, how they can be read and the document by Georges Luc Kalpaktchioglou given in the file WISEDEF.PCT/Report\_eng\_soft.ps.gz. The stereo programs have been developed at CETP by Christine Guerin (CETP) and Emmanuel Chaumont during his engineer scholar stay at CETP. The web server and the data access have been developed by Sophie Cloché (CETP).

Note that the reconstruction of the surface is not always possible (bad contrast, surface too flat to have relevant homologous points, sea birds). An index of quality has been added to the catalogue. Several aspects of the surface topography have been obtained: surface elevation and elevation variance, 1D omnidirectional spectra and 2 D spectra. Figures 2.22, 2.23 and 2.24 show typical examples of these three parameters.

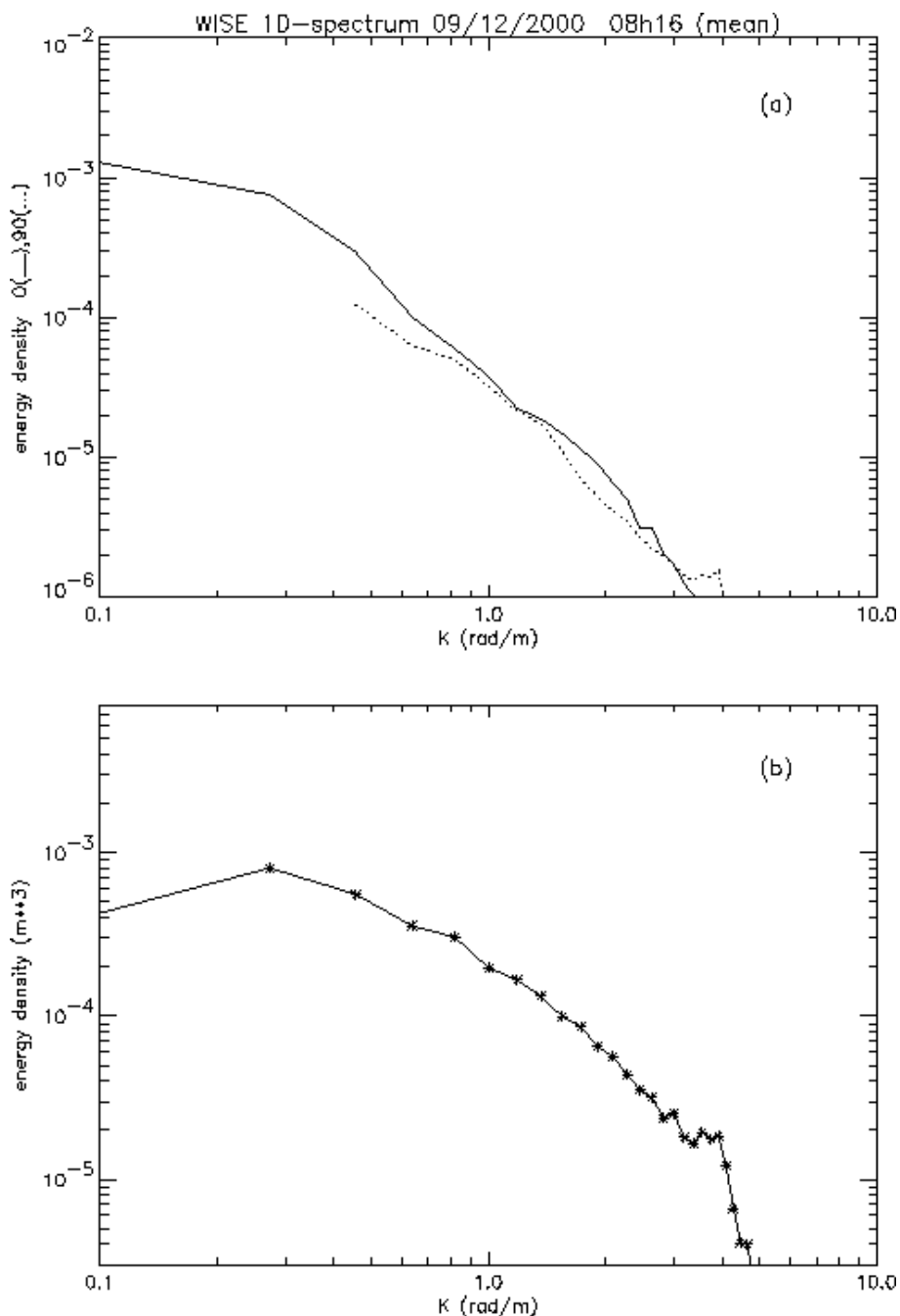


**Figure 2.22.** Typical example of 1D omnidirectional sea surface spectrum as derived from CEPT stereo-cameras during WISE 2000 campaign.

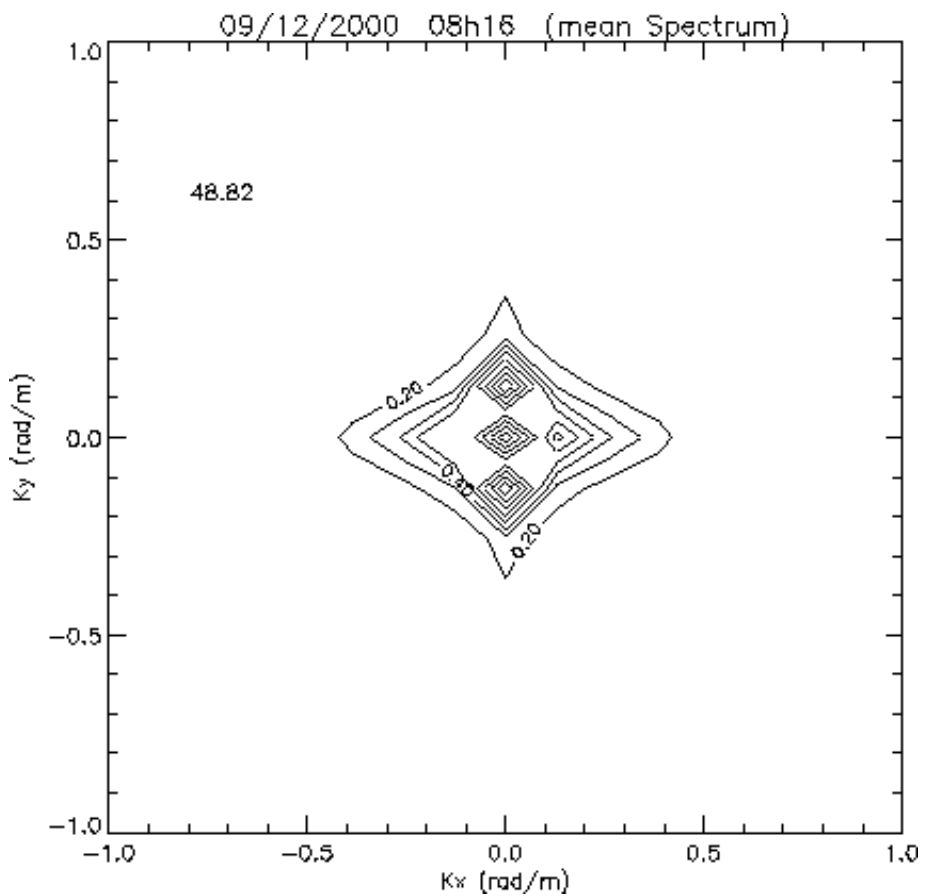


**Figure 2.23.** Typical example of 2D directional sea surface spectrum as derived from CEPT stereo-cameras during WISE 2000 campaign.

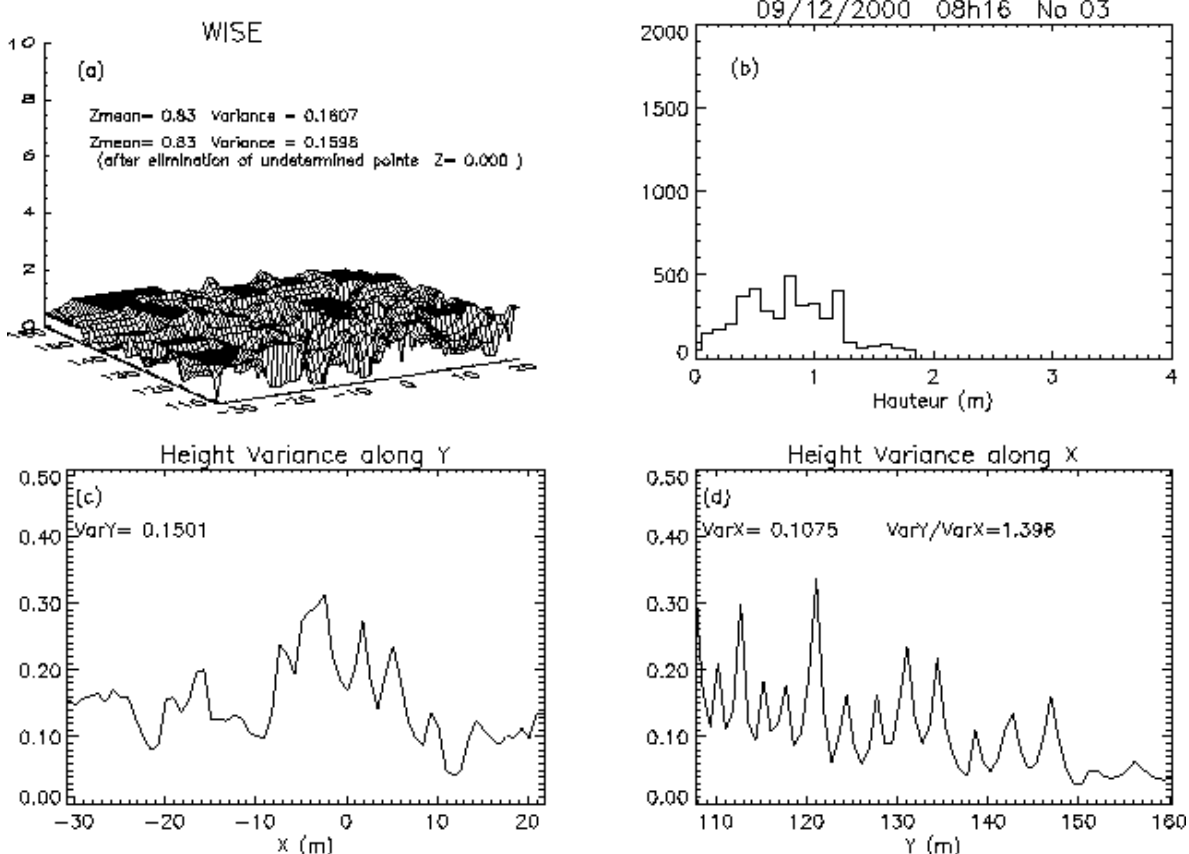


**Figure 2.24.** Typical sea surface topography and height variances along the directions parallel (X) and perpendicular (Y) to the platform derived from CEPT stereo-cameras during WISE 2000 campaign.

*It is observed that during the campaign the spectrum in the range between typically a few meters to 10 m is very complex showing the influence of reflecting waves, while between typically 2 m to 6 m it becomes more and more isotropic.*

#### 2.4.3. Analysis of video imagery from antenna boresight

In addition to the IR radiometer (UV), a video camera (UPC) was mounted on the antenna pedestal in order to get real time imagery of what was being measured by the L-band radiometer. The sea foam coverage is then determined from images not only from the geographic North, as in the case of the stereo-cameras, but from a range of azimuth angles from about 110° West to 40° East, but mainly from the West, since it was the direction less sensitive to radio-frequency interference.

Two different analysis have been performed: i) determination of the sea foam coverage as a function of the wind speed, and ii) determination of the time constant at which the foam path disappears.

The determination of the foam coverage from the video images is as follows:

- First, the images are truncated to the antenna half-power beamwidth, as indicated in Figure 2.25.
- Second, the area corresponding to each individual pixel in the image is determined from the geometry of observation (camera height over the sea and angle of incidence of the center of the image, the same as that of the radiometer).
- Third, each photograph in the image is converted to grayscale, and its histogram computed.
- Fourth, pixels with a gray level higher than a certain threshold are assigned as covered by foam, while pixels below that threshold are assigned as water. The threshold is determined for each series of photograph, since it depends on the illumination conditions.
- Fifth, the ratio total area of pixels covered by foam to total area (Figure 2.25) is the instantaneous foam coverage.
- The process is repeated for all the photographs (acquired every second) during the approximately 30 min period that last a full measurement sequence and the mean foam coverage is computed.

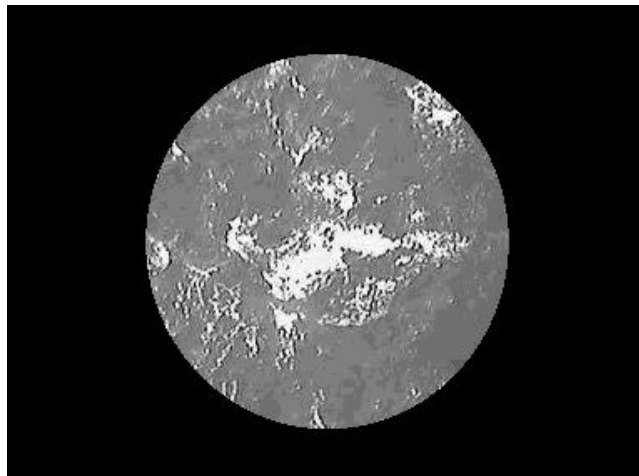


**Figure 2.25.** Photograph from antenna boresight ( $\theta=25^\circ$ ) truncated to the antenna half power beamwidth

Figure 2.26 shows the instantaneous foam coverage corresponding to the sequence acquired around the 13 h, during December 15<sup>th</sup>, 2000. The minimum and maximum values are 0.0025% (Figure 2.27a) and 22.19% (Figure 2.27b), depending on whether or not the wave broke in front of the antenna boresight. This is a extreme case of high winds and low incidence angle ( $\theta=25^\circ$ ), at lower winds the variance is lower and so is at higher incidence angles because of the averaging of many breaking waves (Figures 2.27 c and 2.27 d).

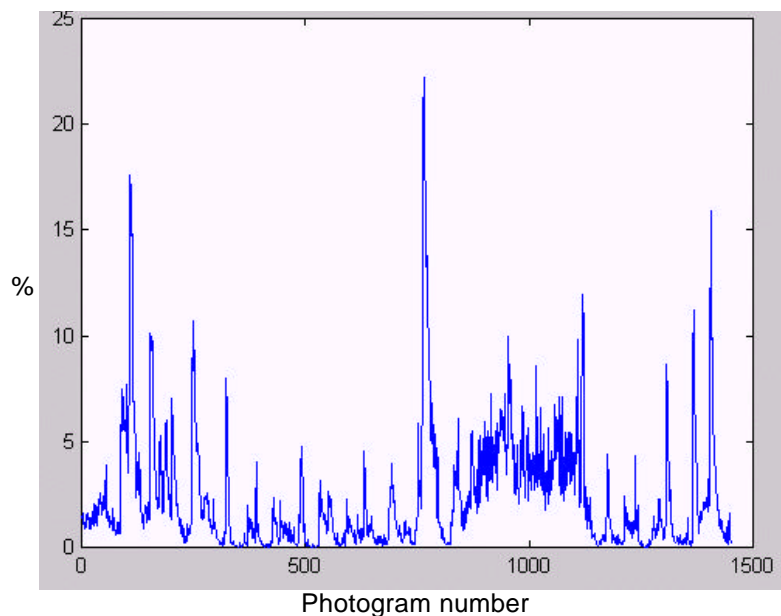


**Figure 2.26.** Example of instantaneous variation of sea foam coverage (%) within antenna footprint.

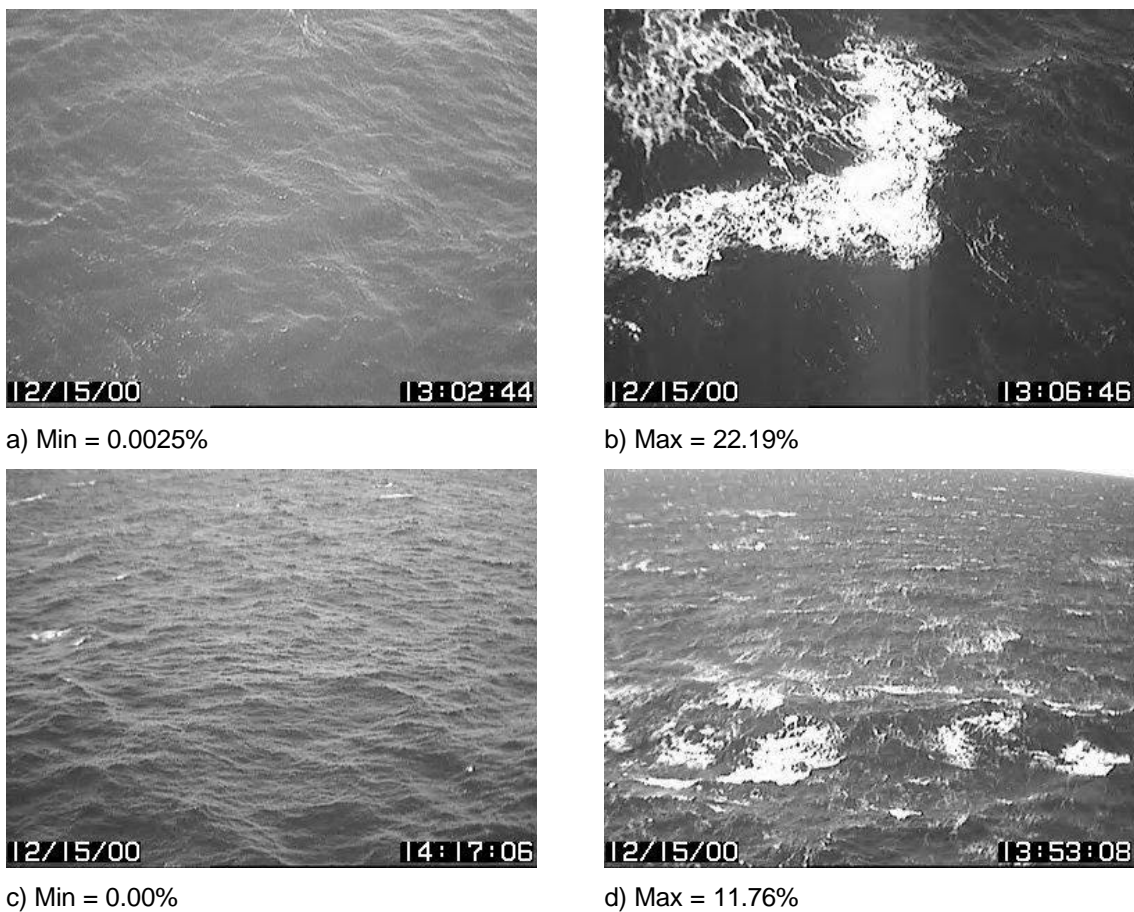


**Figure 2.27.** Sample images of maximum and minimum sea foam coverage during a scan (two different incidence angles: a-b  $\theta = 25^\circ$ , c-d  $\theta = 65^\circ$ ).

The total number of photographs analized is 19.577. The mean wind speed, referred to 10 m, corresponding to the same period is also computed. Figure 2.28 shows the relationship between the sea foam coverage ( $C_f$ ) and the mean wind speed. The diamonds represent the average value of  $C_f$  and the bars are plotted at plus minus one standard deviation of the series (see e.g. Figure 2.25). The linear regression of the scatter plot in logarithmic scale (Figure 2.29) leads to the following equation.

$$C_f = 2.32 \cdot 10^{-4} U_{(10)}^{3.4988} [\%] \quad (2.8)$$

Note that the exponent of  $U_{(10)}$  equation is almost exactly the same as the one found in section 2.4.2. The value of the constant is also in agreement with the results of Monahan and Lu [1990], but is about a factor of ten higher than the value found in 2.4.2 which, as discussed previously, may be due to the stabilization of the wave due to the interaction between the incoming wave and the wave reflected one the north side of the platform.

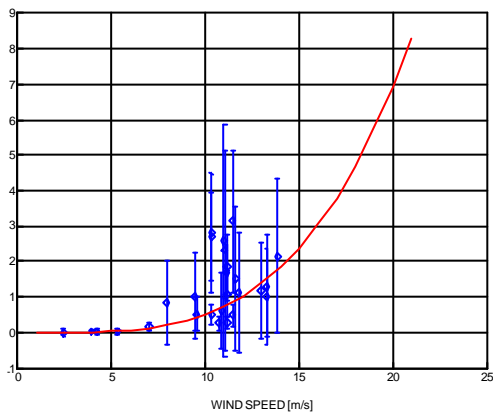


**Figure 2.28.** Foam coverage (%) and 1-sigma standard deviation bars derived from UPC video camera mounted on antenna pedestal (linear scale).

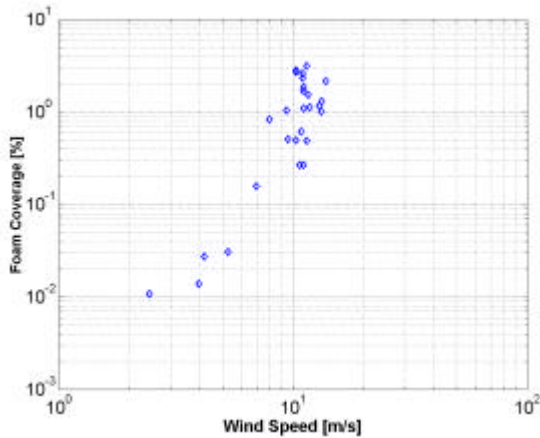


**Figure 2.29.** Foam coverage (%) derived from UPC video camera mounted on antenna pedestal. In logarithmic scale the scatter plot is fit by a line with slope 3.4988, in agreement with Monahan and Lu and Weill.

The determination of the time constant at which a foam patch disappears is similar, but the series of photographs have to be inspected so as to determine those in which there is only a patch and it appears in at least 3 consecutive photographs. The last condition has restricted the analysis to low wind conditions, since for high winds: i) the patch was too large (e. g. Figure 2.27b), ii) it was not possible to isolate single patches (e. g. Figure 2.27d), and/or iii) the patches were not present in 3 consecutive photographs.

Finally, the instantaneous foam coverage is fitted by an exponential function with adjustable time constant  $t$ . The results show a time constant of  $t = 3.15 \pm 0.70$  s, approximately, lower than the 3.5-4.3 s value given by Monahan and Lu [1990], which may be explained by the lower sea temperature. Figure 2.30 shows a series of 4 photographs used in one analysis, starting with a wave breaking and disappearing gradually.

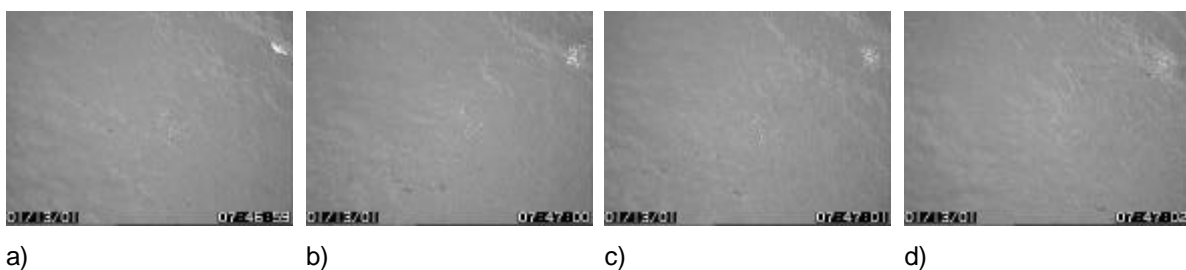


**Figure 2.30.** Foam coverage decay in a series of consecutive photograms.

### 3. Analysis of satellite imagery

Satellite imagery was used to locate the punctual in-situ measurements in their context. For that purpose ocean color from Seawifs and AVHRR SST images enabled us to monitor (cloud coverage permitting) the Ebro river plume, while QUIKSCAT wind speed measurements gave indications on large scale gradients and a cross check of the in-situ wind measurements.

#### 3.1. Analysis of ocean color

Images at 2 kilometer resolution processed as described in Melin et al.[2000] were provided by F. Melin (Space Application Institute, Joint Research Center, Ispra, Italy).

For the case of 26 December 2000 shown below, the Ebro plume which is seen as an enrichment in chlorophyll, probably partly because of increased turbidity, reaches the Casablanca platform as confirmed on in-situ SSS measurements (low salinity). The Ebro plume comes or not to the platform under the influence of changing local currents.

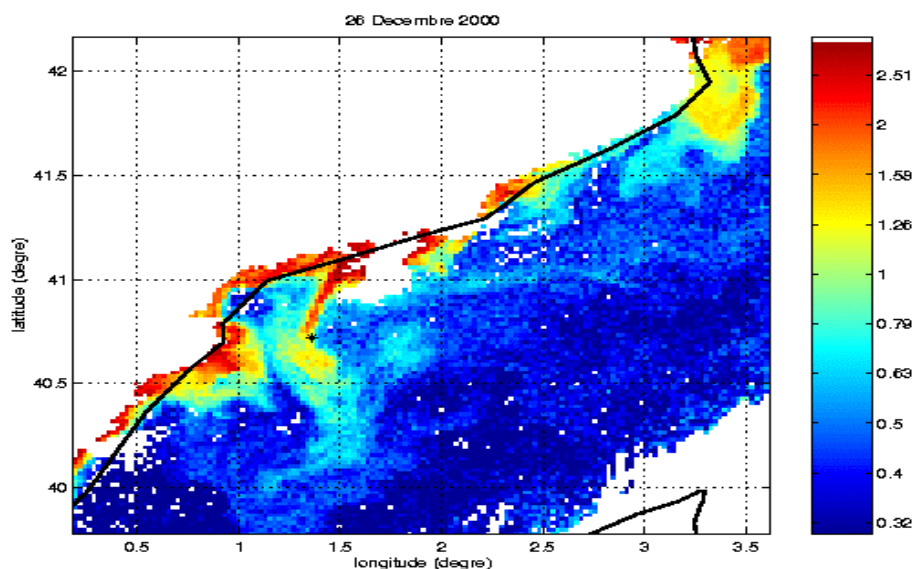


**Figure 3.1.** Seawifs chlorophyll image of the platform region on December 26.

### 3.2. Analysis of AVHRR imagery

The Ebro plume can also be seen on SST images as low temperature water as can be seen on two occasions shown below: December 11 and December 26. The AVHRR data at 2 kilometers resolution were provided by the SATMOS data center (Service d'Archivage et de traitement meteorologique des observations spatiales, Meteo-France/CNRS).

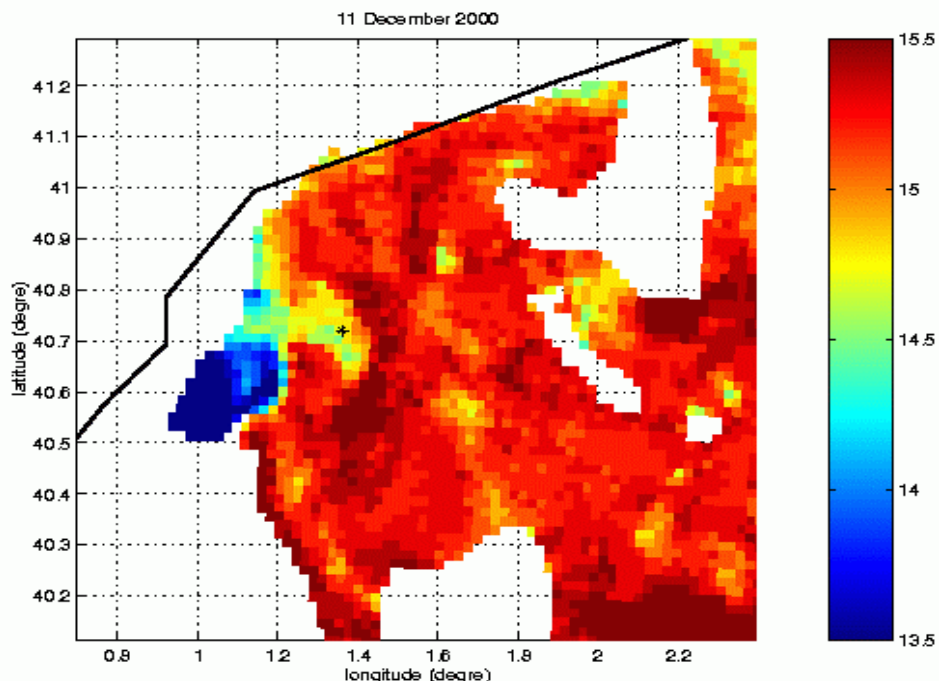


**Figure 3.2.** Sea surface temperature image of the platform region on December 11

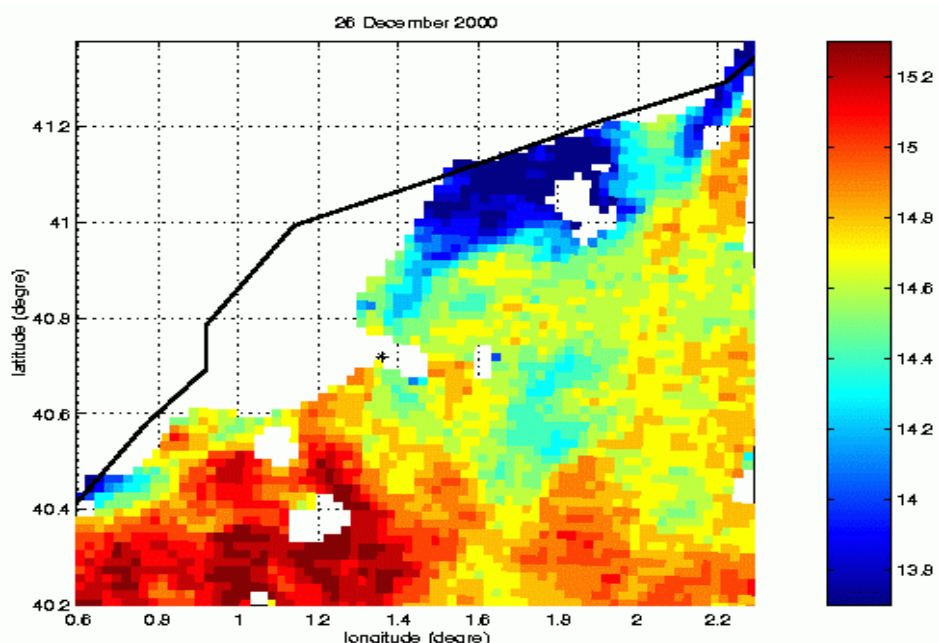


**Figure 3.3.** Sea surface temperature image of the platform region on December 26

The image of December 26 confirms the observation made on ocean color measurements of a plume of different water coming to the Casablanca platform.

### 3.3. Analysis of QUIKSCAT data

Measurements of the QUIKSCAT scatterometer (nudge algorithm) were co-located with the platform using a radius of 0.27° latitude and 0.37° longitude: 196 measurements were found for the duration of the campaign. Since the scatterometer cannot approach closer than 50 km from coast no measurement was coincident with the platform: all of them were east and south. These data were averaged for each satellite pass and the resulting average was compared with one-hour average of the in-situ measurements. The scatter plot of QUIKSCAT data versus the meteorological station measurements at 10 m height is shown below.

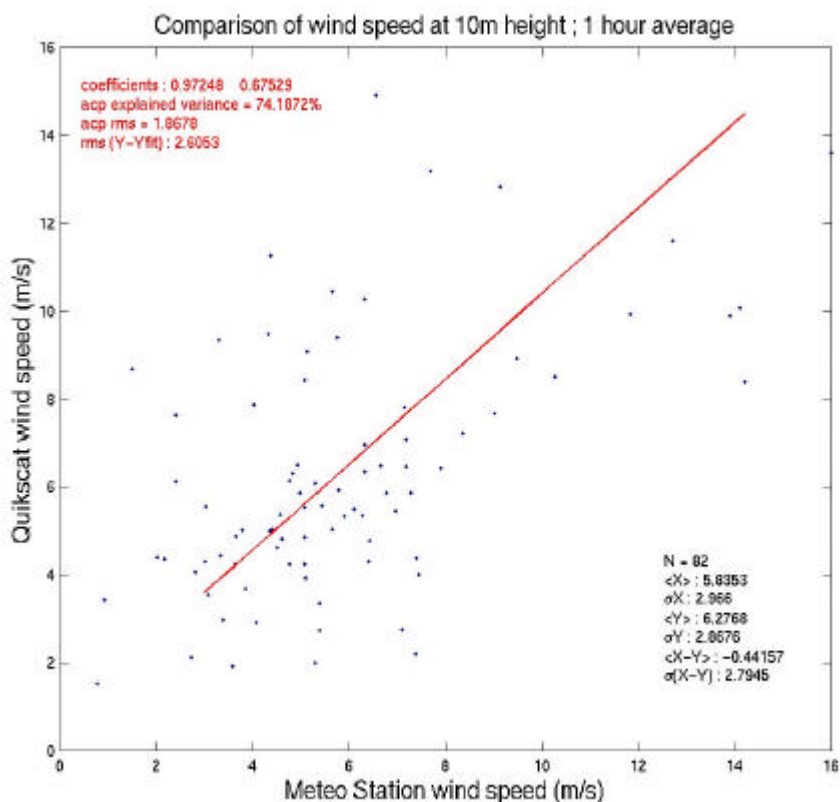


**Figure 3.4.** QUIKSCAT versus meteo station wind speed ( $U_{10}$ ) comparison.

The equation of the fit in the range 3-15 m/s is:  $U_Q = 0.97 U_M + 0.68$  with an explained variance of 74%; the mean difference between the instruments  $\langle U_M - U_Q \rangle$  is 0.44 m/s with a standard deviation of 2.8 m/s. The points are rather dispersed, probably due to the imperfect co-location, but they compare rather well.

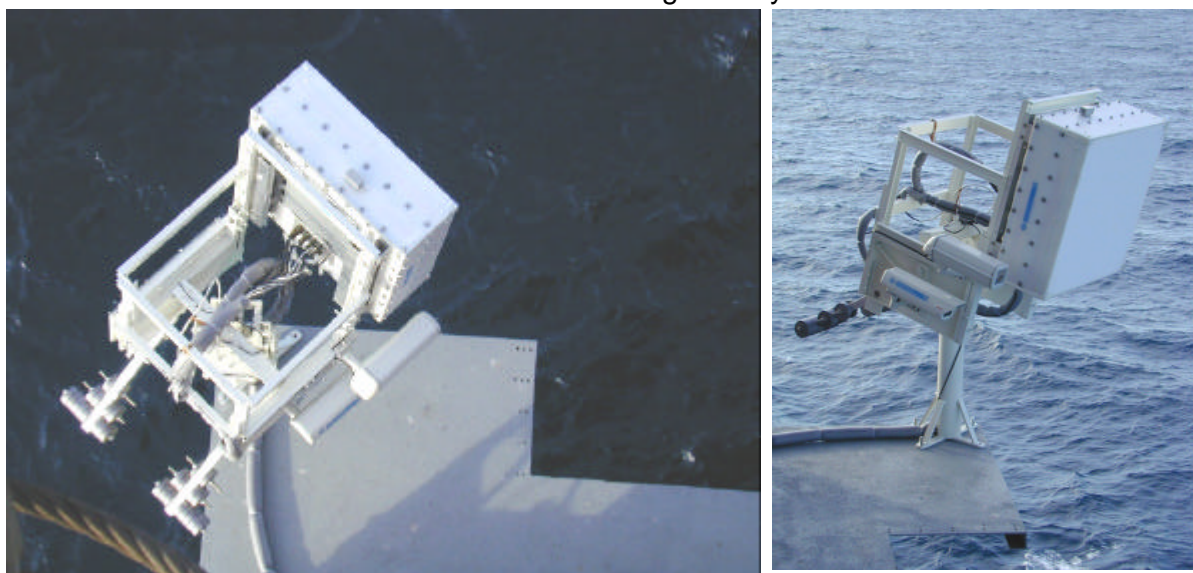
## 4. Analysis of radiometric data

### 4.1. L-band radiometric data (UPC)

The UPC L-band AUTomatic RAdiometer is a fully polarimetric radiometer that measures the horizontal and vertical brightness temperatures ( $T_h$  and  $T_v$ ) by means of two Dicke radiometers, and the third (U) and fourth (V) by means of a complex correlator.

The radiometer was mounted on a terrace specially designed and built for this experiment. The terrace was located in the North-West corner at 32 m above the sea level to have clear view of the zenith, and the widest possible angular excursion pointing in the up-wind direction (note that dominant winds come from the North and the North-West).

The measurements were restricted in elevation from 25° incidence angle (limited by the radiometers' terrace and the own platform) to 65° (limited by the pointing of the secondary lobe to the horizon). In azimuth the scan was limited to something more than 120°, from 110° West (limited by the radiometers' terrace at low incidence angles and by the safety ship at high incidence angles) to about 20° East (limited by the radiometers' terrace at low incidence angles). Figures 4.1a and 4.1b show a top and a side views of the radiometer to better understand the measurement geometry and the limitations.



a)

b)

**Figure 4.1.** a) Top and b) side views of the LAURA radiometer.

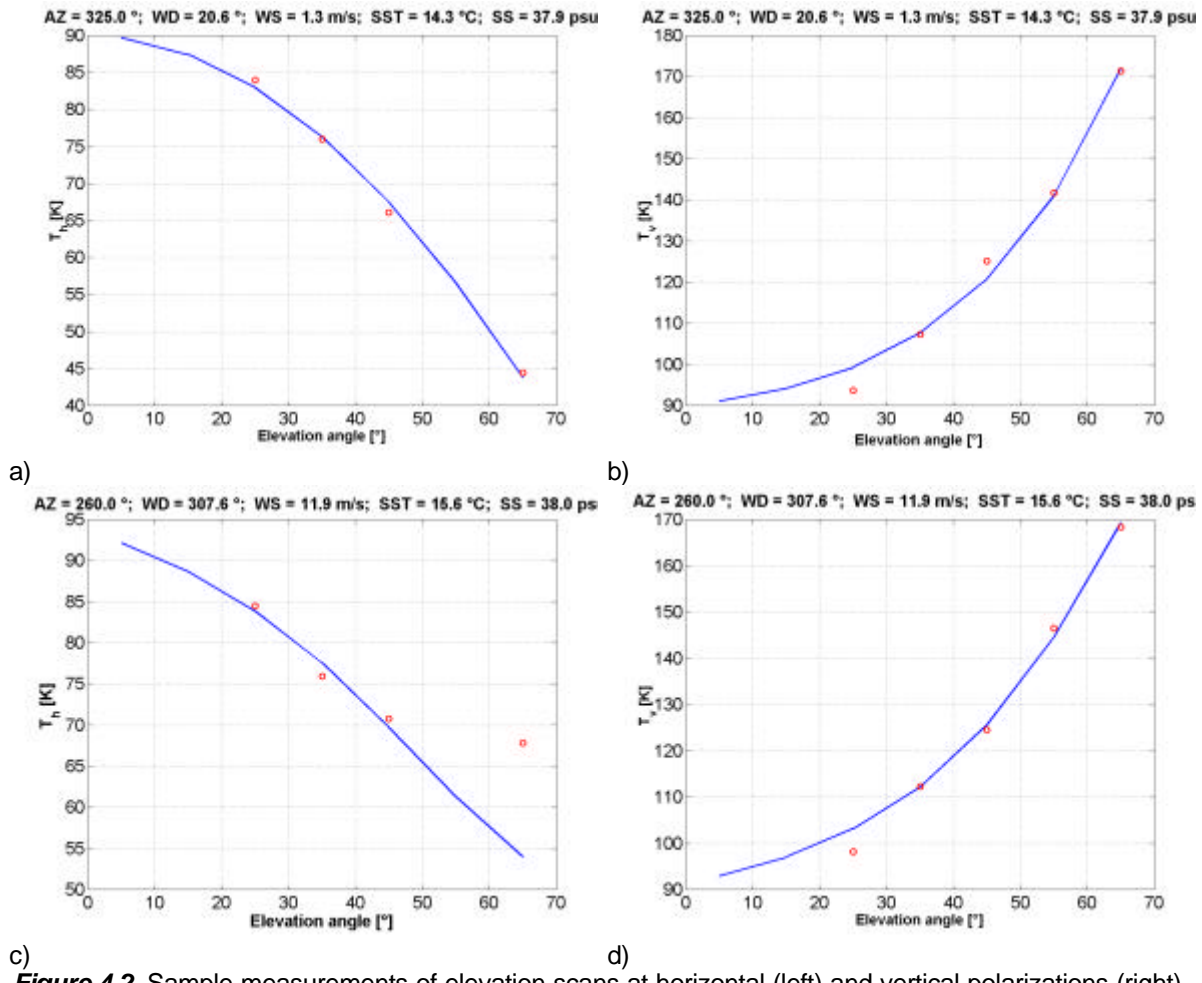
The calibration procedure (from output voltages to brightness temperatures, and from correlator counts to U and V) is described in detail the Data Acquisition Report. It includes corrections for:

- Atmospheric, cosmic and galactic noise contributions scattered on the sea surface computed and subtracted from antenna temperatures,
- Finite beamwidth effects, and
- Tilt oscillations (< 0.2° rms) due to high winds.

#### 4.1.1. L-band brightness temperatures: Signatures in elevation and azimuth

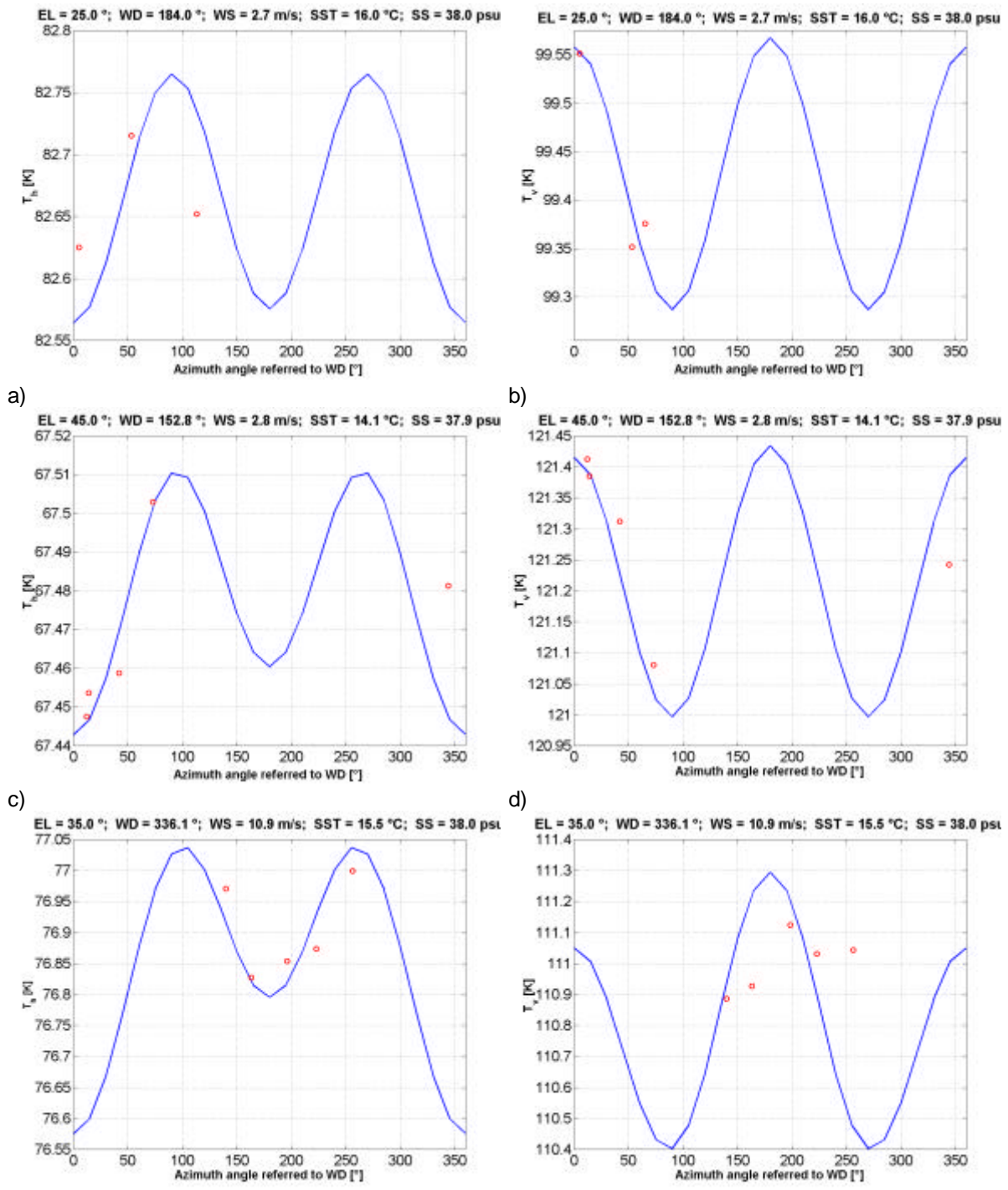
Three types of measurements were acquired: scans in elevation, scans in azimuth and fixed orientation to have coincident footprints with the stereo-camera.

Figure 4.2 presents typical measurements of elevation scans at horizontal (left) and vertical polarizations (right) for two different wind speeds: 1.3 m/s (a-b) and 11.9 m/s (c-d). The trends are almost always the correct ones with two exceptions: an increase at higher incidence angles ( $65^\circ$ , and sometimes  $55^\circ$ ) at horizontal polarization, and a decrease at low incidence angle ( $25^\circ$ ) at vertical polarization. The increase at horizontal polarization was clearly identified as radio frequency interference (RFI) coming from the coast of Tarragona, and was minimized/avoided by taking most of the measurements to the West. The decrease at vertical polarization is not well understood, but it may probably be due to the own metallic structure of the platform. The data points susceptible of being corrupted were eliminated in the analysis to determine the sensitivity to wind speed.



**Figure 4.2.** Sample measurements of elevation scans at horizontal (left) and vertical polarizations (right) for two different wind speeds: 1.3 m/s (a-b) and 11.9 m/s (c-d).

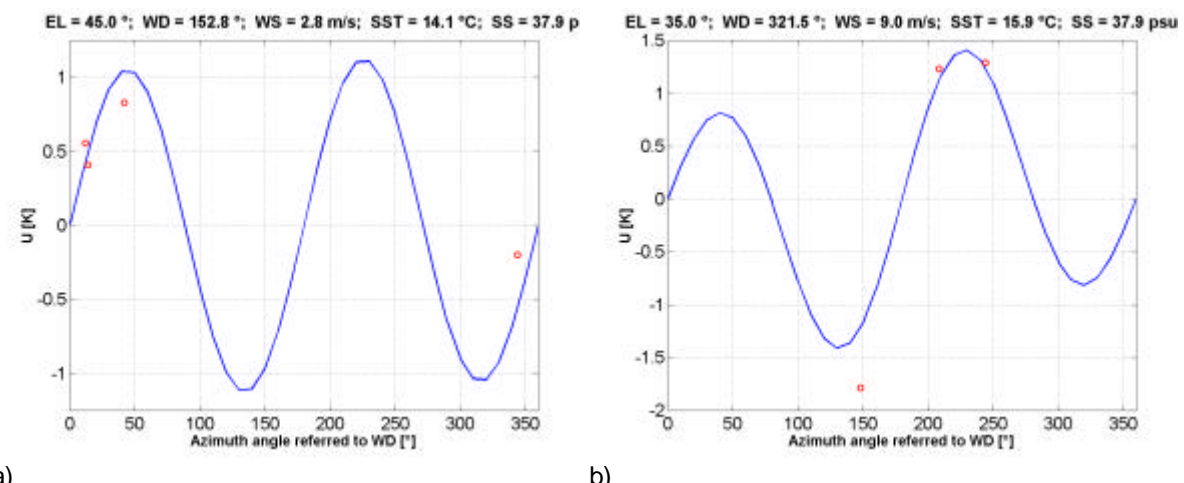
Figure 4.3 shows typical measurements of azimuth scans at horizontal (left) and vertical (right) polarizations for three different wind speeds and incidence angles: (a-b)  $\theta=25^\circ$ , WS = 2.7 m/s, (c-d)  $\theta=45^\circ$ , WS = 2.8 m/s, and (e-f)  $\theta = 35^\circ$ , WS = 10.9 m/s.



**Figure 4.3.** Sample measurements of azimuth scans at horizontal (left) and vertical (right) polarizations for three different wind speeds and incidence angles: (a-b)  $\theta=25^\circ$ , WS = 2.7 m/s, (c-d)  $\theta=45^\circ$ , WS = 2.8 m/s, and (e-f)  $\theta = 35^\circ$ , WS = 10.9 m/s.

It should be noted that in most scans there are missing points due to RFI, specially those pointing to the geographic North. Even though there are very few data points covering about one third of a full 360° scan, a small modulation 0.1-0.2 K is detected.

Figure 4.4 presents some sample measurements of azimuth scans for the third Stokes parameter (U) in different conditions: (a)  $\theta=45^\circ$ , WS = 2.8 m/s, and (b)  $\theta=35^\circ$ , WS = 9 m/s. The number of azimuth scans free of RFI is much smaller than for  $T_h$  or  $T_v$  alone, since it required that both channels were free of RFI. Since the magnitude of these variations is very small (typically < 0.5 K), it may be possible that some points contain residual RFI not perfectly removed (e.g. Figure 4.4b).



a) **Figure 4.4.** Sample measurements of azimuth scans for the third Stokes parameter (U): (a)  $\theta=45^\circ$ , WS = 2.8 m/s, and (b)  $\theta=35^\circ$ , WS = 9 m/s.

There are no plots available of measurements coincident with the stereo-camera, since it was pointing to the North, from the strongest RFI was coming.

#### **4.1.2. L-band brightness temperatures: Sensitivity to wind speed**

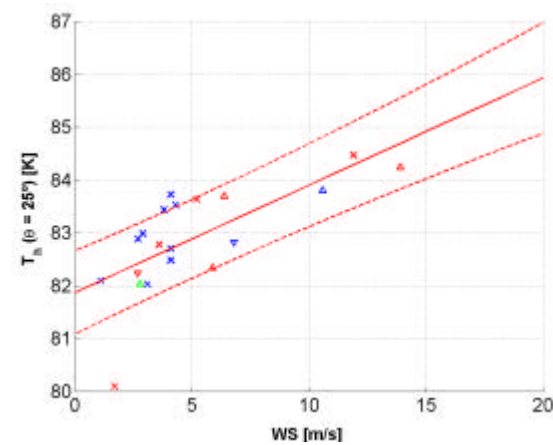
Since the effect of wind on the brightness temperatures may mask the signature due to salinity, the determination of the sensitivity of the brightness temperatures to wind speed is probably the main goal of the WISE-2000 campaign. In addition, these measurements are completely necessary to find out the best parametrization of the numerical model (section 5).

In order to determine it, all the data files have been read, and the data points sorted by polarization and incidence angle. Data points susceptible of wrong or corrupted by RFI have been filtered out. Figure 4.5 shows the sensitivity to wind speed of the L-band brightness temperature at horizontal (left) and vertical (right) polarizations at different incidence angles: (a-f)  $\theta=25^\circ$ , (b-g)  $\theta=35^\circ$ , (c-h)  $\theta=45^\circ$ , (d-i)  $\theta=55^\circ$  and (e-j)  $\theta=65^\circ$ . Table 4.1. lists the number of available data points for each plot. As it can be appreciated, the number is much smaller at horizontal polarization because of RFI, and decreases

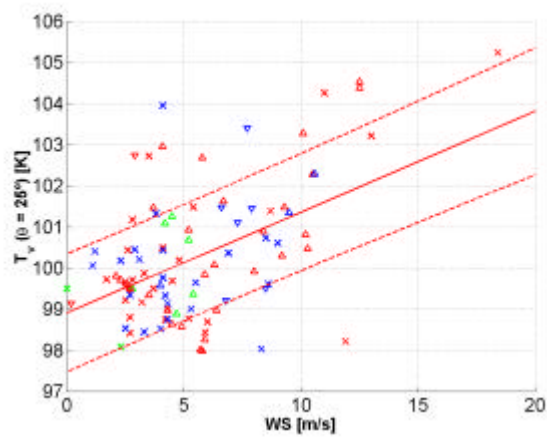
dramatically at higher incidence angles. This produces larger uncertainties (dotted lines in Figure 4.5) and in the estimation of the slope. Figure 4.6 presents the estimated slopes at horizontal (blue) and vertical (red) polarizations vs incidence angle and their associated error bars. It is found that the error bars are mostly due to the uncertainty in the wind speed estimation ( $\sigma_{WS}$  meteo station - WS buoy  $\sim 1.8$  m/s), a problem that will be solved in WISE-2001 by replacing the mechanical anemometer by an ultrasonic one, with an order-of-magnitude accuracy and resolution improvement.

**Table 4.1.** Number of data points for each plot in Figure 4.5.

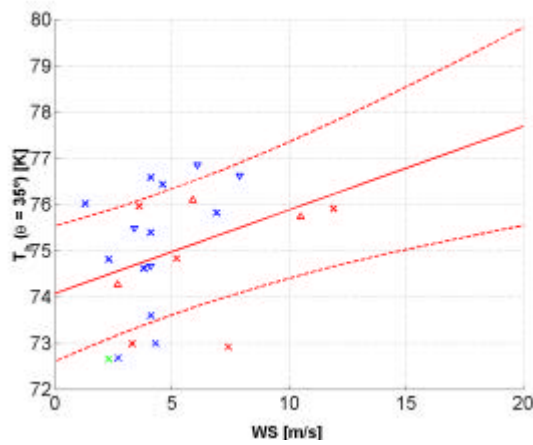
	$\theta = 25^\circ$	$\theta = 35^\circ$	$\theta = 45^\circ$	$\theta = 55^\circ$	$\theta = 65^\circ$
H-polarization	20	23	29	14	8
V-polarization	100	74	98	102	100



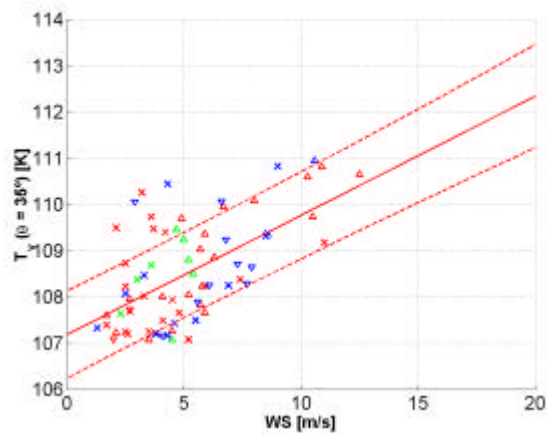
a)



f)



b)



g)

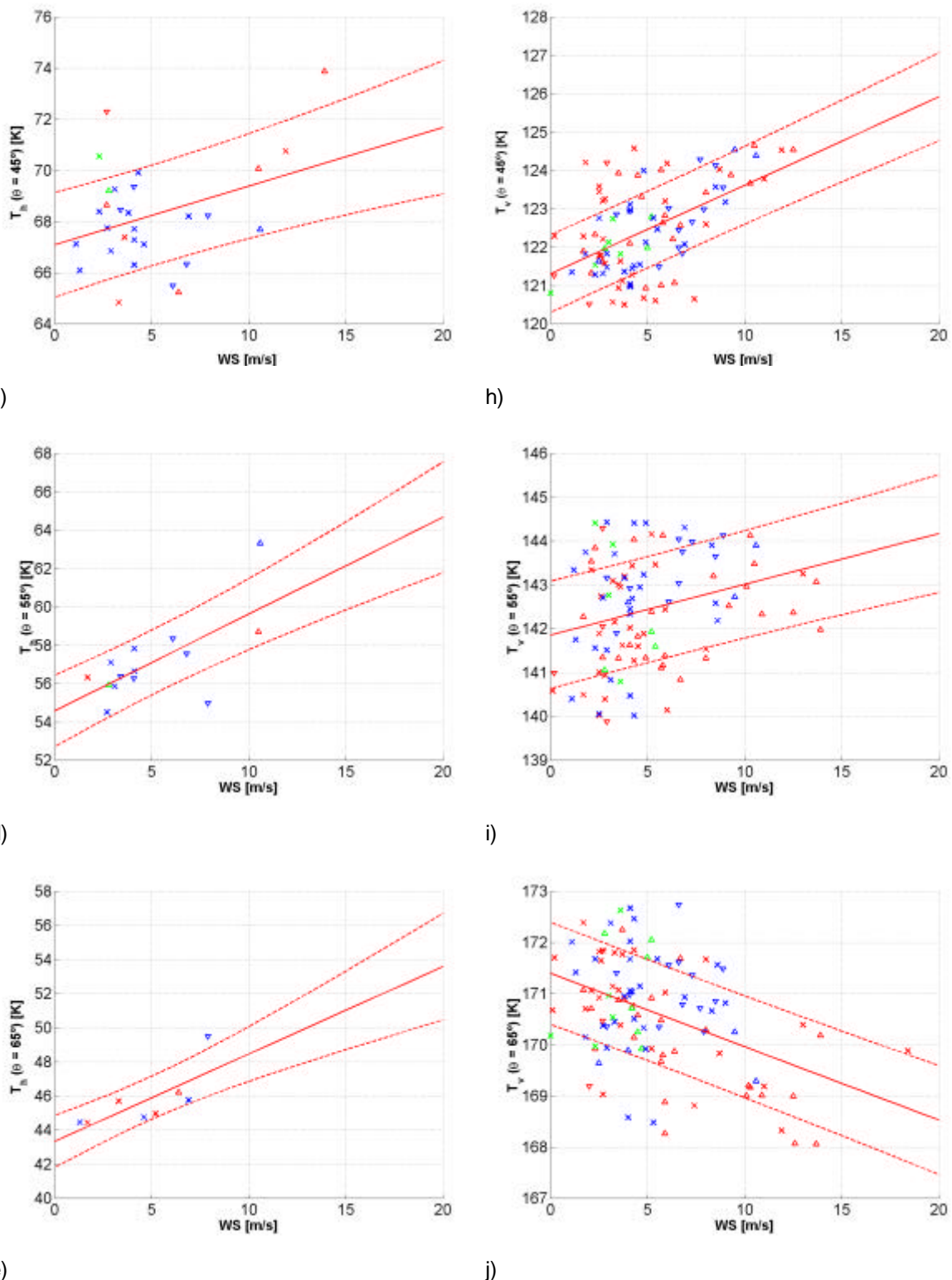


**Figure 4.5.** Sensitivity to wind speed of the L-band brightness temperature at horizontal (left) and vertical (right) polarizations at different incidence angles: (a-f)  $\theta=25^\circ$ , (b-g)  $\theta=35^\circ$ , (c-h)  $\theta=45^\circ$ , (d-i)  $\theta=55^\circ$  and (e-j) $\theta=65^\circ$ .

Legend: SST: Blue: < 14.5 °C, Green: 14.5 °C, 15.5 °C, Red: > 15.5 °C  
 Wind direction relative to radiometer:  $\blacktriangle$ : up-wind,  $\blacktriangledown$ : down-wind,  $\times$ : cross-wind

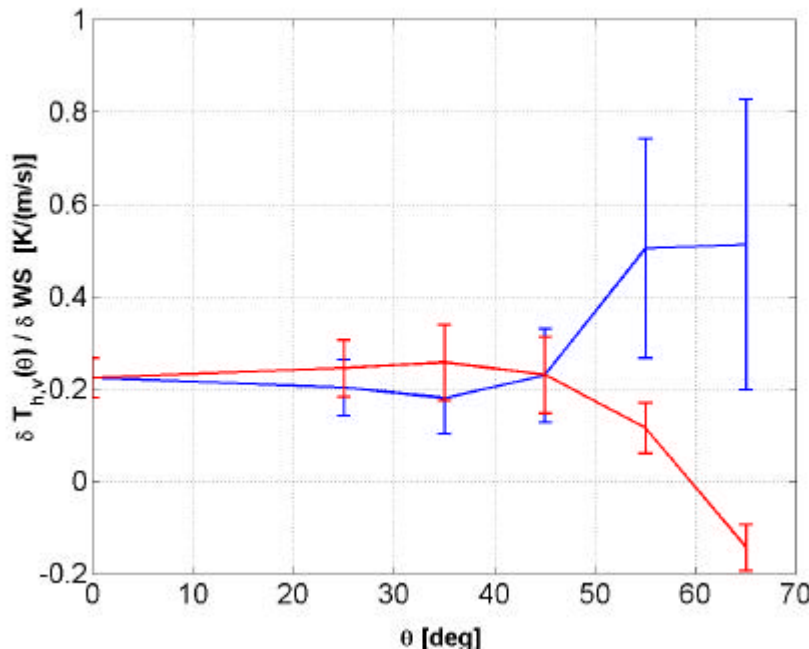


Figure 4.6. Sensitivity of  $T_h$  (blue) and  $T_v$  (red) to wind speed at 10 m height

As it will be discussed in section the results plotted in Figure 4.6 are in agreement with Hollinger's ones [1971], and the error bars are much smaller than the  $\pm 0.2$  K/(m/s). It is found that:

- At **nadir**, the extrapolated sensibility is estimated to be  $\sim 0.22$  K/(m/s).
- Around  $\theta \approx 60^\circ$ , **the brightness temperature at vertical polarization is insensitive to wind speed.**

The fact that, at low incidence angles, the sensitivity of  $T_v$  to wind speed is larger than that of  $T_h$ , although within the error bars) is surprising, since this behavior is not predicted by models, nor is present in Hollinger's measurements. The point now is to try find out in the WISE-2000 CCN-2 is this phenomenon may be due to the presence of swell (note in Figure 1.1 that dominant winds and currents do not have the same direction), and/or by wave reflections on the platform structure.

#### 4.2. Ka-band radiometric data (UMass)

The Microwave Remote Sensing Laboratory (MIRSL) of the University of Massachusetts has participated in WISE-2000 with an L-band radiometer that became unoperative in the first days, and a Ka-band radiometer which was operated by UMass personnel during the whole campaign. UMass participation was sponsored by the Office of Naval Research (ONR).

The UMass Ka-band polarimetric radiometer was located on the north side of the Casablanca platform and performed a total of 40 azimuthal scans at each incidence angle

of  $35^\circ$ ,  $45^\circ$ ,  $55^\circ$  and  $65^\circ$ . Radiometer gain and offset were found by extrapolating tipping curve to zero atmosphere (2.7 K) and using ambient microwave absorber.

#### 4.2.1. Ka-band brightness temperatures: Time series

Figure 4.7 presents a series of instantaneous brightness temperatures at  $\theta=65^\circ$  for vertical (left) and horizontal (right) polarizations and three different wind speeds: (a-d) 2 m/s, (b-e) 5 m/s, (c-f) 10 m/s. As it can be appreciated, both the vertical and the horizontal brightness temperatures have a mean value and present oscillations, which are related to the wave train and the local slope of the facet that is being pointed. The amplitude of these oscillations seems to increases with wind speed at horizontal polarization, but at 10 m/s seems to decrease at vertical polarization. The average value is then obtained by averaging the value of at least 10 oscillations.

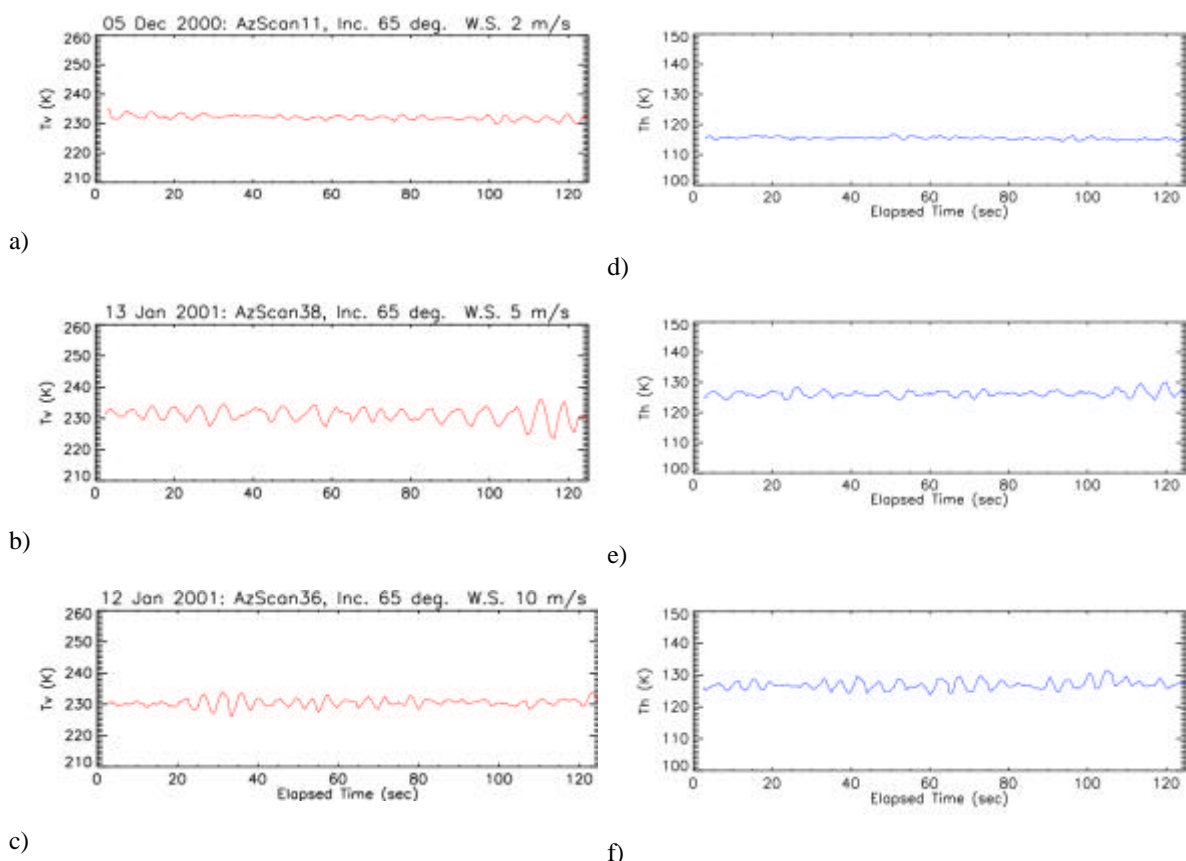


**Figure 4.7.** Series of instantaneous brightness temperatures at  $\theta=65^\circ$  for vertical (left) and horizontal (right) polarizations and three different wind speeds: (a-d) 2 m/s, (b-e) 5 m/s, (c-f) 10 m/s.

#### 4.2.2. Ka-band brightness temperatures: Signature in elevation

A data point at a given azimuth angle is obtained by averaging each time series. These values are then azimuthally-averaged to derive the vertical brightness temperatures. Figure 4.8 presents the azimuthally-averaged vertical brightness

temperatures vs. incidence angle for different wind speeds: a) WS = 2 m/s, b) WS = 5 m/s, c) WS = 8 m/s, and d) WS = 10 m/s. agree well with simulation results computed with the G. O. model described in *Camps and Reising [2001]*.

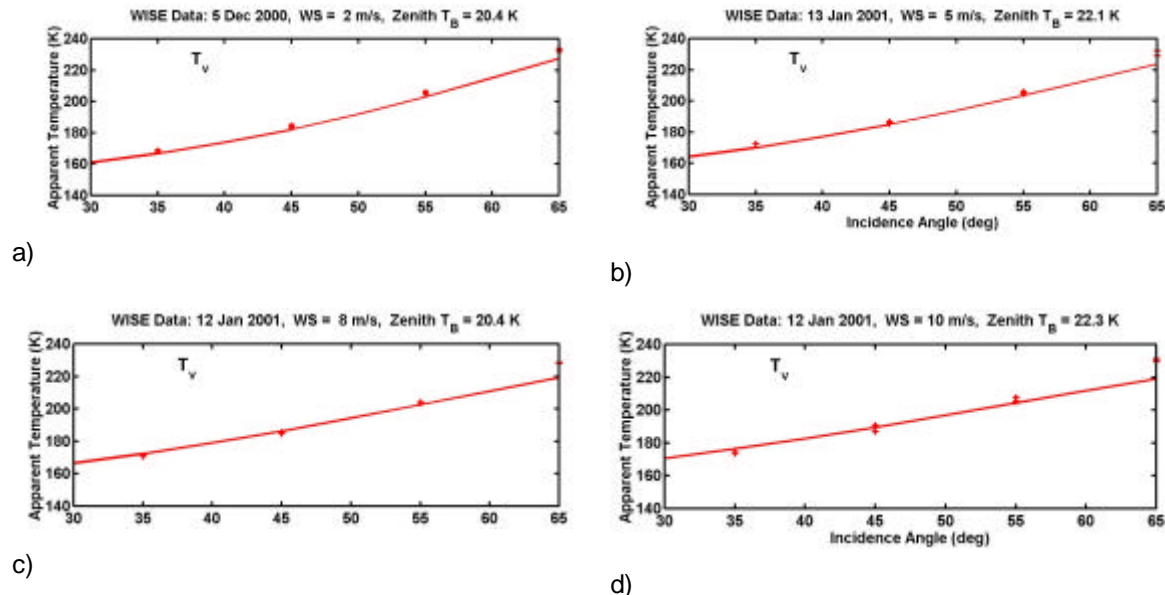


**Figure 4.8.** Azimuthally-averaged vertical brightness temperatures vs. incidence angle for different wind speeds: a) WS = 2 m/s, b) WS = 5 m/s, c) WS = 8 m/s, and d) WS = 10 m/s.

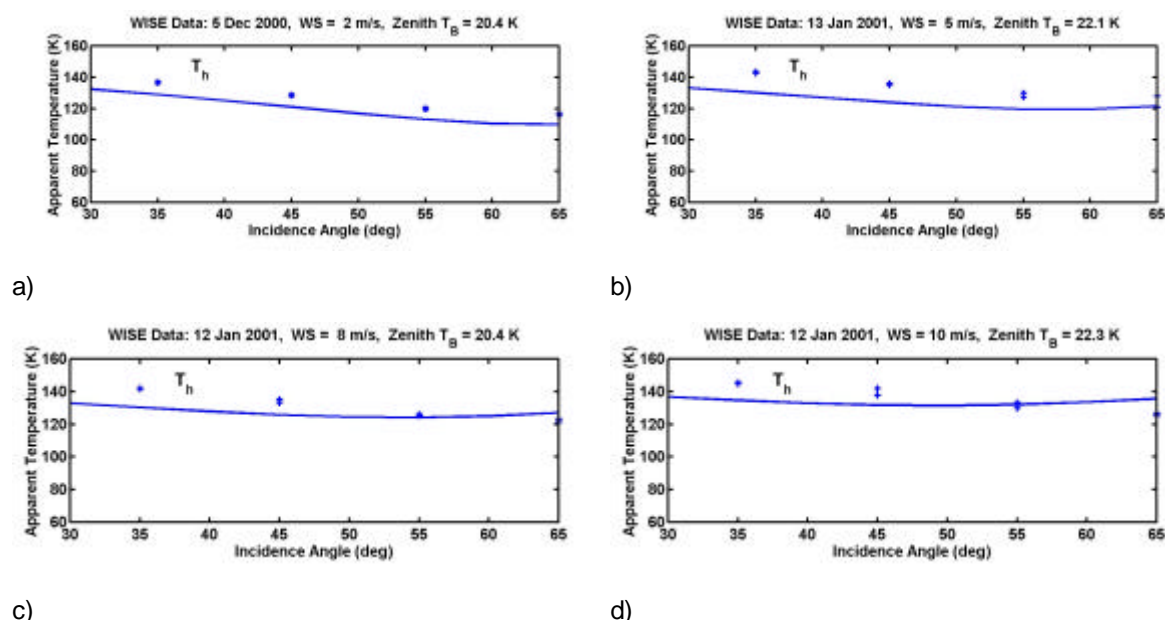


**Figure 4.9.** Azimuthally-averaged horizontal brightness temperatures vs. incidence angle for different wind speeds: a) WS = 2 m/s, b) WS = 5 m/s, c) WS = 8 m/s, and d) WS = 10 m/s.

Figure 4.9 presents the azimuthally-averaged horizontal brightness temperatures for the same conditions. They show similar trends to simulation results, however, most measurements exhibit a positive bias, and the slope effect of increasing wind speed is over-predicted by the G.O. model described in *Camps and Reising* [2001]. Further investigation is required to determine if this effect is due to the wave reflection (and wave stabilization) on the North side, as discussed in section 2.4.2.

## **5. Emissivity modeling studies, comparison with WISE and reported measurements**

### **5.1. Introduction**

The results of section 4.1 should in principle be now compared with the results of emission models so as to refine or even validate them. However, to do so, one must first take into account a number of considerations:

- **Model for sea foam coverage:** Even though WISE results on foam coverage are in agreement with those reported in the literature, it should be noted that it depends on many other factors, such as the fetch duration, the atmospheric stability, the salinity etc., not just only on WS [Monahan and O'Muircheartaigh, 1986; Monahan and Lu, 1990]
- Additionally, there is a **large variability in the sea foam coverage** for the “same” wind conditions (section 2.4.2)
- The **emissivity of the sea foam at L-band is not known**. To authors’ knowledge, even though these measurements have been performed at higher frequencies, nobody has never performed such measurements at L-band.
- There are **two main models for the dielectric permittivity of the sea water**: Klein and Swift [1977] and the more recent one derived by Ellison et al. [1996]. The first one was derived in the low microwave frequency range from NaCl solutions, which are known to have a conductivity 3% higher than the equivalent sea salt solutions. The second one has derived from sea water samples and measurement taken in the range 6-89 GHz, and therefore has to be extrapolated at L-band.

Without entering in a discussion of which one is better, we just note that the predicted brightness temperature using Ellison model is always higher than that using the Klein and Swift model. This difference is about 0.9 K at nadir and increases at vertical polarization with increasing incidence angles, while decreases at horizontal polarization (Figure 5.1). In the sea salinity retrieval problem, if the algorithm is designed to work on  $I = T_v + T_h$  measurements, this effect tends to compensate and it appears as a bias.

Additionally, this **difference** not only **depends on incidence angle**, but also on the **SSS** and **SST** (Figure 5.2). Around 15°C, the variation with salinity is almost

negligible, but this difference increases noticeably at low temperatures, precisely where the brightness temperature sensibility is lower.

Finally, it must be pointed out that these models were derived from measurements acquired with certain uncertainties. These uncertainties in the dielectric constant determination translate into an error in the brightness temperature of almost 1 K in both cases (Figure 5.3). Note that in Figure 5.3 the error bars do not even overlap.

Therefore, it is very important to derive more accurate expressions for the dependence of the dielectric constant with SSS and SST at 1.4 GHz.

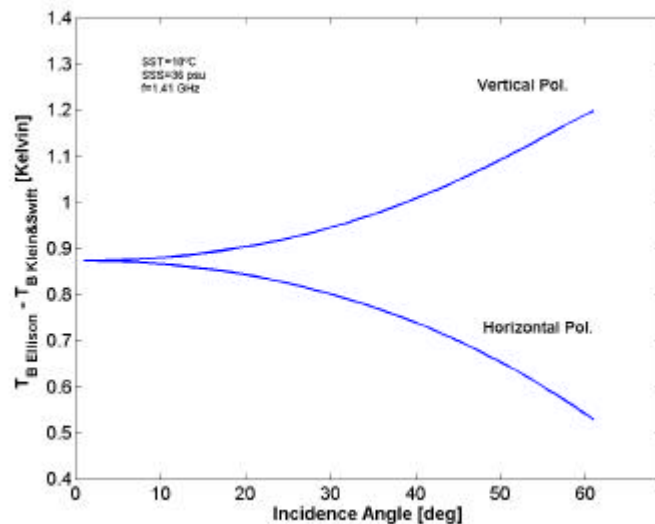


**Figure 5.1.** Incidence angle dependence of the difference between brightness temperatures computed using Ellison or Klein&Swift sea water permittivity model (SST = 18°C, SSS = 36°C, f = 1.41 GHz).

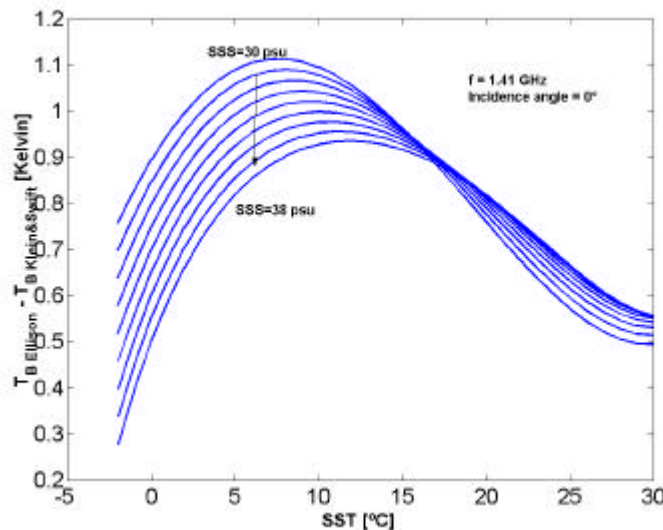


**Figure 5.2.** SST dependence of the difference between brightness temperatures computed using Ellison or Klein&Swift sea water permittivity model ( $\theta=0^\circ$ , f = 1.41 GHz).

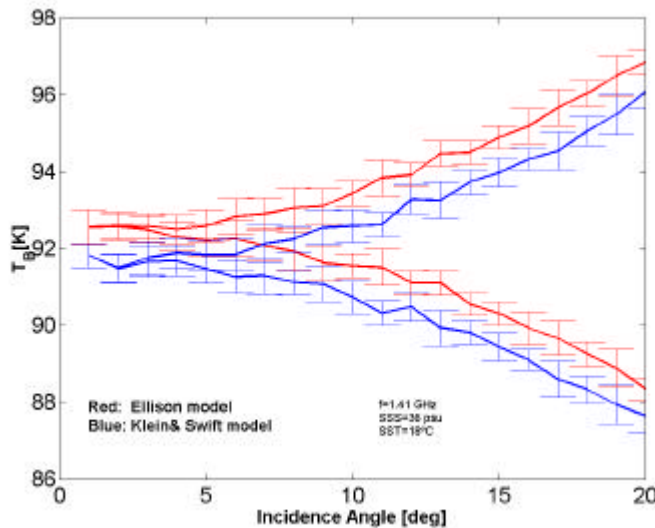


**Figure 5.3.** Brightness temperature uncertainties associated to the measurement uncertainty in the dielectric permittivity of the sea water: Ellison (red) and Klein-Swift (blue) models (mean and standard deviation computed from 100 simulations).

- **Model for sea surface** (different parametrizations or spectra). Most of these spectra have tuning parameters adjusted to match backscattering measurements. Newer spectra have found to present some problems when applied to the emissivity modelling problem (sections 5.2 and 6). In most cases their range of validity must be established, and in practice, nobody guarantees that what we are going to find in the ocean corresponds to one or another spectrum.
- There are a number of **numerical models** to compute the backscattering and the emissivity. Some of them even have tuning parameters. Each one has its own range of validity, but it is found that even when they are valid in a given conditions, the predicted results are different.

The foam coverage and its variability have been already been discussed previously (sections 2.4.2 and 2.4.3). The emissivity of sea foam at L-band is not known, and there are disagreements in best sea water dielectric permittivity model (at L-band). In the next sections we are going to analyze the effects of different numerical methods, their range of validity, and different sea surface parametrizations.

## 5.2. Kirchhoff model

The Kirchhoff model considers the surface flat enough for approximating it by planes, called facets. The validity range is restricted in the horizontal dimension by the correlation length “ $l$ ”, which must be bigger than the wavelength of the incident field. In the vertical dimension, the range is limited by the height variance  $\sigma_h^2$  which must be small compared to the wavelength. Then the two conditions to be accomplished are:

$$k \cdot l > 6 \quad (5.1a)$$

$$r_c > I \quad (5.1b)$$

where  $k$  is the wave number and  $r_c$  is the curvature radius of the surface. For a Gaussian surface the curvature radius is computed by the following expression:

$$r_c = \frac{l^2}{2s} \sqrt{\frac{p}{6}} \quad (5.2)$$

Considering this last expression equations (5.1) derive to:

$$l^2 > 2.76 s_h \cdot I \quad (5.3a)$$

$$k \cdot l > 4.17 \sqrt{k \cdot s_h} \quad (5.3b)$$

On the other hand, Kirchhoff cannot be used when the surface is completely flat or with a very small roughness, which implies that the surface roughness must have a minimum standard deviation height:

$$k s_h > 0.3 \quad (5.4)$$

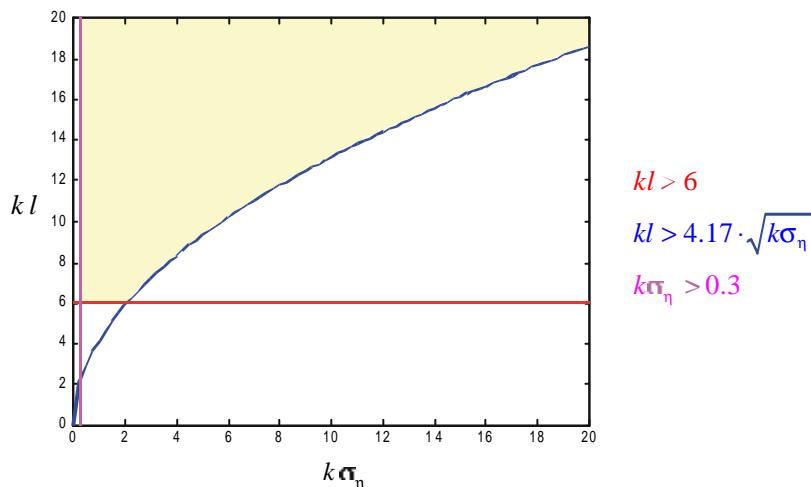


**Figure 5.4.** The yellow zone in the plot marks the validity range of the Kirchhoff model.

This range of validity has been particularized at L-band (WISE conditions):

$$f = 1.4 \text{ GHz} \Rightarrow I = 21.4 \text{ cm} \Rightarrow k = 29.32 \text{ rad m}^{-1},$$

where the Elfouhaily spectrum has been used in the particularization:

$$l = \sqrt{2} \cdot \frac{s_h}{s_s}, \text{ where } s_s \text{ is the surface rms slope.}$$

The roughness state of the sea surface depends on the wind speed. From the statistic restrictions the limits of the wind speed<sup>1</sup> at 12.5 m from the sea surface have been computed:

$$k \cdot l > 6 \Rightarrow \frac{\mathbf{s}_h}{\mathbf{s}_s} > 0.145 \Rightarrow V|_{h=12.5} > 2.035 \frac{m}{s} \quad (5.5)$$

$$k \cdot l > 4.17 \cdot \sqrt{k \cdot \mathbf{s}_h} \Rightarrow \frac{\mathbf{s}_h}{\mathbf{s}_s^2} > 0.296 \Rightarrow V|_{h=12.5} > 1.065 \frac{m}{s} \quad (5.6)$$

$$k \cdot \mathbf{s}_h > 0.3 \Rightarrow \mathbf{s}_h > 0.01023 \Rightarrow V|_{h=12.5} > 1.34 \frac{m}{s} \quad (5.7)$$

The most sever restriction is the one established in equation (5.5). Figure 5.5 the wind speed validity region for Kirchhoff model at 1.4GHz.

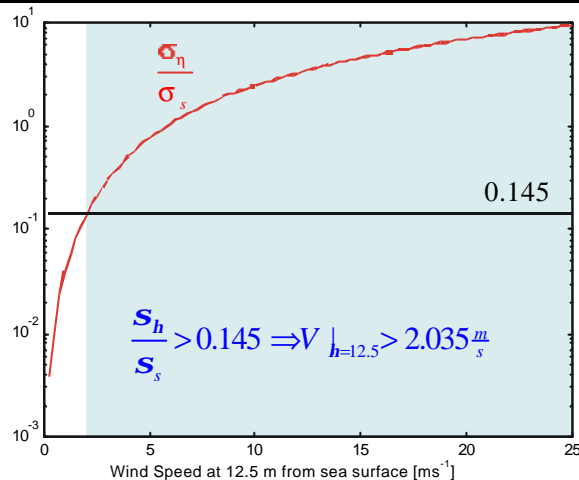


**Figure 5.5.** Wind Speed range in which Kirchhoff hypothesis are valid at 1.4GHz (blue zone).

In fact, other approximations are imposed when using Kirchhoff model. These approaches reduce its validity range. The use of the *Stationary-Phase approximation* (SP) means that the scattering can occur only along directions for which there are specular points on the surface. Hence local diffraction effects are excluded. In this case, it is assumed that the surface standard deviation is large, which represents purely non-coherent scattering. Consequently, a new restriction appears:

$$k\mathbf{s}_h > 2.0 \Rightarrow \mathbf{s}_h > 0.0682 \Rightarrow V|_{h=12.5} > 3.425 \frac{m}{s} \quad (5.8)$$

<sup>1</sup> In this section we define the validity margins using the wind speed at 12.5 m height, since it is the one used by Cox and Munk [1954]. Its value is just slightly higher than that at 10 m height and can be computed assuming atmospheric stability.

Figures 5.6a shows the validity margin of Stationary Phase Approximation (SPA) with respect to the statistical information of the surface. Meanwhile, Figure 5.6b shows wind speed validity range for SP particularized to 1.4 GHz.

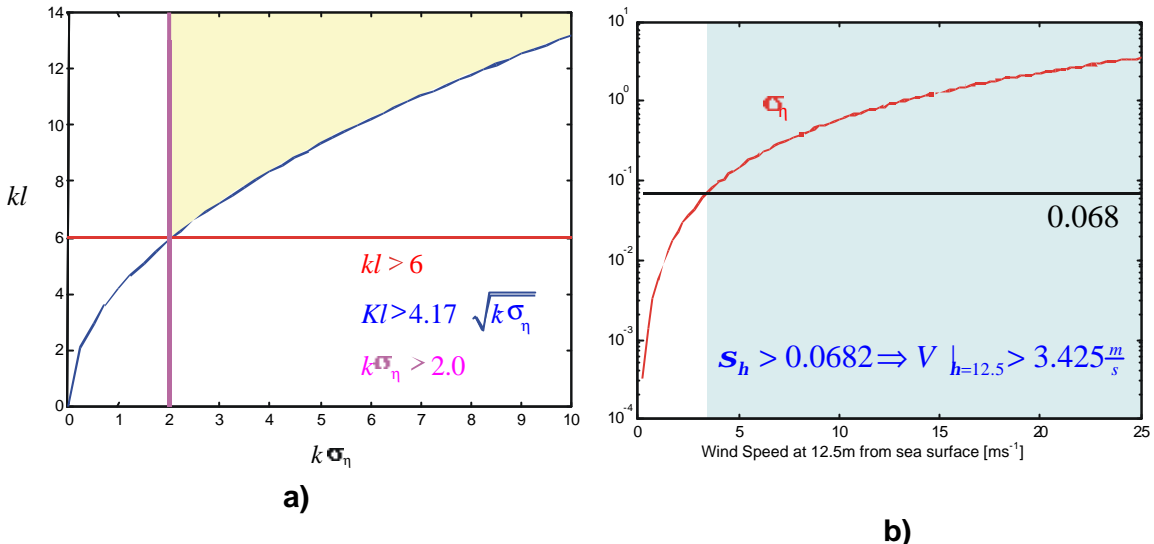


**Figure 5.6.** a) Validity margin (yellow zone) of Stationary-Phase Approximation. b) Validity range of the wind speed at 12.5m from the sea surface at 1.4GHz (blue zone).

When the surface standard deviation slope is less than 0.25 the SPA cannot be applied because the surface generates both non-coherent and coherent scattering. Then the scalar approximation is used on the Kirchhoff model, which is only valid for surfaces with small rms slopes. That is, they must obey the following inequalities (see figure 5.8a):

$$k\mathbf{s}_h < 2.0 \quad (5.9)$$

$$\mathbf{s}_s < 0.25 \quad (5.10)$$

As on the other cases these inequalities can be written using the correlation length and the surface rms height:

$$kl > \frac{\sqrt{2}}{0.25} k\mathbf{s}_h \Rightarrow \mathbf{s}_h < 0.0682 \Rightarrow V |_{h=12.5} < 3.425 \frac{m}{s} \quad (5.11a)$$

$$\mathbf{s}_s < 0.25 \Rightarrow V |_{h=12.5} < 11.5 \frac{m}{s} \quad (5.11b)$$

Since inequality (5.11a) is more restrictive than (5.11b) it has been selected to be plotted at Figure 5.7b. Plots a) and b) in that figure demonstrates that the validity margin for scalar approximation on Kirchhoff model complements the one of SPA.

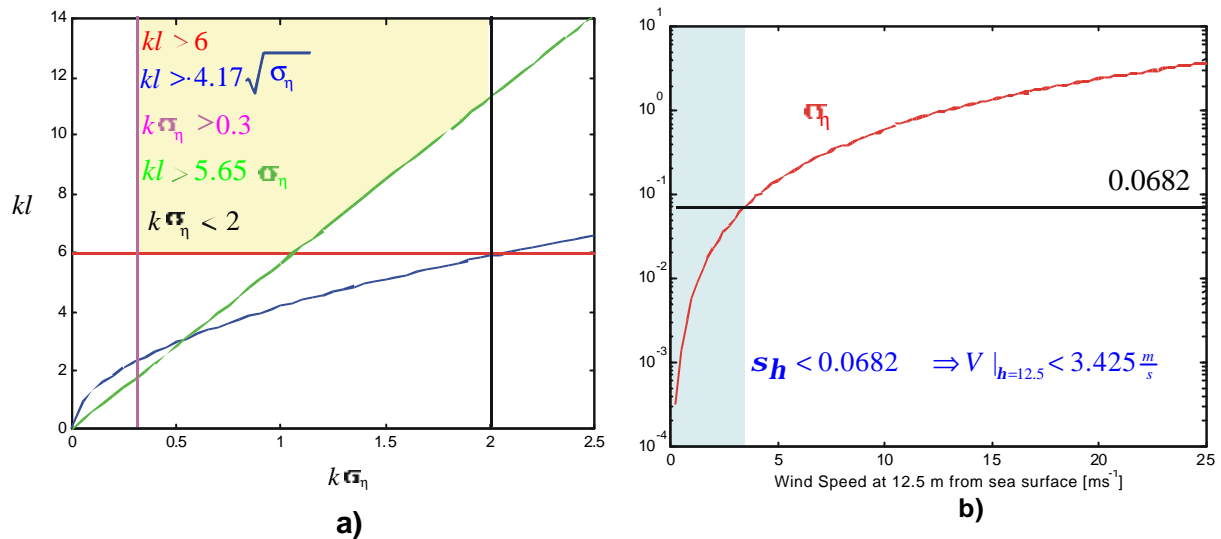


**Figure 5.7** a) Validity margin (yellow zone) of scalar approximation. b) Validity range of the wind speed at 12.5m from the sea surface at 1.4GHz (blue zone).

Finally, plots in Figure 5.8 present the dependence of the wind speed validity margin at a height of 12.5m from the sea surface to the frequency for the Stationary-Phase approach 5.9a and for the scalar approximation (5.8b). The yellow zone (wind speeds inside the hypothesis of the method) is much bigger for the SP than for the scalar approach. Furthermore, we can conclude that the scalar approach complements the margin of SP. Nevertheless, neither of those approaches obtains accurate results for very low wind speeds.

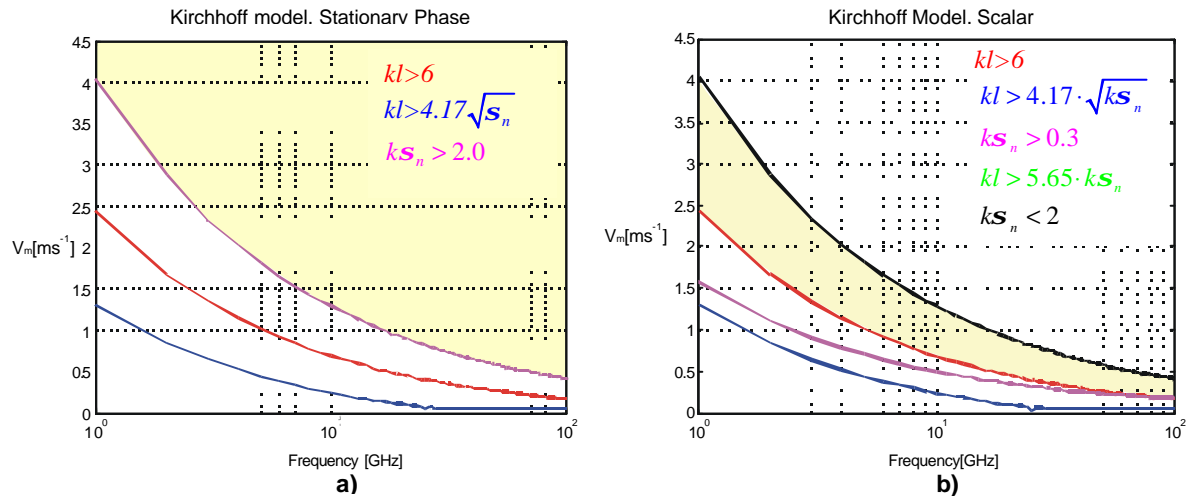


**Figure 5.8.** Validity margin of the wind speed at 12.5 m height from the sea surface respect to the frequency for a) Stationary-Phase Approximation and b) Scalar Approximation.

Figure 5.9 shows the amplitude of the zeroth (average value), first and second harmonics of the brightness horizontal (left) and vertical (right) brightness temperatures as a function of wind speed and incidence angle. At nadir, in the range 5 – 20 m/s, the

sensitivity to wind speed of  $T_{h0}$  and  $T_{v0}$  is 0.2 K/(m/s), in agreement with other models and measurements. At horizontal polarization the sensitivity to wind speed reaches 0.5 K/(m/s) at high incidence angles, while at vertical polarization it decreases sharply for incidence angles greater than 50°, and eventually, it becomes negative beyond  $\theta>60^\circ$ , a behaviour that does not fully agree with measurements. The slight decrease at medium range incidence angles at horizontal polarization and increase at vertical polarization is one of the draw-backs of this model. Except at large incidence angles and high winds, the azimuthal variation is dominated polarization by a second harmonic behavior.

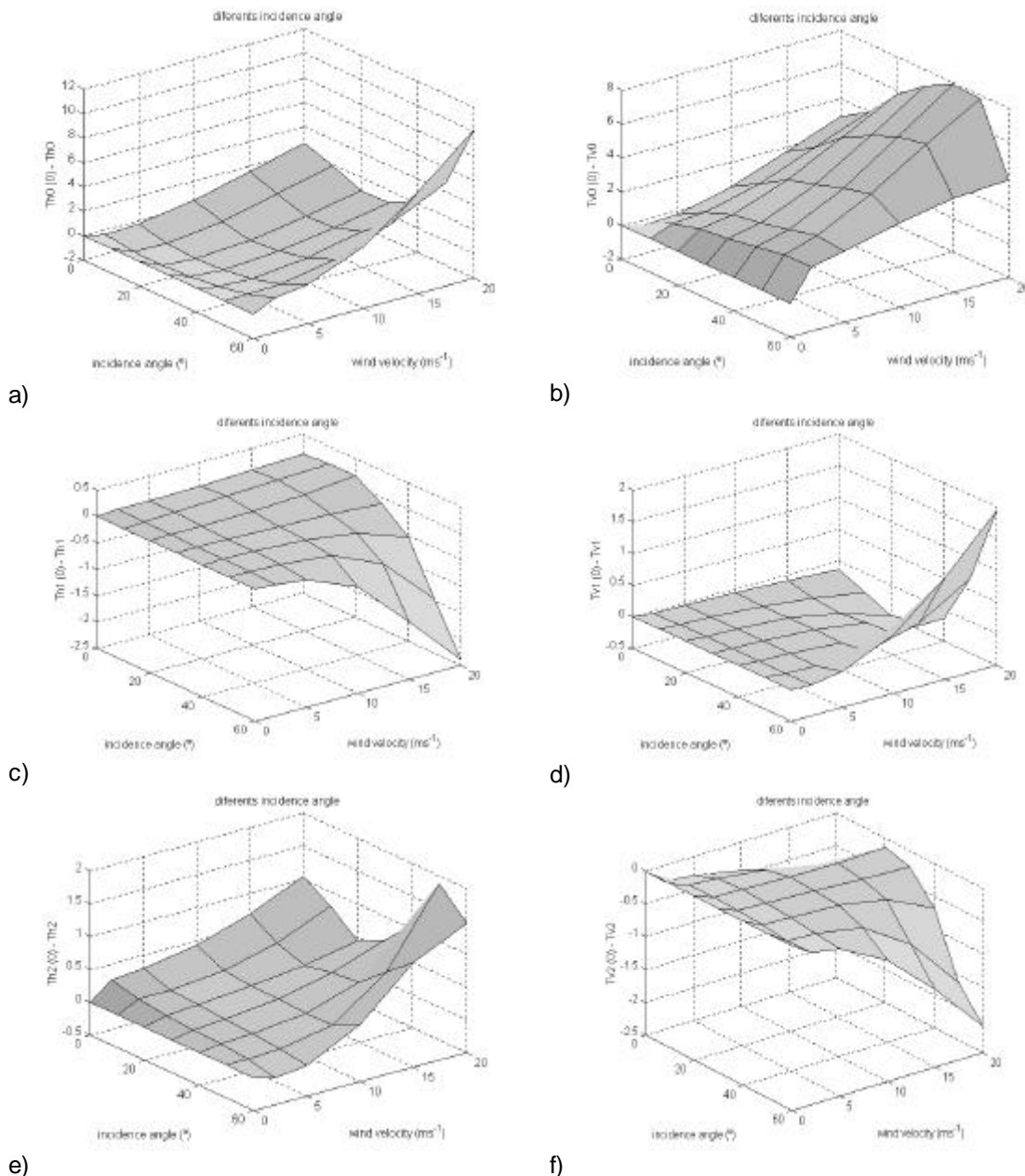


**Figure 5.9.** Simulation results using the Kirchhoff model under the SPA showing the amplitude of the (a-b) zeroth, (c-d) first and (e-f) second harmonics of the horizontal (left) and vertical (right) brightness temperatures ( $T_{h,v}(\phi)=T_{h,v0}+T_{h,v1}\cos(\phi)+T_{h,v2}\cos(2\phi)$ )

### 5.3. Small Perturbation Model (SPM)

The Small Perturbation Method has a very small validity range when sea surface emissivity is studied. As it is demonstrated below, only very low wind velocities can be considered.

The Small Perturbation Method is used when both the rms height and the correlation length are smaller than the wavelength. The validity range is determined with the following inequalities:

$$k\mathbf{s}_h < 0.3 \Rightarrow \mathbf{s}_s = k\mathbf{s}_h \Rightarrow \mathbf{s}_s < 0.3 \quad (5.12a)$$

$$kl > 4.71k \cdot \mathbf{s}_h \quad (5.12b)$$

These inequalities are plotted at Figure 5.10. The validity margin for this method is quite small (yellow zone). As in Kirchhoff method, these conditions have been particularized at 1.4 GHz and then the statistical conditions of the roughness for the sea surface have been transformed into the physical main contribution for that roughness (the wind speed). Figure 5.11a shows the wind speed (at 12.5 m from the sea surface) validity margin at 1.4 GHz of the SPM and figure 5.11b presents de dependence of that range in front of the frequency in GHz. Both plots demonstrate that this method can only be used for predicting the emissivity of the sea surface when the wind speed is really low. At 1.4 GHz the maximum permitted value of the wind speed is about 0.2 m/s.

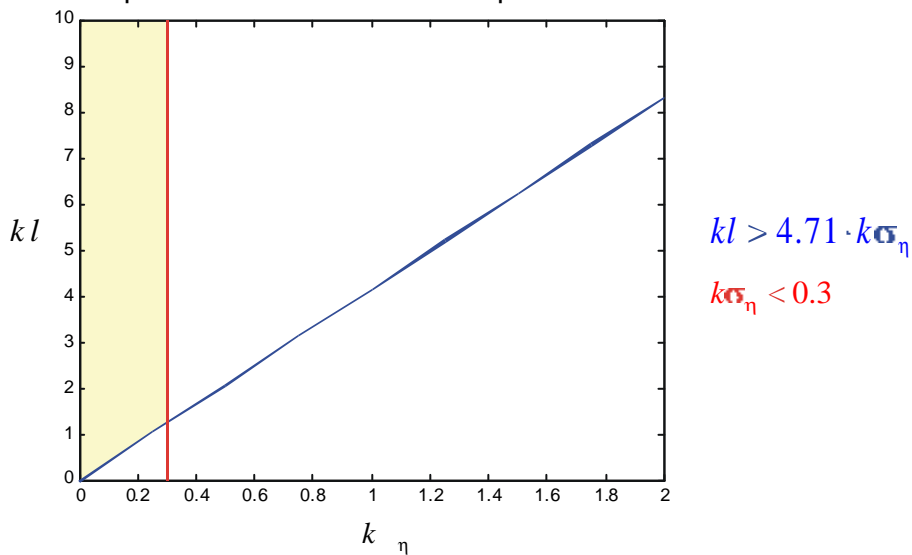


**Figure 5.10.** The yellow zone represents the combination of correlation length and rms height values in which SPM model obtain accurate results.

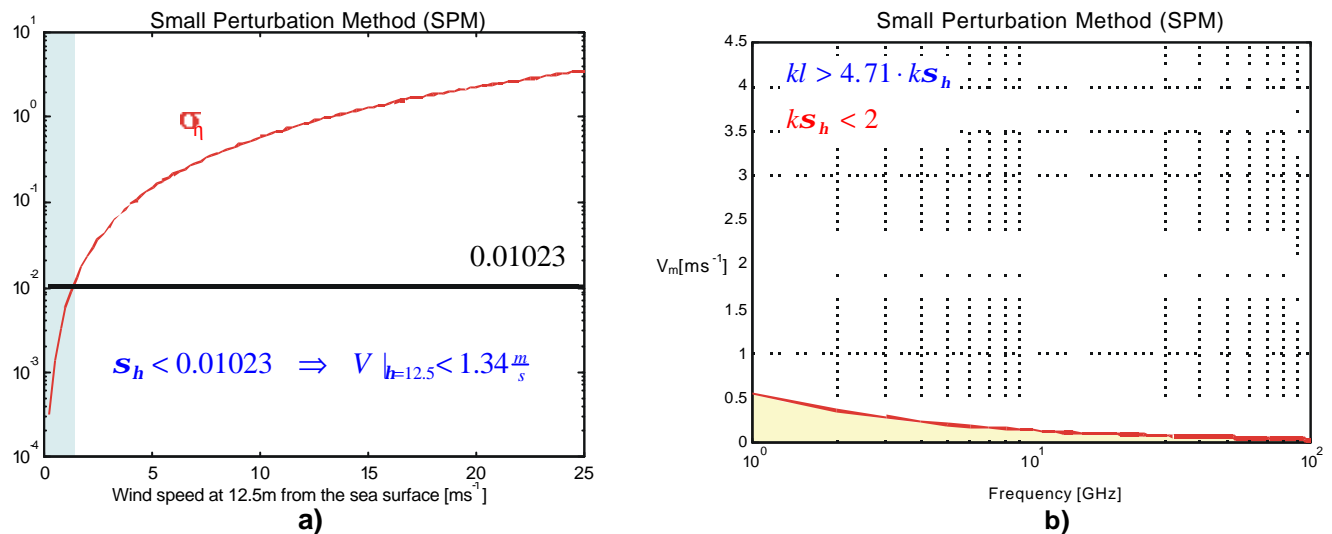


**Figure 5.11.** a) The most restrictive condition for the height standard deviation when SPM is applied. The maximum wind speed at 12.5 m from the sea surface is 1.34 m/s at 1.4 GHz. b) Maximum wind velocity allowed respect to the frequency for obtaining accurate results with SPM.

#### 5.4. Integral Equation Method (IEM)

The Integral Equation Method pretends to solve the scattering problem (then, the emissivity is computed by integration of the bistatic coefficients) with a broader range of applicability. It is based in the approximated resolution of the two integrals that define the fields on the scattering surface. This method was developed to cover the range of validity in which neither the SPM, nor the Kirchhoff Stationary Phase Approximation obtained accurate results. Under certain circumstances, it reduces to SPM and to Kirchhoff-SPA. Two different approximations for the Integral Equation Method exist. One is useful for surfaces with small scale of roughness and the other for large scale.

The most important approximation of the IEM is to use the global incidence angle instead of the local incidence angle when the Fresnel coefficients are computed. The accuracy of this approximation depends on the statistical parameters of the surface roughness, the self-correlation function and the dielectric constant. For surfaces with Gaussian self-correlation function the validity range is established with the following inequality:

$$kl < \frac{1.2\sqrt{\epsilon_r}}{ks_h} \quad (5.13)$$

Equation 5.13 demonstrates the dependence of the validity range with the dielectric constant. Consequently, when suitability is studied for sea surfaces it is necessary to consider a real situation of the salinity and temperature of the sea surface. Figure 5.12 plots condition of equation 5.13 for a sea with 38 psu of salinity and 15°C.

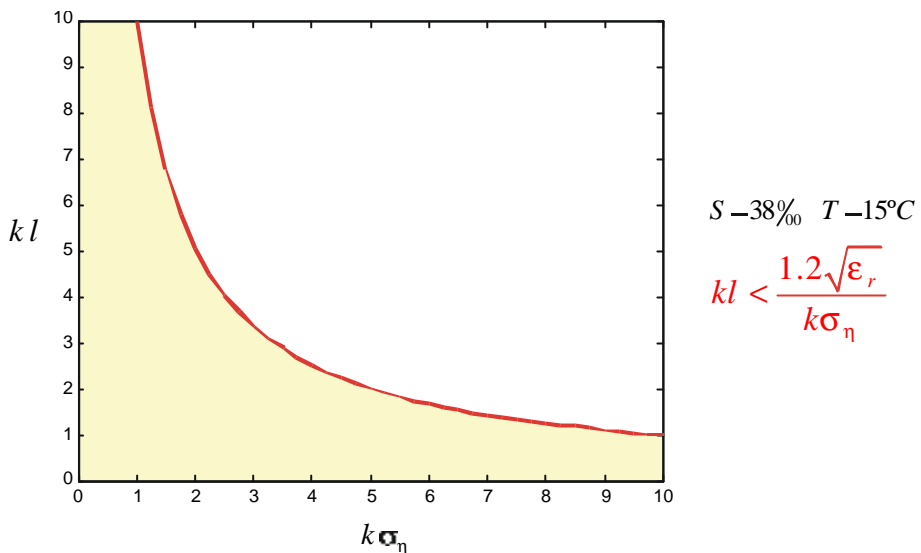


**Figure 5.12.** The yellow zone establishes the validity range of the IEM method for a sea surface with 38 psu of salinity at 15°C and Gaussian autocorrelation function.

When this validity range is studied respect to the height standard deviation and particularized at 1.4 GHz it is possible to obtain the validity range of the wind speed at 12.5 m from the sea surface for the low scale of roughness (Figure 5.14a). On the other hand for high scale of roughness the validity range is almost the complementary as it is demonstrated in Figure 5.13b.

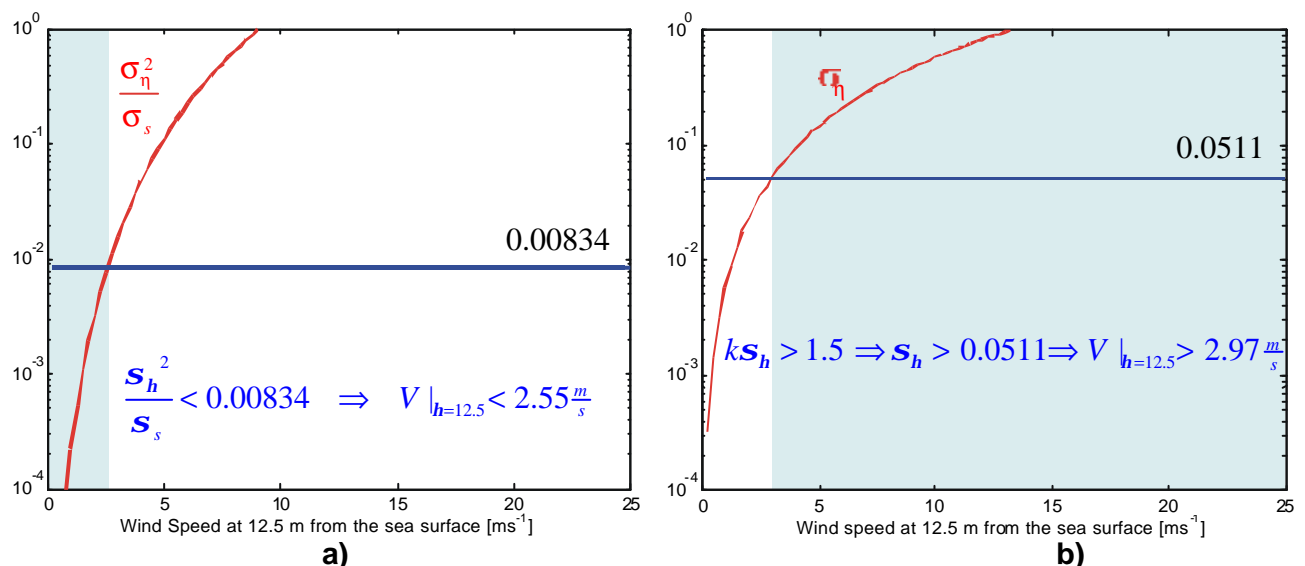


**Figure 5.13.** a) Validity range for IEM small scale. b) Validity range for IEM large scale.

However, even though the IEM appear to be an attractive method, simulation results did not compare well neither in the value of the brightness temperatures, nor in their dependences with wind speed. It appears that the rms height is dominated by the large scale component and some approximations fail. To overcome this problem, the

simulations with the two-scale model are presented below. The two-scale model consists of the SPM model for the small scale waves that satisfy the conditions of section 5.2, modulated by the local slopes of the large scale waves.

### 5.5. Yueh-LODYC two scale model

This work, not originally foreseen in the WISE contract, has been conducted in the frame of the ESA salinity study 3618, in collaboration with people involved in the present study.

We run the Yueh-LODYC 2-scale model in the in-situ conditions (incidence angle, SSS, SST, wind speed and direction) observed during radiometer measurements. Then we fit the simulated Tb as a function of the wind speed with a linear regression, in order to do the same exercise as when deriving slopes from measured Tb. This was done with 3 wave spectra: Durden and Vesecky [1985], Elfouhaily [1998] and Durden and Vesecky x 2 (Figure 5.14).

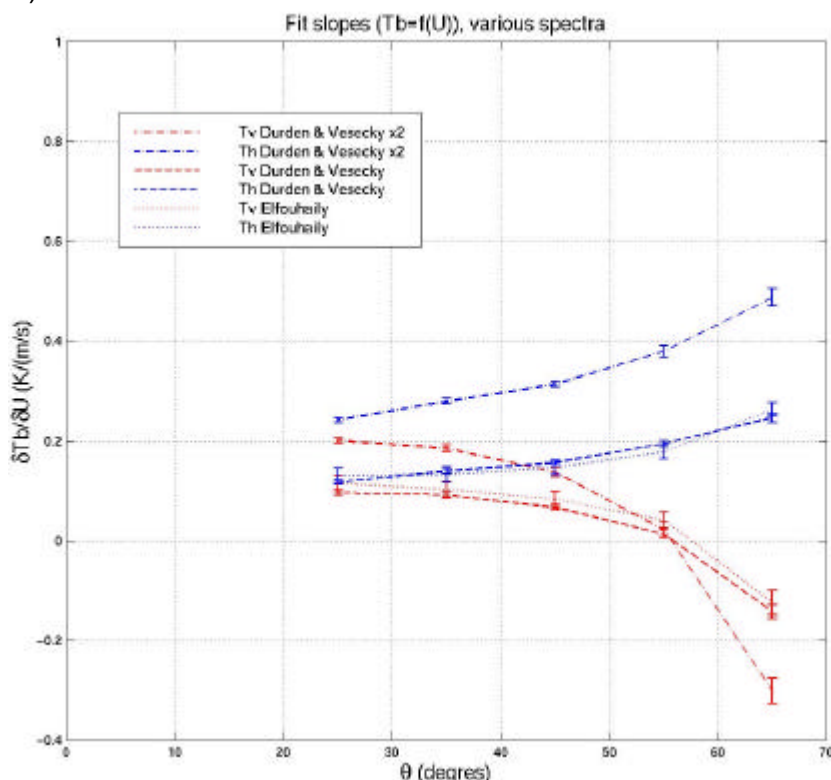


**Figure 5.14.** Slopes of Tb versus U derived from Yueh-LODYC model with 3 different spectra.

Results obtained with the Durden and Vesecky x 2 spectrum appear to be close (most of the time inside the measurements error bars) to the ones obtained from the in situ measurements. However, this comparison would need to be refined in order to take into account possible disturbances of the wind/wave field due to the platform and due to limited fetch as well as foam effects which are neglected in the present study.

## 5.6. Model results and data intercomparison

Figure 5.15 compares the WISE 2000-derived brightness temperature sensitivities to wind speed vs. incidence angle at vertical (red circles) and horizontal polarizations (blue circles) and comparison with Hollinger's measurements (diamonds) and Yueh-LODYC 2-scale model (Durden-Vesecki spectrum x 2, solid line).

As it can be appreciated WISE-2000 derived sensitivities are in agreement with Hollinger's measurements (within error bars). Even though the modelling results do not include foam, swell or other effects, the comparison with the simulation results shows that the Durden and Vesecki x 2 spectrum is closer to the ones obtained from the in situ measurements, than the results obtained with Durden and Vesecki or Elfouhaily spectra.

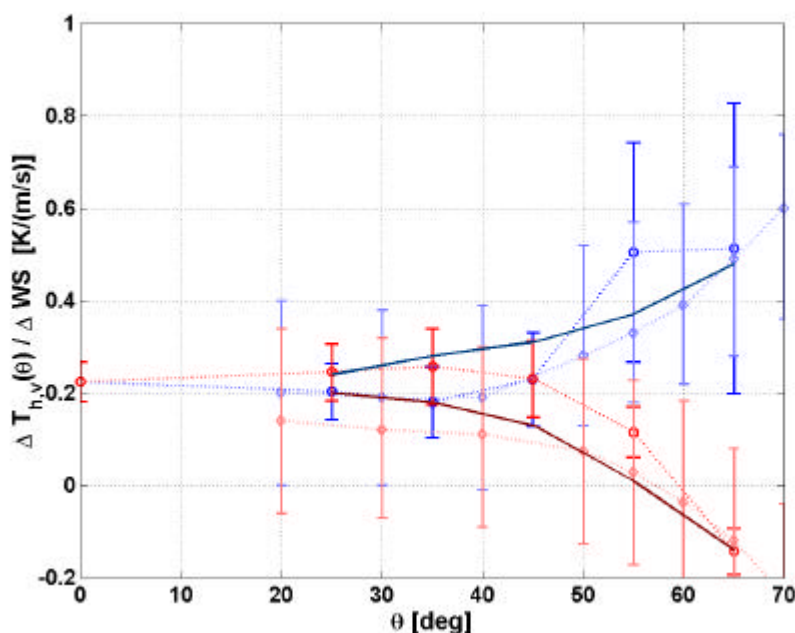


**Figure 5.15.** WISE 2000-derived brightness temperature sensitivities to wind speed vs. incidence angle at vertical (red circles) and horizontal polarizations (blue circles) and comparison with Hollinger's measurements (diamonds) and Yueh-LODYC 2-scale model (Durden-Vesecki spectrum x 2, solid line).

Foam effects can be probably negligible below wind speeds smaller than 7 m/s. However, from the data it is not easy to separate them, since most data points were acquired for wind speeds smaller than 10 m/s. If weather conditions are favorable during the second WISE campaign, a possibility may be to make a separate analysis for different ranges of wind speed.

## 5.7. Rain effects on the brightness temperature at L-band: modelling results

The effect of a rain cell within the antenna beam of a down-looking radiometer pointing to the sea surface is three-fold:

- It increases the opacity of the atmosphere and the scattering of the up-welling radiation.
- It creates a surface layer of fresh water.
- It changes the roughness of the sea surface.

The high radiometric accuracy required to determine the sea surface salinity from L-band measurements requires the identification of rainy/cloudy conditions (preferably with sensors with a spatial resolution higher than that of the radiometer antenna) and an accurate modeling of atmospheric and surface roughness effects, if rainy/cloudy pixels are going to be used in the salinity retrieval process. In this section we are going to present some preliminary results to better understand the effect of the rain induced roughness using a modified Kirchhoff model, which parameters are derived from a sea spectrum that includes wind speed and direction, and rain intensity.

### 5.7.1 Description of the model

The polarimetric bistatic scattering coefficients depend on the description of the sea surface slopes. In rain-free conditions, the sea surface slopes are described by a Gram-Charlier pdf function. In the presence of rain, the wind-induced spectrum combines with the rain-induced spectrum as described in [Craeye et al. 1997] and Craeye Ph. D. Dissertation [1998], although convergence problems have been detected in some cases. Figure 5.16 shows Elfouhaily's wind-induced spectrum for several wind speeds, together with the log-Gaussian spectrum used to describe the rain-induced ring-waves for several rain rates.

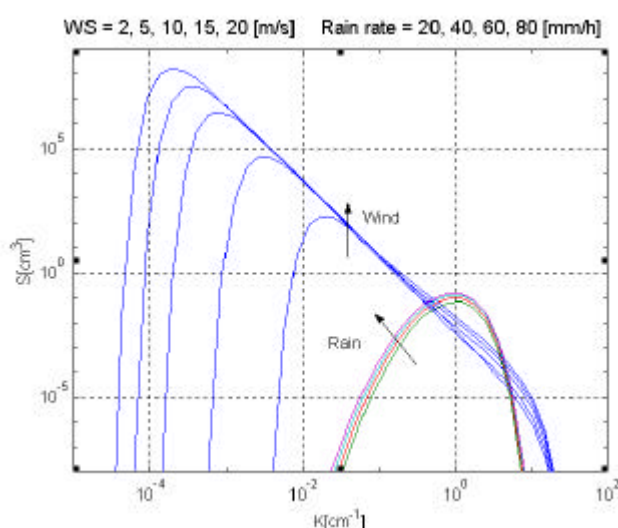


**Figure 5.16.** Wind-induced spectrum for wind speeds 2, 5, 10, 15 and 20 m/s and rain-induced spectrum for rain rates 20, 40, 60 and 80 mm/h.

The combined effect of wind and rain on the sea surface emissivity is computed using a modified Kirchhoff model with the sea surface slopes derived from the combined spectrum. Figure 5.17 shows the variance of the sea surface slopes versus wind speed computed with Cox and Munk formula, from Elfouhaily's spectrum and from the combined Elfouhaily's spectrum and rain-spectrum.

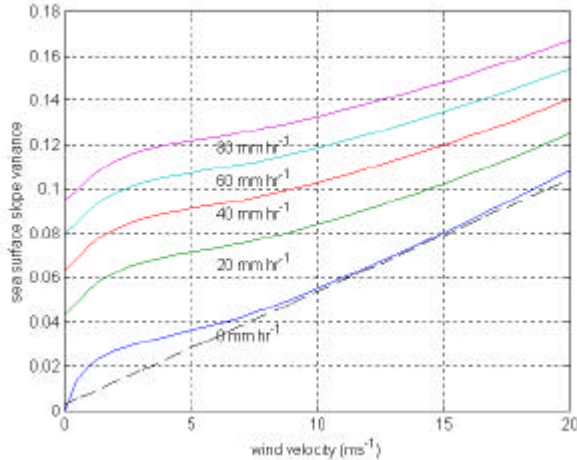


**Figure 5.17.** Sea surface slope variances versus wind speed in rain free conditions and for rain rates 20, 40, 60 and 80 mm/h.

### 5.7.2. Simulation results at L-band

Some simulations considering different rain rates and wind speeds conditions were performed. Figures 5.18 and 5.19 present the results of some of them at L-band. Plots 5.18 show the brightness temperature at horizontal polarization versus incidence angle and rain rate. Meanwhile plots 5.19 show the brightness temperature at vertical polarization also versus the incidence angle and the rain rate.

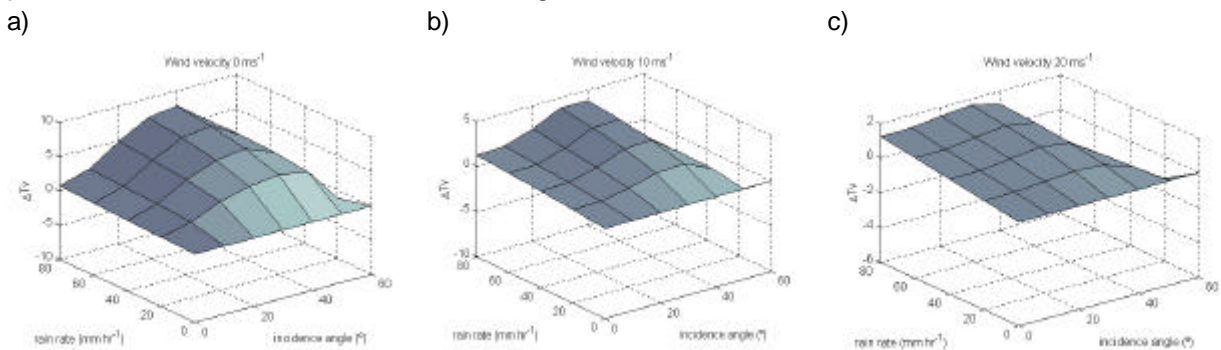


**Figure 5.18.** Vertical polarization of the brightness temperature change at 1.4 GHz due to the presence of rain:

$$\Delta T_{Bv} = T_{Bv}(\mathbf{q}, WS, rr) - T_{Bv}(\mathbf{q}, WS, 0).$$

a) Wind Speed = 0 m/s. b) Wind Speed = 10 m/s. c) Wind Speed = 20 m/s

a)

b)

c)

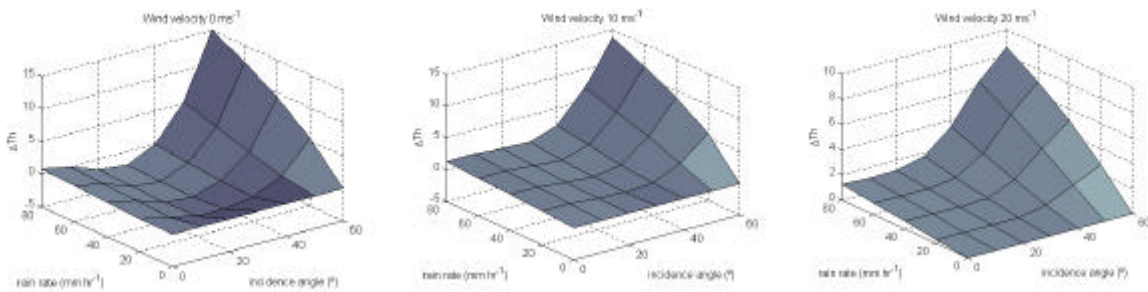


**Figure 5.19.** Horizontal polarization of the brightness temperature change at 1.4 GHz due to the presence of rain:  $\Delta T_{Bh} = T_{Bh}(\mathbf{q}, WS, rr) - T_{Bh}(\mathbf{q}, WS, 0)$ .

a) Wind Speed = 0 m/s. b) Wind Speed = 10 m/s. c) Wind Speed = 20 m/s

As it can be appreciated, rain rate always causes an increase of the brightness temperature at horizontal polarization, except at zero wind speed and medium incidence angles. The increase is almost linear with rain rate at a given incidence angle, except at higher incidence angles ( $>60^\circ$ ). At nadir, the sensitivity of the brightness temperature to rain rate is approximately 0.01 K/(mm/h), and increases up to 0.1 – 0.2 K /(mm/h) at incidence angles of  $\sim 60^\circ$  for wind speeds in the range 20 – 0 m/s.

At vertical polarization the effect of rain is completely different. At low incidence angles the brightness temperature increases moderately with increasing rain rate, reaching a maximum around  $30^\circ$ , and then decreases sharply for large incidence angles, showing negative sensitivities to rain rate  $\sim -0.1$  to  $-0.06$  K/(mm/h) for wind speed in the range 0-20 m/s.

## 6. Simulation results at L-band in WISE conditions

In order to check to what extent observed conditions and in-situ data accuracy are appropriate to validate and improve model parametrizations, we run the Yueh-LODYC two-scale emissivity model at  $30^\circ$  incidence angle without foam in the in situ conditions encountered during the campaign. This work not originally foreseen in the WISE contract, has been conducted in the frame of the ESA salinity study 3618, in collaboration with people involved in the present study.

We use measurements of SSS, SST and wind speed. Two wind data sources were tested: ICM meteorological float and platform meteorological station. During the WISE campaign, due to Ebro river discharge variations of up to 2.5 psu in SSS have been observed.

We use different parameterisations for the sea water permittivity: Klein and Swift [1977], Ellison et al. [1998] and for the sea state spectrum: (Durden & Vesecky) x 2 and Elfouhaily.

Without taking into account the wind/wave/foam effects, model of sea-water permittivity predict that these SSS and SST variations lead to variations of Tb between 0.5K and 1 K (Figure 6.1).

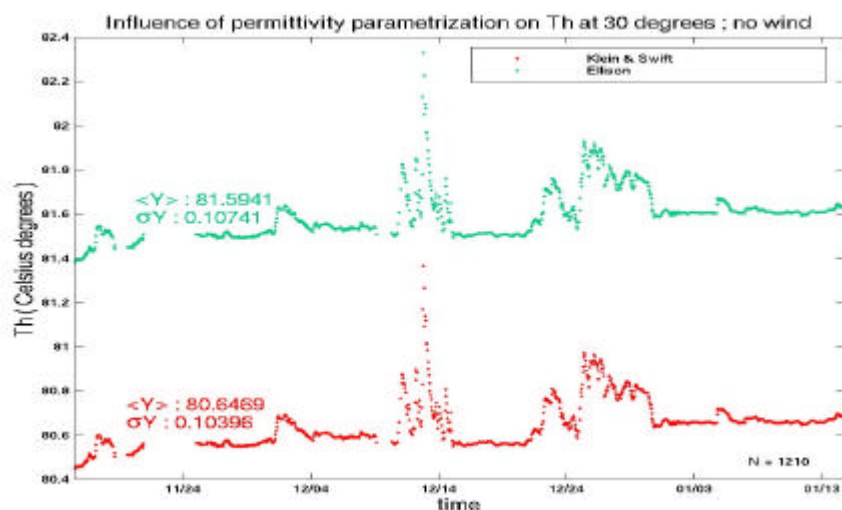


**Figure 6.1.** Tb (h-pol) variations at 30° incidence angle predicted by the Klein and Swift sea water parametrization (red) and by the Ellison parametrization (green), when only SSS and SST variations are taken into account.

Most of these variations are due to SSS variations as shown on Figure 6.2 where influences of SSS and of SST have been decoupled.

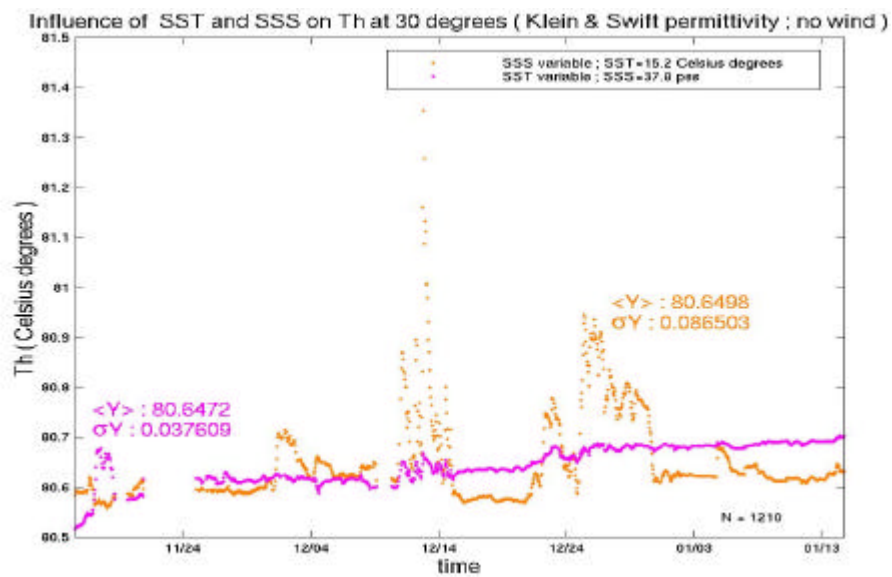


**Figure 6.2.** Tb (h-pol) variations at 30° incidence angle predicted by the Klein and Swift sea water parametrization due to SST variations at fixed SSS (37.8 psu) (purple) and due to SSS variations at fixed SST (15.2°C) (orange).

During the campaign, wind speed varies from 0 up to 25 m/s. However, wind speeds measured on the meteorological station (at 69 m height) and on the meteorological buoy (at 2.6 m height) are not in perfect agreement (rms difference of 1.8 m/s between wind speeds converted to 10 m height; meteorological station winds about 10% higher than buoy winds). In order to examine the influence of the imperfection of the wind data for model validation, we compare Tb retrieved with these two sources of wind speed and Tb retrieved with two wave spectra.

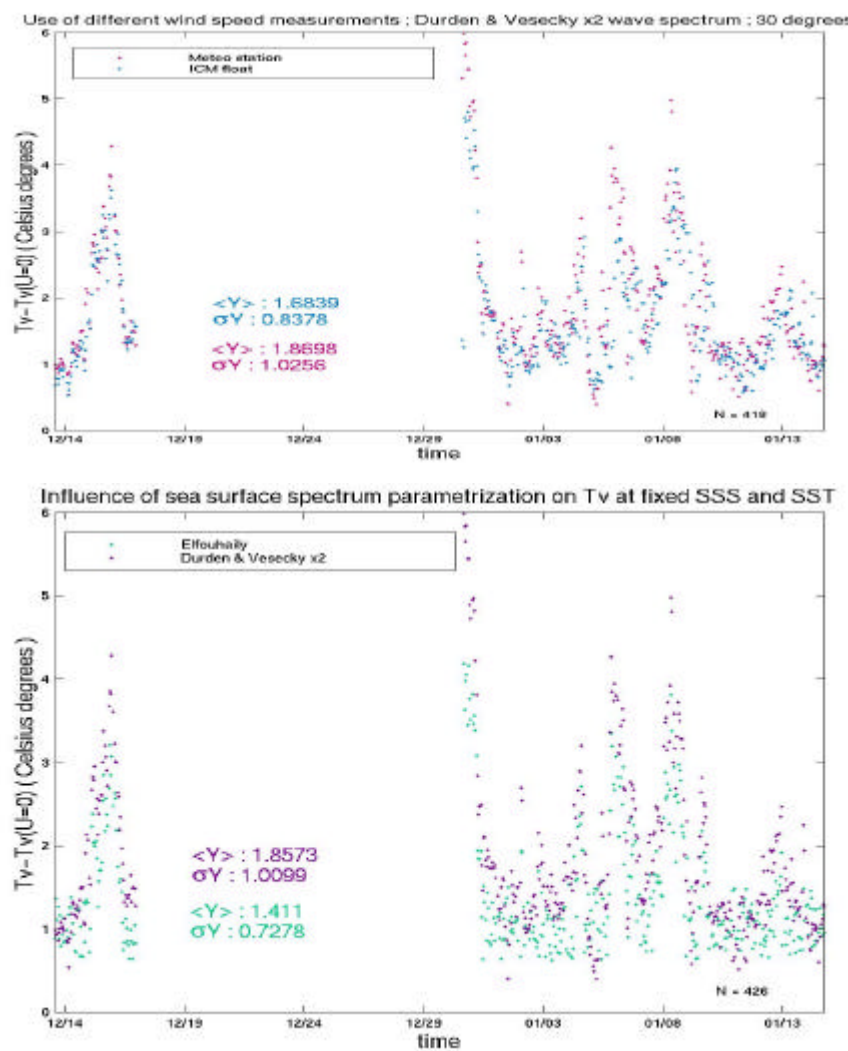


**Figure 6.3.** Influence of the wind speed on Tb at 30° incidence angle (in V-pol) when using two sources of wind speed (top) (meteorological station (purple); ICM float (blue)), and when using two wave spectra (bottom) (Elfouhaily (green); Durden and Vesely x 2 (purple)). On average, the difference coming from the different wind speed source is 0.2 K whereas the difference coming from the use of different spectra is 0.35K.

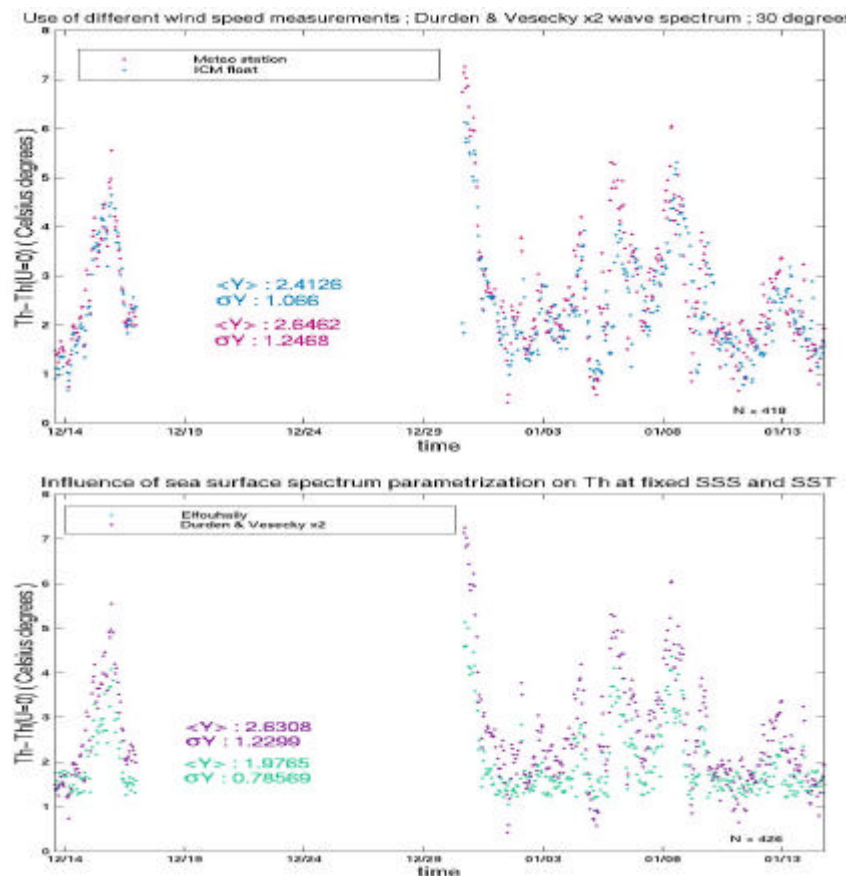


**Figure 6.4.** Influence of the wind speed on Tb at 30° incidence angle (in H-pol) when using two sources of wind speed (top) (meteorological station (purple); ICM float (blue)), and when using two wave spectra (bottom) (Elfouhaily (green); Durden and Vesecky x2 (purple)). On average, the difference coming from the different wind speed source is 0.2 K whereas the difference coming from the use of different spectra is 0.7K.

It is clear that the expected effect of wind speed is well above the effect of SSS upon Tb. In V-pol and H-pol, differences coming from imperfect in situ measurements are lower than the ones coming from different spectra parametrizations; moreover Elfouhaily spectrum lead to higher Tb at very low wind speed due to a ‘plateau’ up to 7m/s.

Despite technical difficulties the observed conditions and the in-situ data accuracy are appropriate to validate and improve model parameterisations.

## 7. The sea surface salinity retrieval problem

### 7.1. Sea Surface retrieval using WISE data (ICM)

A lot of data was acquired during the WISE campaign that least 1 month and a half. These data will be very useful for the modelers to find models that best fit the real emissivity process. But, by the other hand, these data will, also, be very beneficial to study the retrieval problem. It will allow us to test different algorithms with real data, and to study which variables are necessary (and with which accuracy) to retrieve salinity with a good exactitude.

The retrieval algorithm for SMOS is not yet defined, but to retrieve WISE data a simple least square algorithm can be used. In particular, we have used the well-known Levenberg-Marquardt algorithm (IDL toolbox).

This algorithm is a recursive system and consist of the following: the inputs are SST (from buoy 1 measured at -20cm), wind speed (measured from the meteorological station), the incidence angle, and a first guess value for salinity. These data are input in an emissivity model, and brightness temperature ( $Tb'$ ) is obtained. This  $Tb'$  is compared to the  $Tb$  measured by the L-band radiometer (see Figure 7.1). If the difference between both is larger than a threshold, a  $\Delta SSS$  is added to the first guess salinity. This process is repeated until the difference is smaller than the threshold.

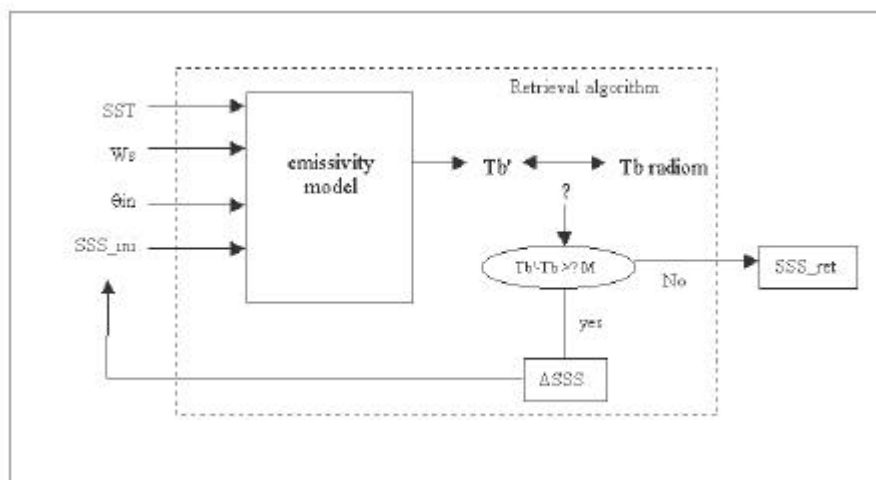


**Figure 7.1.** Block diagram of the salinity retrieval algorithm

The retrieved salinity is directly dependent on the emissivity model, so a good model is necessary to have good retrieved salinities from brightness temperature.

Only brightness temperature files acquired on January 2001 have been used for the inversion since they are less noisier than the rest of the WISE data set.

During the whole campaign the L-band radiometer was acquiring data at 5 incidence angles, except one case when data were acquired at 9 incidence angles (14-1-2001).

To reduce random noise of the measurement, two procedures have been applied to the data files. In the first one, files with very close salinity and wind conditions have been analysed as a single measurement by averaging the values for every incidence angle. In the second one, files with, also, very close salinity and wind conditions, have been put together in the same file and this one has been used to retrieve salinity. Here it follows an example:

- File from 14-1-2001 with 4 incidence angles and 4 measurements (no extra processing). The error on the retrieved SSS is 0.98 psu.
- Averaging 5 different files (9 measurements in total) from 14-1-2001. The error on the retrieved SSS is 0.35 psu.
- Putting all the measurements (9 meas.) of 5 files (14-1-2001) together. The error on the retrieved SSS is 0.39 psu.

So with this extra-processing the retrieval results improved significantly, but it is not evident which of the two procedures is better.

It has been observed that the retrieval is better in the case of 9 incidence angles than with files with only 5 incidence angles.

### **7.1.1. Emissivity Models**

Four different models have been used in the calculations:

1. NOAA model: This is an empirical model presented by NOAA (1) after the SLFMR experiment. This model follows the equation:

$$T_b = T_{\text{surf}} + T_{\text{wsp}} + T_{\text{DWR}} + T_{\text{up}} + T_{\text{EBT}} \quad (7.1)$$

Where  $T_{\text{surf}}$  is the brightness temperature produced by the sea surface,  $T_{\text{wsp}}$  is the  $T_b$  caused by wind speed,  $T_{\text{DWR}}$  is the temperature produced by the downwelling and  $T_{\text{up}}$  is produced by the upwelling. Finally  $T_{\text{EBT}}$  is due to extraterrestrial bodies.

Adapting this equation to our conditions (just 32 m above sea level), the effects of upwelling brightness temperature can be neglected. The terms  $T_{\text{DWR}}$  and  $T_{\text{EBT}}$  were already compensated for during the calibration of the radiometric data.

So ,

$$Tb = e(SSS, Ts, \mathbf{q}) \cdot Ts + 0.2 \cdot Ws \cdot \left( 1 \pm \frac{\mathbf{q}}{55} \right) \quad \left\{ \begin{array}{l} + \quad Hpol \\ - \quad Vpol \end{array} \right. \quad (7.2)$$

where  $\theta$  is the incidence angle (for  $\theta < 55^\circ$ ), and  $e$  is the emissivity computed as

$$e_H = 1 - \frac{\left| \cos(\mathbf{q}_i) - \sqrt{e - \sin^2(\mathbf{q}_i)} \right|^2}{\left| \cos(\mathbf{q}_i) + \sqrt{e - \sin^2(\mathbf{q}_i)} \right|^2} \quad (7.3)$$

$$e_V = 1 - \frac{\left| e \cdot \cos(\mathbf{q}_i) - \sqrt{e - \sin^2(\mathbf{q}_i)} \right|^2}{\left| e \cdot \cos(\mathbf{q}_i) + \sqrt{e - \sin^2(\mathbf{q}_i)} \right|^2} \quad (7.4)$$

where  $\epsilon$  is the dielectric constant obtained by Klein & Swift [1977] and is function of surface temperature and salinity.

2. NOAA model with a new wind dependence derived by UPC from the WISE data (Figure 4.6). The equation is as follows

$$Tb = e(SSS, Ts, \mathbf{q}) \cdot Ts + B(\mathbf{q}) \cdot Ws \quad (7.5)$$

Where the wind dependence is different for each angle and has been obtained by adjusting the in-situ measurements (see section 4.1).

3. Yueh's model. This is a two scale model that uses the spectrum of Durden & Vesecski .
2. This model is available not in an analytical equation, but in a table with tabulated values. The input values are: SSS, SST, WS, azimuth angle, and elevation angle.
4. The last model is the same as in case 2, but with a small bias correction to WS, that has shown to improve the results,

$$Tb = e \cdot Ts + B(\mathbf{q}) \cdot (Ws - 0.7) \quad (7.6)$$

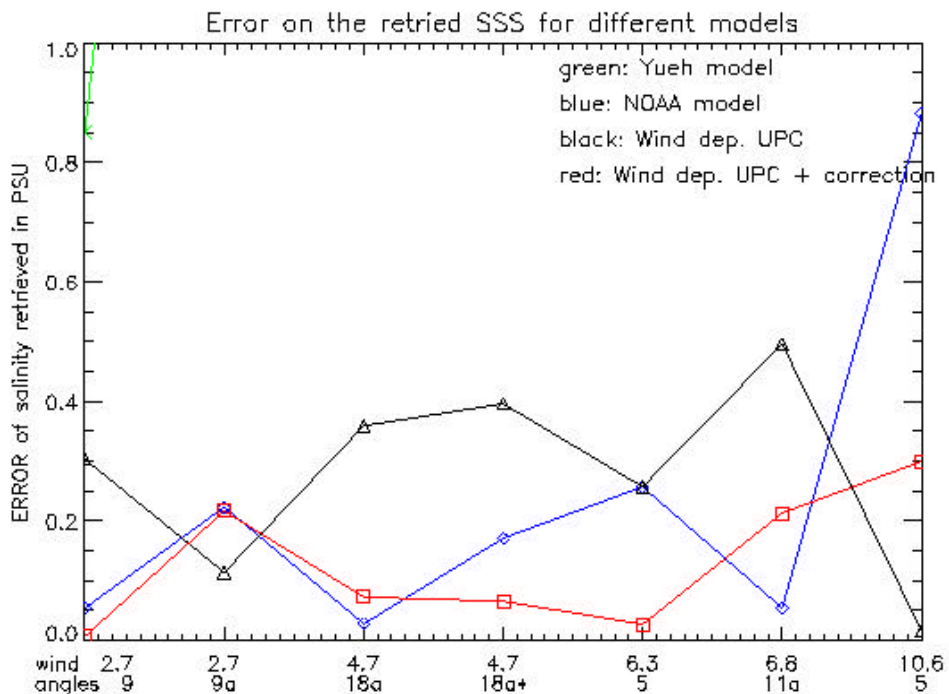


**Figure 7.2:** Comparison of retrievals using different models.

Figure 7.2. shows the comparison between the 4 models for 7 cases. The Y axis represents the error on the retrieved SSS vs. in situ data. The X axis, indicates the 7 studied cases, with the corresponding wind speed measured by the meteorological station and the number of different incidence angles (or measurements) included in the retrieval.

The sign 'a' marks the cases when measurements made on different moments have been averaged for the 5 incidence angles. The case 18a\* is the same as 18a, but all the measured Tb data have been included in the computation without previous averaging for each incidence angle.

From the Figure 7.2 it can be concluded that the case of the wind dependence derived from WISE with the correction on wind (model 4) gives the best results.

It is also clear that the retrieval using Yueh's model gives retrieved salinities far from reality (errors larger than 0.85 psu) with always an underestimation of the retrieved salinity. This underestimation can be explained by a low wind dependence in Yueh's model, that could be due to an error on the software that reads the tables (advertised by J. Boutin). This problem has not been possible to fix by the moment of writing this report.

All the above retrievals have been calculated using the dielectric constant modelled by Klein & Swift. A comparison of this model with the Ellison [1996] model has been

performed. Using the Klein & Swift model the SSS retrieved is much better (difference of  $\leq 1.5$  psu) than using Ellison.

### 7.1.2 Error on in-situ measurements

An important issue that has been studied is the effect on the retrieval of having some error on the wind and SST measurements.

The consequence of adding some error on the wind measurement has been calculated. For example, for a bias of 1 m/s on the wind speed, the error on the salinity retrieved increases by 0.35 psu as average.

The SSS retrieval has also been computed, using the wind speed measured by the QuickSCAT satellite (space resolution = 25 Km, accuracy = 2 m/s). Figure 7.2. shows the difference between using the in-situ and the satellite wind measurement using model 4.

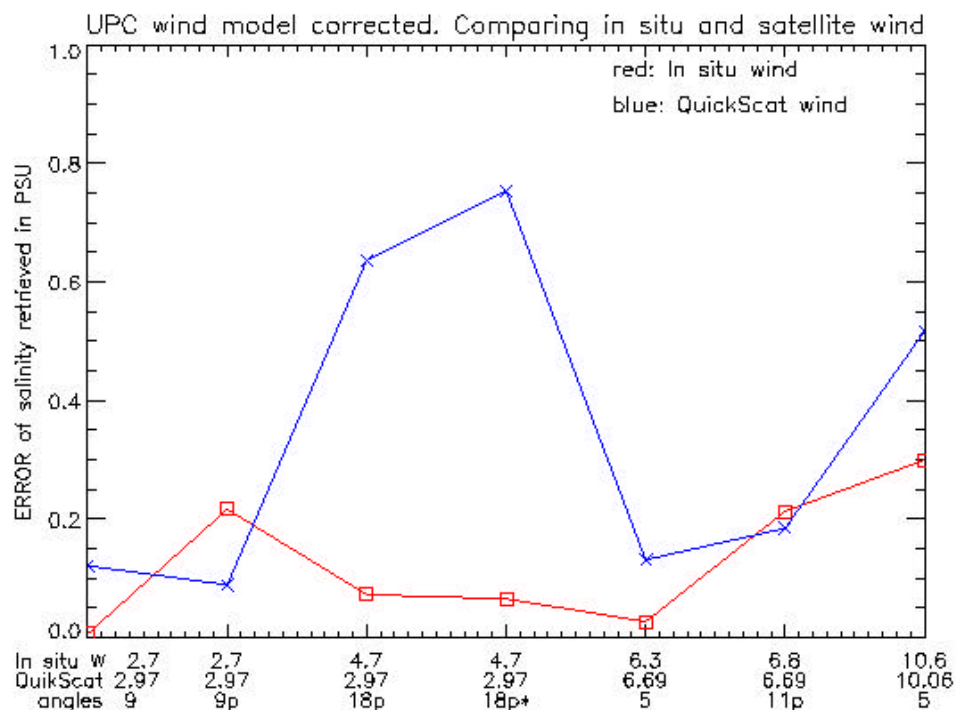


**Figure 7.3.** Comparison of retrieved SSS using in-situ and satellite wind data.  
Wind data bias corrected

The values of the wind for the in-situ and QuickSCAT are written on the X axis of Figure 7.3. It can be observed that large differences on wind produce large errors on the retrieved SSS.

As the retrieved SSS is so sensitive to noise or bias on the wind, the possibility to obtain the wind directly from the L-band radiometer measurements (as the salinity) should be considered. The inversion with the wind as a free parameter (but putting an initial value) has been performed. An example is the following (case where 9 incidence angles were acquired):

- When considering no error on the wind, the retrieved SSS has an error respect the in-situ measurement of  $\Delta SSS=0.01$  psu
- Considering an error on the wind of 2 m/s (Accuracy of QuickSCAT), the retrieved SSS has an error of  $\Delta SSS=0.85$  psu
- Leaving the wind as an unknown variable, the retrieved variables have an error of  $\Delta SSS= 0.54$  psu and  $\Delta W = 0.55$  m/s

So when the error on the measurement of the wind is large, it is better to leave this parameter as an unknown variable, but only for the cases where the noise on the brightness temperature is low, and where more than 5 incidence angles have been acquired.

The dependence of the retrieved salinity to errors on the measurement of sea surface temperature have also been studied.

During the days with less noisy data (January 2001) the infra-red radiometer was not operating, so the retrieval of SSS using the SST from the radiometer was not possible.

A possible calibration of SMOS will be done by using the Argo profiler system that will measure sea temperature at 5 m below sea level. As during WISE there was a second Microcat measuring temperature at this depth, the error due to have temperature at this depth and not surface has been computed. The maximum temperature difference observed between -5m and -20cm is 1° C, and this introduces an error increment on the retrieved SSS respect to SST of  $\approx 0.02$  psu.

So it shows that errors on the measurement of wind speed have a big impact on the retrieved SSS, while errors on the measured SST have low influence on the retrieval.

### **7.1.3. Conclusions**

This work demonstrates that the retrieval of salinity from WISE data is feasible. The results are better with higher number of incidence angles, and when joining or averaging different files with very similar wind and salinity conditions (reducing the noise).

It can also be concluded, that the emissivity models and the dielectric models have a big impact on the quality of the retrieved salinity (as expected) and that efforts should be

put on trying to find the best models. It has also been shown that the retrieval is very sensitive to wind errors, but not to SST bias.

## 7.2. Sea surface retrieval using WISE fits in the SMOS configuration<sup>2</sup> (UPC)

### 7.2.1. Introduction

Sea Surface Salinity (SSS) has already been retrieved from L-band radiometric measurements at constant incidence angles (e.g. SLFMR). The SMOS configuration, however, presents a very particular property that can be exploited: the same pixel is observed under different views at different incidence angles, with varying spatial resolution, radiometric accuracy and sensitivities, depending on the position of each pixel with respect to the cross-track. Figure 7.4 represents this particular imaging characteristics for the final SMOS configuration. The arrows indicate the tracks followed by a pixel since it enters in the field of view (top), until it leaves it (bottom). Depending on the distance with respect to the satellite ground-track, the number of snap-shots in which the pixel will be imaged will vary. As it goes far away from the ground-track, not only it is imaged less and less times, but also the angular variation reduces and measurements become noisier, which will translate in a performance degradation in terms of the retrieved parameters.

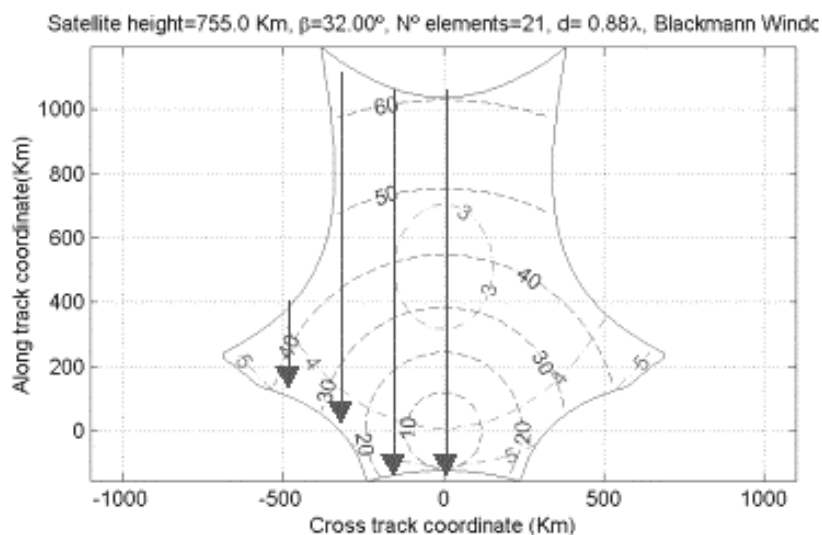


**Figure 7.4.** The SMOS imaging characteristics: a pixel is imaged many times under different incidence angles, with different spatial resolutions and radiometric sensitivities. Parameters: NEL=21 antennas per arm,  $d=0.875$  wavelength antenna spacing,  $\beta=32^\circ$  tilt angle,  $h = 755$  km platform height.

The SSS retrieval problem presents some difficulties that are listed below:

---

<sup>2</sup> This work has been performed in the frame of the project CICYT "Técnicas de teledetección con énfasis en polarimetría e interferometría", CICYT TIC99-1050-C03-01

1. Sensitivity of the brightness temperatures to SSS is about 0.5 K/psu, and that to WS is about 0.2 K/(m/s). Taking into account the range of variability of the SSS (30-38 psu) and the WS (0-~25 m/s), the **WS can mask the SSS signature**, unless it is properly corrected.

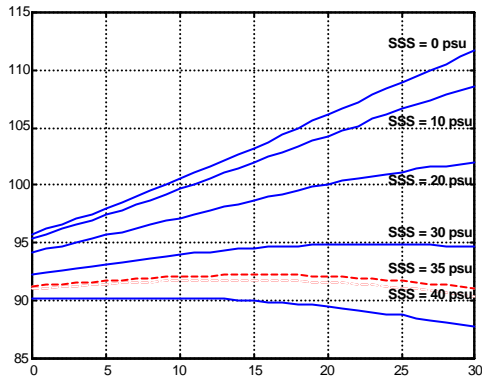


**Figure 7.5.** Brightness temperature at nadir dependence with SSS and SST:

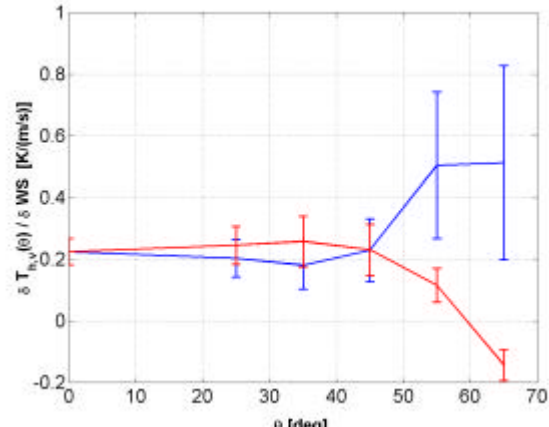


**Figure 7.6.** Sensitivity of brightness temperature to WS vs. incidence angle.

Figure 7.5 shows the dependence of the brightness temperature at nadir vs sea surface temperature (SST) and SSS. Figure 7.6 shows the dependence with WS derived in section 4.2.1. Since it is very small, a first order approximation has been adopted:

$$T_{v,h}(\mathbf{q}, \text{SST}, \text{SSS}) \approx (1 - \Gamma_{v,h}(\mathbf{q}, \text{SST}, \text{SSS})) \cdot \text{SST} + \Delta T_{v,h}(\mathbf{q}, \text{WS}) \quad (7.7)$$

2. **Polarization mixing** problems. The SMOS imaging characteristics, with a very wide field of view suitable for Earth observation creates a polarization mixing. That is, the **brightness temperatures in the antenna reference frame** are **related** to the **brightness temperatures** in the **local reference frame** over the Earth by

$$\begin{bmatrix} T_V \\ T_H \end{bmatrix}^{(ant)} = \begin{bmatrix} \cos^2 y & \sin^2 y \\ \sin^2 y & \cos^2 y \end{bmatrix} \begin{bmatrix} T_V \\ T_H \end{bmatrix}^{(pixel)}, \quad (7.8)$$

where the angle **y** depends on the observation geometry, but also on the Faraday rotation, that cannot be neither neglected at L-band<sup>3</sup>. The **polarization mixing problems** (geometry + Faraday rotation) can be **avoided** if the **retrieval problem** is **formulated** in terms of the first Stokes parameter **I** defined as:

$$I = T_V^{ant} + T_H^{ant} = T_V^{pixel} + T_H^{pixel}, \quad (7.9)$$

<sup>3</sup> It can be estimated for correction in (7.8), but the accuracy is not always enough, and additionally local inhomogeneities in the ionosphere may create different Faraday rotations within a pixel.

which is **invariant to rotations**, as it can be readily deduced from equation 7.8.

As a collateral gain, this approach minimizes the effect of the uncertainty in the dielectric permittivity (Klein and Swift or Ellison). Since the sum of the two plots in Figure 5.1 is approximately constant, this uncertainty will appear as an offset.

### **7.2.2. SSS retrieval algorithm**

The SSS retrieval algorithm will minimize the error defined as

$$e = \left( \left\| I^{model} \right\|_{(1)} - \left\| I^{data} \right\|_{(1)} \right)^2 / N_{observations}, \quad (7.10)$$

where  $I^{model}$  is the first Stokes parameter ( $T_h + T_v$ ) computed from the estimated SSS, SST and WS, and  $I^{data}$  corresponds to the measured first Stokes parameter computed from the sum of consecutive  $T_h$  and  $T_v$  in a pixel by pixel basis.

As a starting point, it has been assumed that  $I^{data}$  contains only a pixel-dependent random noise error. All pixels in alias-free FOV included, regardless of the noise level and incidence angle. The minimization method used is the Levenberg-Marquardt method of the Matlab © Optimization Toolbox, with restrictions for SSS (30-40 psu), SST (0-40°C), WS (0-30 m/s). However, the speed and accuracy of the retrieval is improved by reducing the search limits to an interval within the error bounds given by the starting point provided by other sensors, for example: SST = nominal SST  $\pm 1^\circ C$ , WS = nominal WS  $\pm 2.5$  m/s. It is found that this approach produces better results than forcing the nominal SST and WS, which may not be exact.

Figures 7.7, 7.8. and 7.9. show the standard deviation of the retrieved SSS, SST and WS for different wind speed 0 m/s (left) and 10 m/s (right), different SSS (a-b) 30 psu, (c-d) 35 psu and (e-f) 40 psu, and different SST: 5°C, 15°C and 25°C.

### **7.2.3. Conclusions**

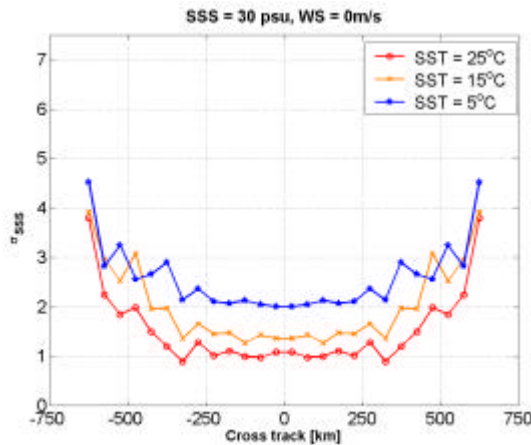
- In general SSS retrieval improves with increasing SST, except for high SSS and WS.
- As expected, because of the lower number of samples and the higher noise, SSS estimates worsen at swath edges because of higher noise level.
- The estimated values of SST and WS have the same standard deviation as the ones provided by other sensors.
- Forcing SST and WS (within measurement errors  $\pm 1^\circ C$ ,  $\pm 2$  m/s) induces a larger error in the SSS estimate than leaving them as free parameters.
- Most SSS error is a bias (positive or negative), not a random error, as shown in Figures 7.10 and 7.11. At low WS, the estimated WS tends to be higher (positive bias), which the algorithm compensates increasing the estimated SSS (positive bias, Figure

7.10). At higher WS, the situation is reversed (Figure 7.11). In all cases, SST estimates have a very small bias, and most of the error is random.

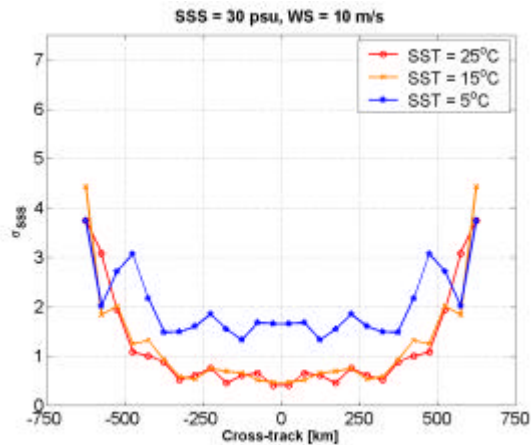
- Systematic errors need to be modeled and simulated. It is not known yet how much the SSS accuracy will be degraded for:
  - a 1.5 K accuracy error (rms value for pixels in the FOV)
  - a bias in the whole FOV due to a different average value of the brightness temperature in the alias-free FOV, and that measured by the Noise Injection Radiometer (zero-baseline:  $V_{h,v}(0,0)$ ).

**Retrieved SSS (std dev): steering = 0°, SST = 5°C, 15°C, 25°C**

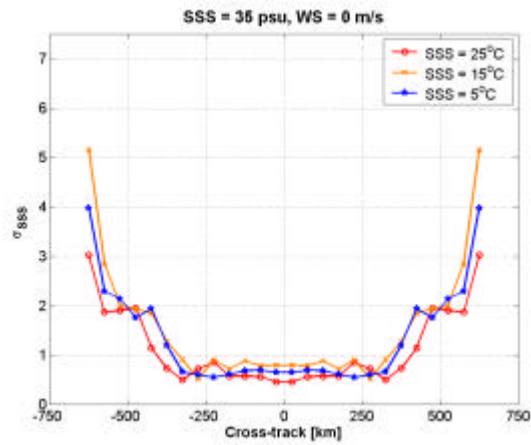
WS = 0 m/s



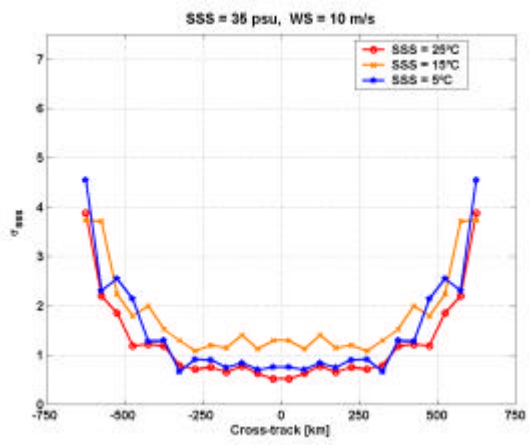
a)



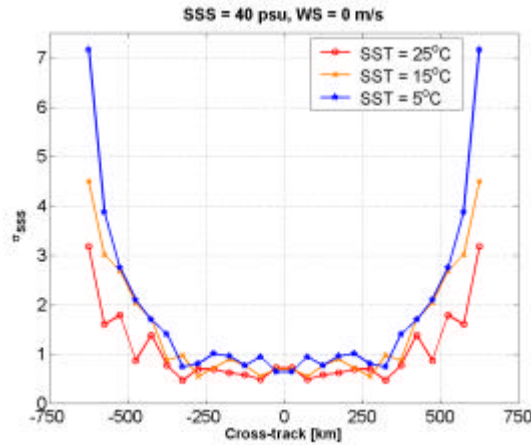
b)



c)



d)



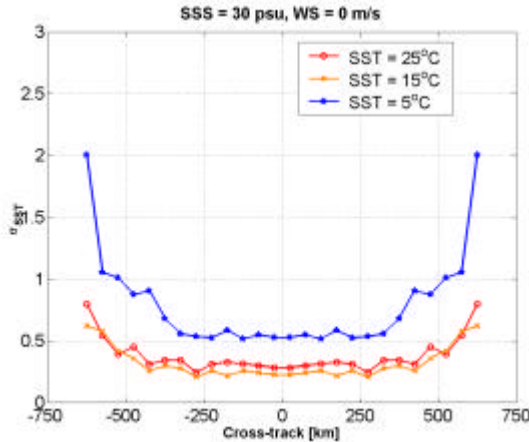
e)

f)

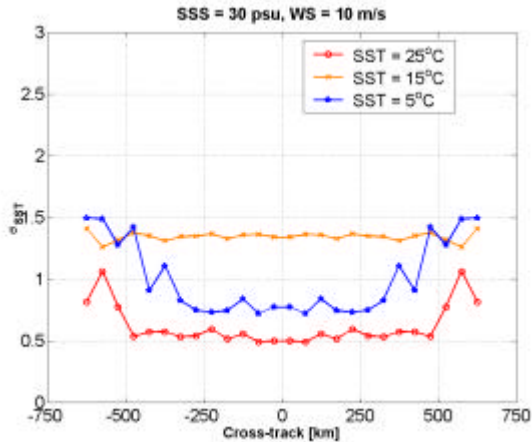
**Figure 7.7.** Standard deviation of the retrieved SSS for different wind speed 0 m/s (left) and 10 m/s (right), different SSS (a-b) 30 psu, (c-d) 35 psu and (e-f) 40 psu, and different SST: 5°C, 15°C and 25°C.

**Retrieved SST (std dev): steering = 0°, SST = 5°C, 15°C, 25°C**

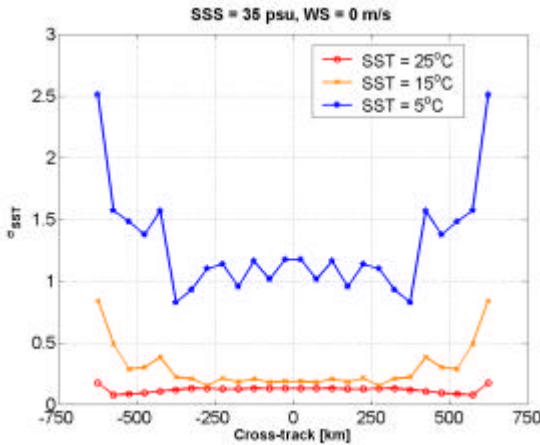
WS = 0 m/s



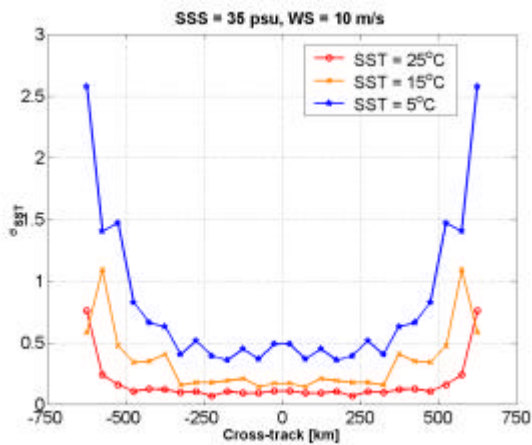
a)



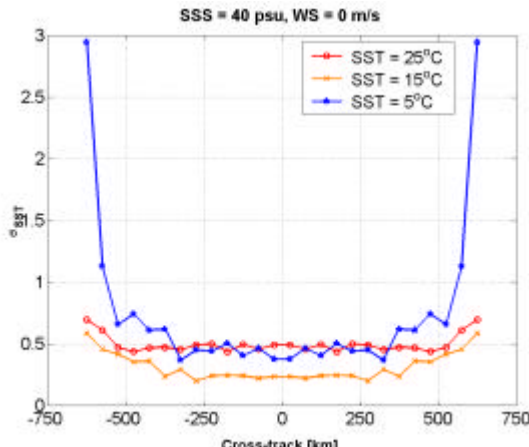
b)



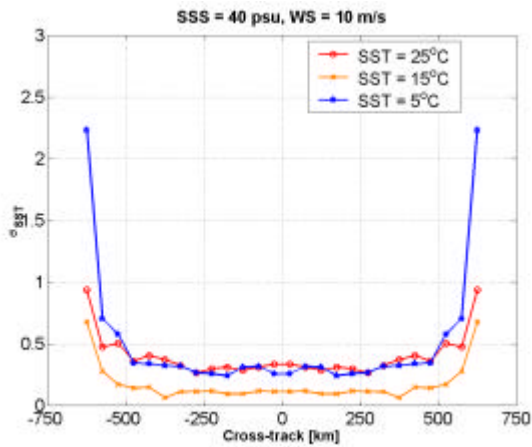
c)



d)



e)

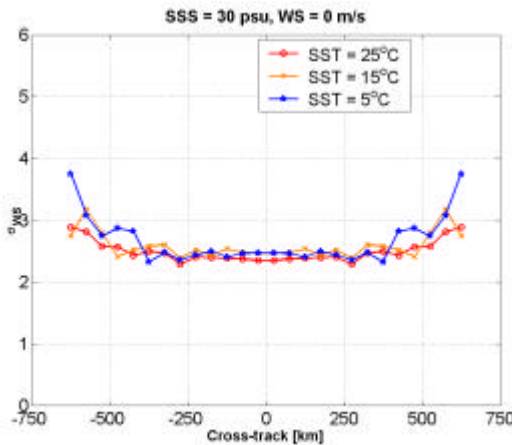


f)

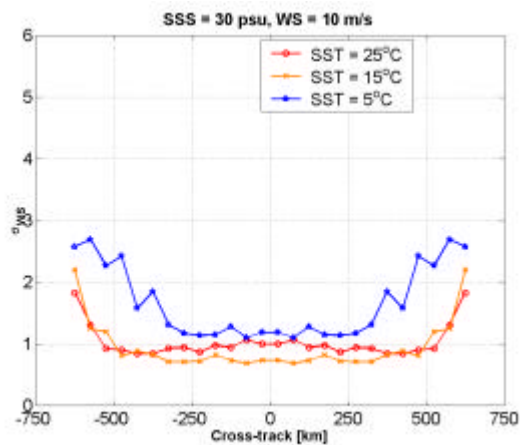
**Figure 7.8.** Standard deviation of the retrieved SST for different wind speed 0 m/s (left) and 10 m/s (right), different SSS (a-b) 30 psu, (c-d) 35 psu and (e-f) 40 psu, and different SST: 5°C, 15°C and 25°C.

**Retrieved WS (std dev): steering = 0°, SST = 5°C, 15°C, 25°C**

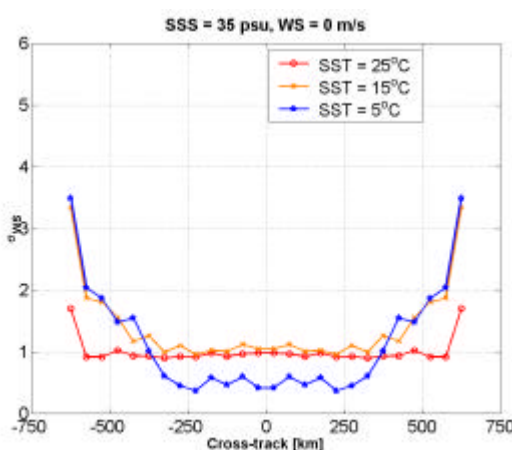
WS=0 m/s



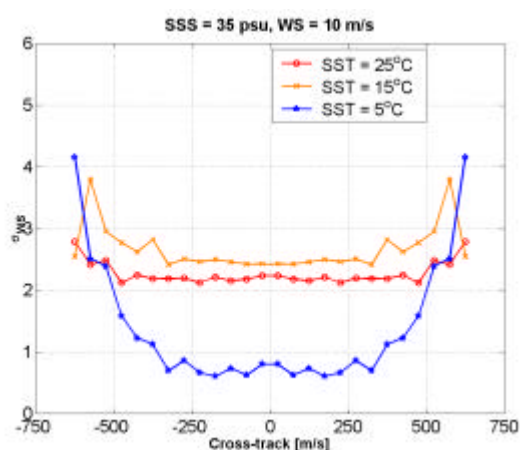
a)



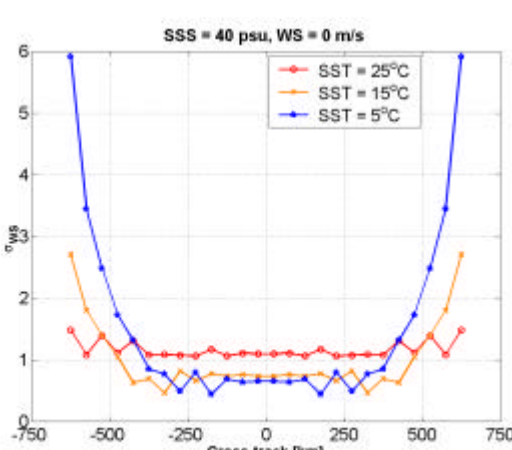
b) WS = 10 m/s



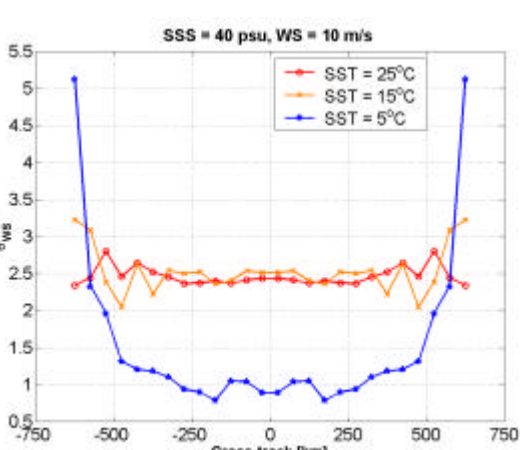
c)



d)



e)



f)

**Figure 7.9.** Standard deviation of the retrieved WS for different wind speed 0 m/s (left) and 10 m/s (right), different SSS (a-b) 30 psu, (c-d) 35 psu and (e-f) 40 psu, and different SST: 5°C, 15°C and 25°C.

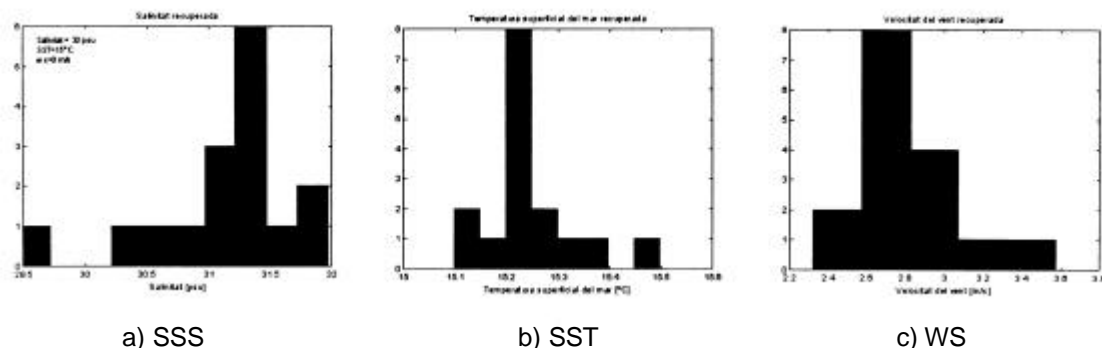


**Figure 7.10.** Typical histograms of retrieved SSS, SST and WS for SSS = 30 psu, SST = 15°C and WS = 0 m/s. Positive bias in SSS and WS.

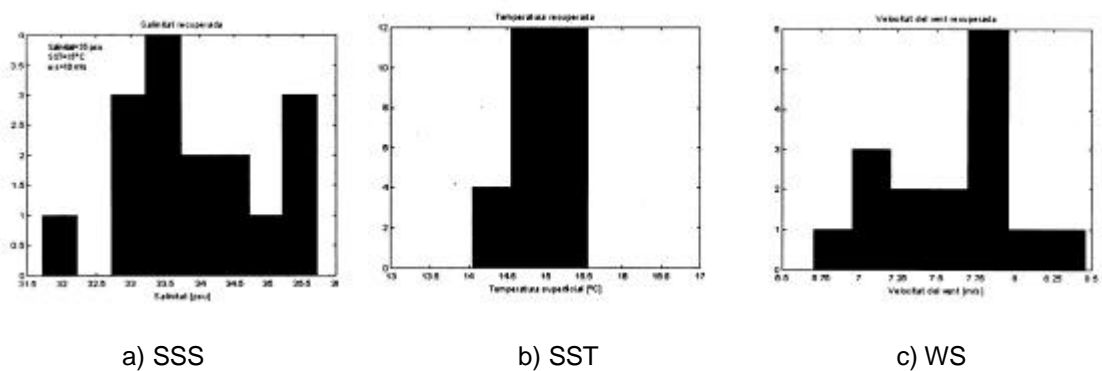


**Figure 7.11.** Typical histograms of retrieved SSS, SST and WS for SSS = 35 psu, SST = 15°C and WS = 10 m/s. Negative bias in SSS and WS.

## 8. General conclusions of WISE 2000

Despite a number of technological, logistic, and RFI problems, the WIND AND SALINITY EXPERIMENT 2000 has provided for the first time in the last 30 years, new data to better understand the effects of the wind in the emissivity of the sea at L-band. The experimental results confirm the existing experimental data [Hollinger, 1971] and have reduced their associated error bars. The experimental results show a nadir sensitivity of 0.22 K/(m/s) and seem to indicate that the Durden and Vesecki spectrum multiplied by two, can be an appropriate description for the sea state. The magnitude of the azimuthal variation of the first two Stokes parameters is 0.1 – 0.2 K approximately, but these results have to be confirmed by the results of the LOSAC campaign. The analysis of the sea state reveals that often the wind stress and the sea state are correlated, and the wind intensity and direction can be used to describe its state. However, in some situations the correlation is quite low, meaning that the wave field was originated somewhere else. In this case a characterization and modelling of the swell would be required.

It has also been demonstrated that SSS can be retrieved with enough accuracy from multi-angular measurements. Even though the WS measurements from the buoy anemometer, the meteo station and QUICKSCAT are in agreement ( $\sigma_{\text{buoy-met st}} = 1.8 \text{ m/s}$ ,  $\langle WS_{\text{buoy-met st}} \rangle = -0.9 \text{ m/s}$ ,  $\sigma_{\text{met-Quick}} = 2.8 \text{ m/s}$ ,  $\langle WS_{\text{met st-Quick}} \rangle = 0.4 \text{ m/s}$ ), it is found that if the WS measurement have a large error, the SSS retrieved performs better leaving the WS as a variable rather than a fixed parameter.

Even though the WS measurements from the buoy, the meteo station and the QuickSCAT are in agreement, the quality of it improves with the number of incidence angles. The IR SST estimates have proven to be accurate enough for the SSS retrieval process, exhibiting a small bias (~ -0.2 K) that increases at high incidence wind speeds, probably because of a lack of accurate modelling of the sea foam emissivity at the IR.

The stereo-camera and video imagery results have corroborated the sea foam coverage dependence with wind speed, although a large variability exists for the same wind conditions. An interesting point found was the lower foam coverage in the North side of the platform because of the stabilization of the incoming waves interfering with the reflected ones. This may be the reason for the discrepancy between the measured Ka-band horizontal brightness temperature and the predicted one [Camps and Reising, 2001]. The RFI coming from the Tarragona shore has not allowed us to compare the evolution of the sea state and the brightness temperatures. This problem will be solved in WISE-2001 by orienting the stereo-cameras to the West side.

- Two fundamental points to be addressed in a near future are:
- to get more data points and better WS measurements so as to reduce the sensitivity to WS uncertainty,
  - to study the sea state stability by looking to series of brightness temperatures, and
  - to determine the emissivity of sea foam at L-band and different incidence angles.

The first two will be addressed during the second WISE campaign during the 2001 autumn, while the third one would require a specialized field experiment.

## Bibliography

- Camps, A., and S.C. Reising, "A Model for Wind Direction Signature in the Stokes Emission Vector of the Ocean Surface at Microwave Frequencies", *Microwave and Optic Technology Letters* Vol 29, No 6, pp 426-432, 20 Juny 2001.
- Cox, C., and Munk, W., 1954, Measurements of the roughness of the sea surface from photographs of the sun's glitter, *J. Opt. Soc. Amer.*, 44, 838-850.
- Craeye, C., "Radar Signature of the sea Surface Perturbed by Rain", Ph. D. Dissertation, Université Catolique de Louvain, December 1998.
- Craeye,C., Sobieski,P.W., and Bliven, L.F., "Scattering by artificial wind and rain roughned water surfaces at oblique incidences", *Int. J. Remote Sensing*, Vol 18, No 10, pp 2241-2246, 1997
- Donlon, C.J., Keogh, S.J., Baldwin, D.J., Robinson, I.S., Ridley, I., Sheasby, T., Barton, I.J., Bradley, E.F., Nightingale, T.J., and Emery, W., 1998, Solid-state radiometer measurements of sea surface skin temperature, *Journal of Atmospheric and Oceanic Technology*, 15, 775-787.
- Donlon, C.J., and Nightingale, T.J., 2000, Effect of atmospheric radiance errors in radiometric sea-surface skin temperature measurements, *Applied Optics*, 39(15), 2387-2392.
- Ellison,et al. 'Study and measurement of the dielectric properties of sea water'. European Space Agency N° 11197/94/NL/CN, 1996
- Goodberlet, M. & Miller, J. 'NPOESS-SEA SURFACE SALINITY', NOAA Contract #43AANE704017, Final Report, Dec. 1997.
- Hollinger, J.P., "Pasive Micorwave Measurements of Sea Surface Roughness", *IEEE Trans. Geosci. Electronics*, GE-9, 3, 165-169, 1971.
- Klein,L.A. & Swift, C.T. 'An Improved Model for the Dielectric Constant of Sea Water at Microwave Frequencies', *IEEE J. Oceanic Engr.*, OE-2, 1, 104-111, 1977.
- Masuda, K., Takashima, T., and Takayama, Y., 1988, Emissivity of Pure and Sea Waters for the Model Sea Surface in the Infrared Window Regions, *Remote Sensing Environ.*, 48, 302-308.
- Melin F., B. Bulgarelli, N. Gobron, B. Pinty and R. Tacchi, An integral tool for SeaWiFS operational processing, Internal Report EUR 19576 EN, 2000.
- Monahan, E.C., and M.Lu, Acoustically relevant bubble assemblages and their dependence on metereological parameters, *IEEE.J Oceanic Eng* 15, p 340, 1990
- Monahan, E.C., and I.G.O 'Muircheartaigh, Whitecaps and the passive remote sensing of the ocean surface, *Int J Remote Sensing* 7, pp 627, 1986
- Pietras, C., Abu Hassan, N. K., Haeffelin, G., Brogniez, G., Legrand, M., and Buis, J.P., 1994, Development of a high precision thermal infrared field radiometer, *Proceedings of 6<sup>th</sup> ISPRS Symposium*, Val d'Isere, France, Jan. 17-21: 809-815.
- Sicard, M., Spyak, P. R., Brogniez, G., Legrand, M., Abu Hassan, N. K., Pietras, C., and Buis, J.P., 1999, Thermal infrared field radiometer for vicarious cross-calibration: characterization and comparisons with other field instruments, *Optical Engineering*, Vol. 38(2): 345-356.

- Sidrin, M., 1981, Broadband reflectance and emissivity of specular and rough water surfaces, *Appl. Opt.*, 20, 3176-3183.
- Smith S.D., Coefficients for sea surface wind stress, heat flux, and wind profiles as a function of wind speed and temperature, *J. Geophys. Res.*, 93, 15467-15472, 1988.
- Smith, W.L., Knuteson, R.O., Revercomb, H.E., Feltz, W., Howell, H.B., Menzel, W.P., Nalli, N.R., Brown, O. Brown, J., Minnett, P., and McKeown, W., 1996, Bulletin of the American Meteorological Society, 77(1): 41-50.
- Swift, C.T., and McIntosh, R.E., 1983, Considerations for microwave remote sensing of ocean surface salinity, *IEEE Trans. Geosci. Remote Sensing*, 21, 480-491.
- Watts, P.D., Allen, M.R., and Nightingale, T. J., 1996, Wind speed effects on sea surface emission and reflection for the Along Track Scanning Radiometer, *Journal of Atmospheric and Oceanic Technology*, 13, 126-141.



## WISE Scientific Analysis Report